Title

Fool's Gold, Density Functional Theory, and the Future of Photovoltaics: Experimental and Computational Approaches to Reducing the Price of Solar

Author

Lucas, James Matthew

Publication Date

2014

Peer reviewed|Thesis/dissertation

Fool's Gold, Density Functional Theory, and the Future of Photovoltaics: Experimental and Computational Approaches to Reducing the Price of Solar

by

James Matthew Lucas

A dissertation submitted in partial satisfaction of the

Requirements for the degree of

Doctor of Philosophy

in

Engineering – Mechanical Engineering

and the Designated Emphasis

in

Energy Science and Technology

in the

Graduate Division

of the

University of California, Berkeley

Committee in charge:

Professor A. Paul Alivisatos, Co-Chair

Professor Ralph Greif, Co-Chair

Professor Ting Xu

Professor Samuel Mao

Fall 2014

Fool's Gold, Density Functional Theory, and the Future of Photovoltaics: Experimental and Computational Approaches to Reducing the Price of Solar

By

James Matthew Lucas

Abstract

Fool's Gold, Density Functional Theory, and the Future of Photovoltaics: Experimental and Computational Approaches to Reducing the Price of Solar

By

James Matthew Lucas

Doctor of Philosophy in Mechanical Engineering

Designated Emphasis in Energy Science and Technology

University of California, Berkeley

Professor A. Paul Alivisatos, Co-chair

Professor Ralph Greif, Co-chair

At the outset of this research, there was significant doubt as to whether incumbent solar photovoltaic semiconductors, particularly silicon, would be sufficiently available, efficient, and affordable to meet the growing demand for solar cells. Chapter 1 is an introduction that frames some of the challenges with developing new semiconductor materials. In short, I encourage any researcher pursuing new materials to take a more holistic view of many material properties which contribute to photovoltaic performance rather than over-focusing on a single property to the exclusion of others.

This dissertation explores two distinct routes, one experimental and one computational, to achieving future photovoltaics with the potential for either higher efficiency or lower cost. Chapter 2 presents one of the first colloidal nanocrystal syntheses of a novel, earth-abundant semiconductor, FeS_2, better known as "fool's gold" or "iron pyrite". This particular synthesis is controlled by an aliphatic sulfonate ligand, a new ligand in the field of nanocrystal synthesis. In contrast, Chapter 3 takes a theoretical approach by using combinatorial density functional theory calculations to identify which dopants would be most likely to generate favorable electronic energy levels in zinc sulfide. The goal of the computation is to identify the dopant-matrix most likely to form the absorber layer for an intermediate band solar cell.

Lastly, Chapter 4 is an outlook that compiles a variety of categorical approaches, as well as specific techniques, for improving device efficiency and/or lowering costs. Since this field is sure to experience both incremental and step-change progress, keeping new approaches in mind is essential to planning future research activities.

Table of Contents

List of Figures

List of Tables

Chapter 1: Introduction

The Promise and Peril of Earth-Abundant Materials

Background & Motivation

When I began graduate school in 2008-2009, the solar photovoltaic industry was in a very different place than it is today. A number of today's emerging technologies, including perovskites and CZTS, hadn't hit the academic literature. CIGS and organics were suffering in the market and would ultimately be marginalized. The failure of Solyndra, a maker of CIGS modules, after a large government loan even became a political issue in the 2012 presidential election. CdTe hadn't yet emerged as a clear cost leader. Amorphous silicon was still popular and multi/polycrystalline silicon was viewed as the future of wafered silicon rather than more-expensive mono-crystalline wafers.

Around this time, the cost of poly-silicon, the input to the wafer-growing process, hit record prices. There was a genuine concern about what the semiconductor absorber would be that could take solar to the terawatt scale if silicon-based PV modules remained costly without subsidies in part due to their materials' cost. As history has since shown, that spikes and valleys in PV module prices were transient as the market demand and manufacturing capacity evolves and adjusts.

Overview of topics Covered

Chapters 2 and 3 represent original, first-author contributions to the field.

In Chapter 2, a liquid-phase synthesis for colloidal iron pyrite nanocrystals is described, along with structural and electronic characterization. This experimental report is one of the first controlled colloidal syntheses of iron pyrite nanocrystals and the only nanocrystal synthesis of any compound, to my knowledge, to make use of the sulfonate ligand. An extensive review of prior iron pyrite synthesis literature is included my master's thesis.

In Chapter 3, a combinatorial computational study is presented that identifies possible dopants in zinc blende-structure zinc sulfide for use as absorber layers in intermediate band solar cells. This work represents one of the first combinatorial studies using density functional theory to examine material properties for intermediate band solar cell absorbers. While zinc sulfide may not be an optimal solar material, the methodology demonstrated in the paper should be readily applied to other semiconductors, including GaP, 3C-SiC, and perovskites, that have more appropriate bandgaps.

The study of intermediate band solar cells was a reaction to changing market conditions. While there was interest, and a plausible commercial argument, for low-efficiency, low-cost solar cells when silicon was very expensive, only a few years later it became apparent that device efficiency is highly desirable because it is leveraged in other components of a solar power system. Intermediate band solar cells are one of several plausible concepts for reaching efficiencies greater than those of current silicon-based devices. Unfortunately, the central question required to begin an experimental materials synthesis—"What material should I make?"—was unknown, so the computational approach was selected as a precursor to future experimental materials synthesis.

Chapter 4 is an outlook on prospective technologies that may aid the photovoltaics industry in the near and distant future. Since my research contributions in Chapters 2 and 3 were at the cell level and were focused on materials science and optics, I limited my outlook to technologies in that domain. Of course, advances in 'balance of systems' will also play an important role in the continuing reductions in photovoltaic system costs.

Additional Considerations for New Semiconductors

When pursuing new semiconductor materials for photovoltaics, there are many criteria that must be simultaneously fulfilled if the device is going to have even modest efficiency. Drawing on lessons learned from my experiences of the last few years, I have briefly summarized some of the most important factors below. My hope is that future researchers will avoid over-emphasizing the pursuit of any single semiconductor property to the detriment of a more balanced and holistic view when assessing potential new materials.

Material Costs vs. Geological Abundance

One of the primary motivations for the pursuit of iron pyrite, detailed in Chapter 2, were the sky-high prices for poly-silicon at the time. An analysis at the time [1] addressed this issue by using geologic abundance, which is reported by the US Geological Survey and others, as a proxy for material cost. While there are certainly materials, such as precious metals, whose geological scarcity contributes to their high prices, a closer analysis shows that the mere abundance of a material does not necessarily mean it will be cheap. This difference is due to the costs of processing and purification. For example, the difference in price between metallurgical (>98% pure) and solar grade (>99.999% pure) silicon was a factor of at least 20x when I began my work and is still around 10x today. Using the same reasoning, metal oxides and metal sulfides, colloquially known as 'rust' and 'dirt', are indeed very geologically abundant but are unlikely to be significantly less expensive than other semiconductors once purified to electronic grade.

Regardless of the costs of extraction versus purification, materials costs have come to be a smaller share of the total cost of a solar module, at least when manufacturers using conventional wafer, evaporation, or sputtering processes. For example, NREL analysis shows the polysilicon cost for a typical single-junction Si modules is less than $0.04/watt for a $0.70/watt module. While that doesn't account for crystal growth, wafering, and cell processing, it's now clear the raw materials themselves are not driving the cost structure.

Bandgap

Bandgap is an important attribute of photovoltaic semiconductors. The widely-cited Shockley-Queisser limit [2] for solar cell efficiency makes a number of idealized assumptions that force the cell efficiency to be solely a function of bandgap. I think this has led to an over-emphasis on the importance of bandgap matching in assessing solar absorbers.

The optimal bandgap for a solar cell can indeed be modulated. Theoretical work by others at UC Berkeley[3] has shown that the addition of selective reflectors can red-shift the optimal bandgap. These systems compensate for the photons they block by driving higher photon densities within the device itself, which improves voltage. Such systems are thermodynamically sound, though it's unclear whether they would be realizable with real semiconductors, especially small bandgap ones, that suffer from greater Auger recombination at high carrier concentrations.

Indirect vs. Direct Optical Transitions

While material costs are often assessed on a gravimetric basis ($/kg), the cost of materials can be reduced if the device requires less material to adequately absorb sunlight. For instance, gallium arsenide (GaAs) is much more expensive that silicon, but since a solar cell only requires a few microns of GaAs as opposed to hundreds of microns of silicon there is a potential for significant savings since less GaAs is required than silicon. For this reason, volumetric cost of the material is probably a better metric than gravimetric cost, since optical absorption is inherently tied to volume, and must be further normalized bases on the absorptivity of a given volume of semiconductor. Of course, this analysis assumes the same precursor utilization rate for both materials. That may be difficult to compare since silicon and GaAs are processed using different technologies.

The silicon vs. GaAs analogy is an extreme case because it compares a direct to an indirect semiconductor. However, even within the direct bandgap semiconductors there is some difference in absorptivity. While higher absorptivity can have a direct savings by using a thinner absorber layer, an additional savings, which may be significantly larger than the material cost savings, is the increased manufacturing throughput afforded by a thinner semiconductor layer.

This could be especially important if the absorber is deposited in a physical vapor deposition process.

Some materials, such as iron pyrite, have especially strong absorption despite being indirect transition semiconductors. In the particular case of pyrite, this is especially surprising because the bandgap is thought to reside entirely in the 3d orbital, thus making it a forbidden transition.

Such an apparent anomaly could be explained several ways. First, the primary (indirect) transition could have another (direct) transition at a slightly higher energy. In this way an indirect bandgap material could have strong absorption. Since the bandgap energy is often extrapolated from a Tauc plot, closely spaced transitions may not be individually resolved. Second, interpretation of absorption data is further complicated by free carrier absorption in highly-doped semiconductors, such as iron pyrite, that extend the absorption redder than the actual bandgap would truly account for. Third, the apparent forbidden nature of the d-to-d transition may be circumvented if the bands are hybridized. Since many energy levels near the band edges contribute to the primary optical transition, it may be that some of those levels are hybridized and thus allow an overall optical transition. However, the hybridized states may not be the true band maximum/minimum which is typically analyzed in computational studies. In this way the bandgap may not be allowed but there is still strong optical absorption indistinguishably close to the bandgap.

Defects and Surface States

Another key challenge for semiconductor science is reduction of surface and bulk recombination. Reductions in recombination are important so that more photogenerated charge carriers can be extracted at the two electrodes. While it is a major achievement to prepare crystallographically-pure semiconductors, characterization techniques such as XRD, Raman, and electron microscopy cannot necessarily provide details about bulk and surface defects which can easily degrade semiconductor performance.

Fortunately, the quality of a semiconductor can be easily assessed by using time-resolving photoluminescence. If the material is available in several different thicknesses, both the bulk lifetime and the surface recombination velocity can be measured. This opens the way to rapid iteration of both chemical surface treatments as well as additive coatings than can suppress surface recombination. The bulk lifetime, when accounted for in the optimization of semiconductor growth, should yield material that is higher-performance than what would be anticipated by crystallography alone.

The most common earth-abundant materials, oxides and sulfides, have particularly challenging defect chemistry. Oxides tend to derive their n-type conductivity from oxygen vacancies. This can pose several challenges. If annealed at elevated temperatures, they can lose additional

oxygen and become more doped. On the other hand, some oxides are not stable under ambient conditions. For example, nano-sized zinc oxide will become less n-type (ie. more intrinsic) over time, presumably because it re-oxidizes in ambient conditions. Since most electronic devices desire stable dopant profiles over time, these time- and temperature-dependent changes in doping are not desirable.

Sulfides have similar challenges. For example, iron sulfides have many crystallographic phases with slightly different stoichiometries resulting in radically different material properties, such as being metallic or semiconducting. Sulfides are prone to loss of sulfur at elevated temperatures which limits their ability to be annealed as a means of improving their semiconductor properties. In the particular case of iron pyrite, the disulfide (S_2^{2-}) is thought to generate a charge-neutral, bulk vacancy defect by forming S^{2-}.

At the surface there are additional challenges with sulfides. Since most metals form metal sulfides, any deposition of metal on the metal sulfide, such as to form an electrode contact, can instead extract sulfur from the semiconductor to form an interfacial metal sulfide layer. Not only can these interfacial metal sulfides distort conduction pathways, but by extracting sulfur from the semiconductor they can also modify the semiconductor. A sulfur-deficient material may, as in the case of iron sulfide, no longer be semiconducting. In this way, deposition of the metal contact produces Fermi level pinning and introduces surface states.

Modulation of doping

The highest efficiency devices are typically homojunctions of the same material. This is due in part to their lack of any band offsets, which maximizes their voltage. However, a homojunction requires that the semiconductor be able to be doped both n- and p-type. Unfortunately, few of the new semiconductors, including CdTe, CIGS, CZTS, Zn_3P_2, and the perovskites, show such facile doping. Even worse, iron pyrite in nanocrystalline form has been shown to be degenerately doped, meaning its conductivity is more metallic than semiconducting.

Even when ambipolar doping is not required due to the use of heterojunctions, there are still some cases, most famously in CdTe, where even the degree of one type of doping is difficult to modulate. In the case of CdTe, additional doping (ie. more heavily p-type) is desirable in order to increase V_{oc}. Future investigations of semiconductors must ensure that doping can be modulated, preferably in both types.

The Tradeoff between Materials Costs, Material Quality, and Capital Costs

At the conclusion of this work, it's apparent that there is a tradeoff to be made between cost and quality of materials, their deposition, and device performance. At some point it might be commercially practical to achieve a low capital intensity ($/Watt) solar cell by using low-grade

materials deposited using a low-cost process. However, given the current state of the solar manufacturing industry, material cost has become proportionally less important in the cost structure compared to the depreciation expense of capital equipment. This suggests that methods using cheaper deposition and/or manufacturing processes to produce the same material might be more technologically and commercially relevant.

In this area, solution processing or other more direct deposition methods may still be relevant due to their lower capital intensity compared to vacuum techniques. For instance, chemical bath deposition is used for depositing the emitter on thin film solar cells. There may be advantages to solar cells deposited entirely by chemical bath deposition. In a similar method, electrodeposition, which uses an electric current to induce deposition from solution, could be similar lower cost relative to vacuum systems. In an analogous innovation in the wafered silicon industry, a startup company, Crystal Solar, has had success directly growing epitaxial, mono-crystalline directly from silane. Their process bypasses the need to reduce the silane back to solid silicon, grow an ingot, and finally dice the ingot. In this way, new deposition methods for established materials may be a promising way to introduce new technology to incumbent players.

References

[1] C. Wadia, a P. Alivisatos, and D. M. Kammen, "Materials availability expands the opportunity for large-scale photovoltaics deployment.," *Environ. Sci. Technol.*, vol. 43, no. 6, pp. 2072–7, Mar. 2009.

[2] W. Shockley and H. J. Queisser, "Detailed Balance Limit of Efficiency of p-n Junction Solar Cells," *J. Appl. Phys.*, vol. 32, no. 3, p. 510, 1961.

[3] a. Niv, Z. R. Abrams, M. Gharghi, C. Gladden, and X. Zhang, "Overcoming the bandgap limitation on solar cell materials," *Appl. Phys. Lett.*, vol. 100, no. 8, p. 083901, 2012.

Chapter 2:
Ligand-Controlled Colloidal Synthesis and Electronic Structure Characterization of Cubic Iron Pyrite (FeS_2) Nanocrystals

Based on published work:
J. Matthew Lucas, Chia-Chi Tuan, Sebastien D. Lounis, David K. Britt, Ruimin Qiao, Wanli Yang, Alessandra Lanzara, A. Paul Alivisatos, *Chem. Mater.*, 2013, 25 (9), pp 1615–1620

Abstract

Iron pyrite (FeS_2) is a promising photovoltaic absorber due to its Earth abundance, high optical extinction, and infrared bandgap (E_g = 0.95 eV), but its use has been hindered due to the difficulty of phase-pure synthesis. Pyrite phase purity is a paramount concern, as other phases of iron sulfide have undesirable electronic properties. Here we report the synthesis of phase pure iron pyrite nanocrystals with cubic morphology and mean dimension of 80nm. Control over the nanocrystal shape was achieved using an unusal ligand, 1-hexadecanesulfonate. The particles were characterized with synchrotron X-ray spectroscopy, indicating an indirect bandgap of 1.00 +/- 0.11 eV and valence bandwidth of nearly 1eV. Transmission electron microscopy from early reaction stages suggest a nucleation and growth mechanism similar to solution precipitation syntheses typical of metal oxide nanocrystals, rather than the diffusion-limited growth process typical of hot-injection metal chalcogenide nanocrystal syntheses.

Background & Motivation

Iron pyrite (FeS_2) shows great promise as a photovoltaic absorber material due to its Earth abundance [1], lack of toxicity, appropriate bandgap (E_g = 0.95 eV)[2], and high optical extinction ($\alpha > 10^5$ cm^{-1} in the visible) [3]. However, thin film fabrication for photovoltaic applications has been unsuccessful. Other crystallographic phases of iron sulfide form readily, leading to an exceptionally narrow phase space for iron pyrite formation[3-5]. Phase purity is necessary for effective photovoltaic devices because the different phases of iron-sulfide have very different optoelectronic properties, most being metallic or semi-metallic rather than semiconducting. Since the first report of an iron pyrite energy conversion device in 1984[6] and the highest efficiency devices in 1991[7], device efficiency has not improved in the last 20 years.

For a high efficiency iron pyrite device, the absorber layer must be thick enough to absorb sufficient sunlight while maintaining a single-crystalline pathway for charge transport to minimize recombination and maximize mobility. Given pyrite's absorption coefficient of 2-3 x 10^5 cm^{-1} above the bandgap, optical absorption lengths are 35-50nm. Since complete extinction requires at least two optical lengths, an optimal pyrite absorber would be 70-100nm. Wet chemical colloidal syntheses of phase pure iron pyrite nanocrystals have been reported

recently, using a variety of approaches, including hydrothermal synthesis[8, 9], solvothermal synthesis[10], hot injection[11-16], and thermal decomposition[17]. Nanowires have also been produced[18], although it's not evident the light-trapping effect of nanowires is necessary given pyrite's strong absorption. Thin films have also been prepared by non-colloidal methods.[19] While these syntheses all produce pyrite-phase material, their sizes are often too big or too small to form a monolayer film needed to provide a single-crystal path for charge collection. The nanocrystals synthesized here are 80nm on average, within the optimal range for a monolayer absorber.

Here we present a colloidal synthesis of cubic nanocrystals with dimensions of 80nm, on the order of the optical absorption length for iron pyrite. This synthesis utilizes an uncommon ligand in hot-injection nanocrystal synthesis, 1-hexadeanesulfonate, to achieve shape control. To the best of our knowledge, the use of this ligand has never been reported before for shape control in any colloidal nanocrystal system. We used X-ray spectroscopies to measure an indirect gap of 1.00eV +/- 0.11eV and characterize the curvature of the valence band. The growth mechanism for this reaction is found to be very different from those of other hot-injection syntheses, bearing strong parallels to aqueous colloidal precipitation reactions.

Imaging and Structural Characterization

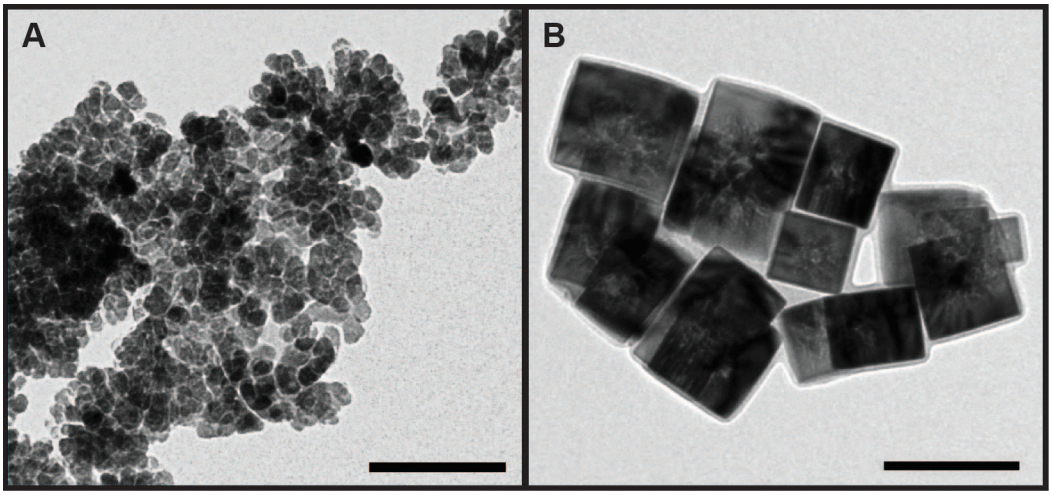

Figure 2.1. Nanocrystals made without (a) and with (b) 1-hexadecanesulfonate. Scale bar is 100 nm.

Nanocrystals were synthesized using a hot injection of sulfur and sodium hexadecanesulfonate in oleylamine into $FeCl_3$ in oleylamine at 220° C (see Methods for details). TEM images in Figure 2.1 show the singular impact of the sulfonate ligand on particle morphology. The left pane shows typical nanocrystals synthesized without the ligand, while the right pane shows an equivalent synthesis with the sulfonate ligand (mean 80nm +/- 20% from TEM analysis). All reaction conditions and reagents are otherwise identical between the two syntheses.

In the course of our investigation, we tried substituting a variety of different alkyl length and functional ligands including: carbamates, carboxylic acids, xanthates, trithiocarbonates, primary & secondary amines, and primary thiols. We also tried phenyl diamines and large molecular weight surfactants such as polyvinylpyrrolidone and Triton X-100. In all cases, shape and size control were not achieved. At higher concentrations, many surfactants disturb the phase purity of the nanocrystals, as evidenced from PXRD.

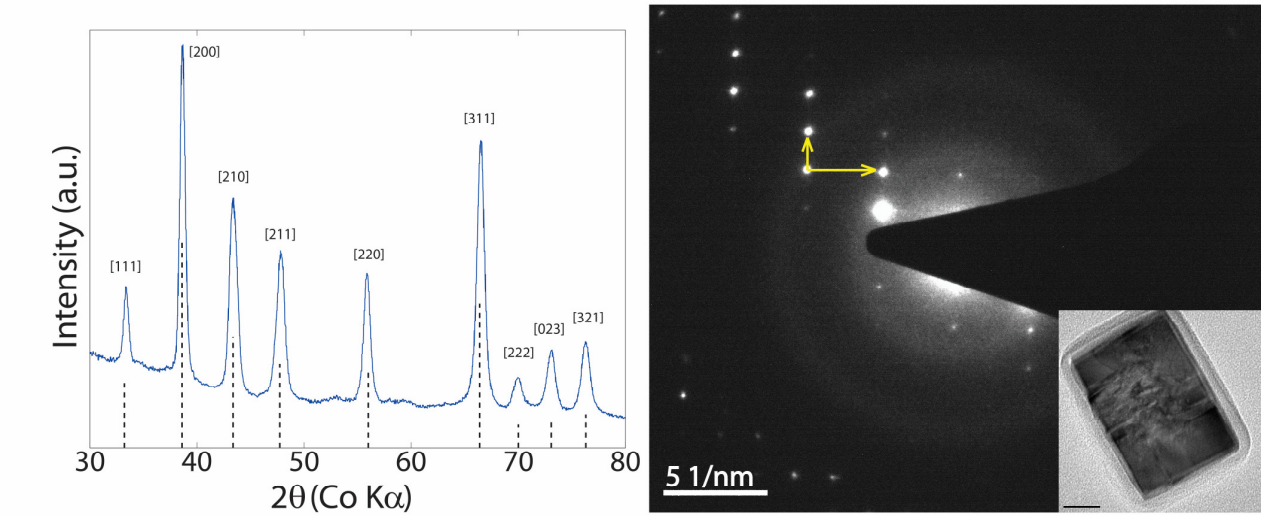

Figure 2.2. X-ray diffraction matches reference for iron pyrite (JCPDS 42-1340). Selected area electron diffraction with overlaid vectors show imaging is along the [100] zone axis. Inset: Nanocrystal characterized by SAED. Scale bar in inset is 20 nm.

Peak positions in powder XRD (Figure 2.2, left) agree with those in JCPDS file 42-1340 (iron pyrite, FeS_2). Williamson-Hall analysis[20] (not shown) against an annealed Al_2O_3 powder standard confirm the peak width is equal to instrumental resolution. Raman spectroscopy (Figure 2.3) confirms the purity of the iron pyrite. Selected area electron diffraction (SAED, Figure 2.2, right) shows that the particles are monocrystalline, despite inconsistent contrast in the TEM imaging. Contrast within the particle could be due to dislocations or strain induced by imperfect stoichiometry.[21] Electron microscopy is known to modify samples, for example by changing the oxidation state of metal ions or displacing atoms, so it is not possible to distinguish defects resulting from imaging from those due to synthesis. Furthermore, pyrite also has a tendency to lose sulfur under elevated temperature and reduced pressure[3], so imaging may lead to sub-stoichiometric nanocrystals which may evolve further defects. Modeled SAED patterns [22] indicate imaging along the [100] zone axis. Since the particles are cubic, this indicates the exposed facet is [100]. The layer surrounding the particles, as seen in Figures 2.1, 2.2, and 2.10, is most likely a combination of hexadecanesulfonic acid and oleylamine. It does not diffract under SAED. The particles must be cleaned gently or they will irreversibly precipitate from solution (see Methods for details), which suggests the hexadecanesulfonic acid does not bond very strongly. The need for solubility must be balanced against the desire to further remove the viscous oleylamine solvent. It's also possible that the

layer is an amorphous Fe-S species. However, we did not observe the layer diminish at longer reaction times when it would have had ample opportunity to crystalize. Additional cleaning steps that reduce the particles' solubility also diminished the layer, which is consistent with it being an organic surfactant.

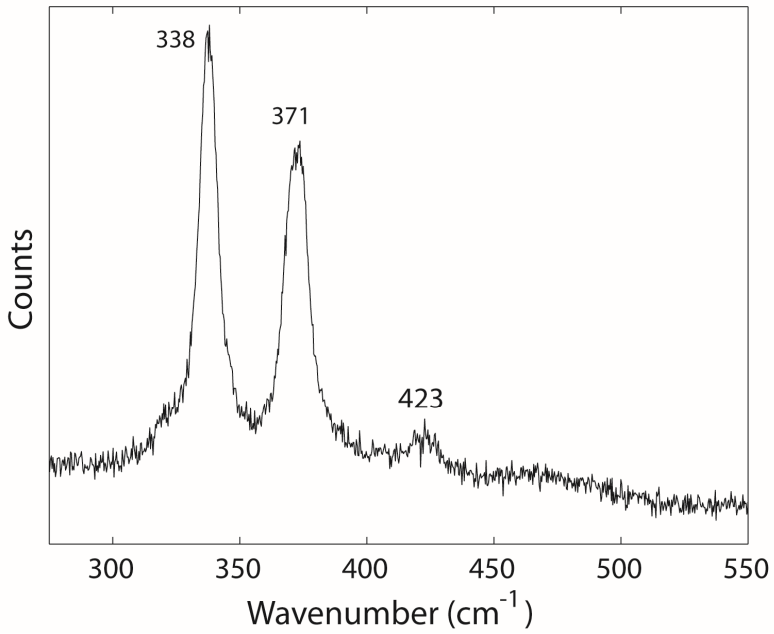

Figure 2.3. Raman spectrum of pyrite nanocrystals excited at 632nm. The three peaks match known pyrite features.[19]

1-Hexadecanesulfonate has not been previously reported to confer shape control in hot-injection nanocrystal syntheses. Of the few reports of sulfonate binding to nanocrystals,[23-25] none was based on hot-injection syntheses or achieved shape control. Sulfonates are routinely found in nanoparticle synthesis as a means to confer water solubility by presenting an anionic functional group to solution.[26, 27] In those cases, the sulfonate group is not bound to the particle. In contrast, the sulfonate is the likely binding entity in the present reaction as there is no other coordinating functionality on the ligand.

IR absorption spectra of oleylamine, hexadecanesulfonic acid sodium salt, and the particles are shown in Figure 2.4. Both the sulfonate and the oleylamine can act as surface ligands, but both ligands have overlapping features in IR. IR transmission spectra of nanocrystals shows peaks around 2950, 2800, 2700, 1450, and 1170 cm^{-1}. There is no peak above 3000 cm^{-1}. The peak at ~1170 cm^{-1} in the sulfonate spectrum is attributed to S=O stretch. The peak around 1200 cm^{-1} is a shifted and broadened S=O stretch, which is consistent with sulfonate binding. The absence of peaks above 3000 cm^{-1} is consistent with an absence of C=C bonds, which suggests oleylamine is not present in the nanocrystal sample. Other peaks are shared between both the amine and sulfonate spectra and so are not uniquely identifying. Thus, we can picture the nanocrystal surface as being covered by both 1-hexadecanesulfonate with at most trace oleylamine.

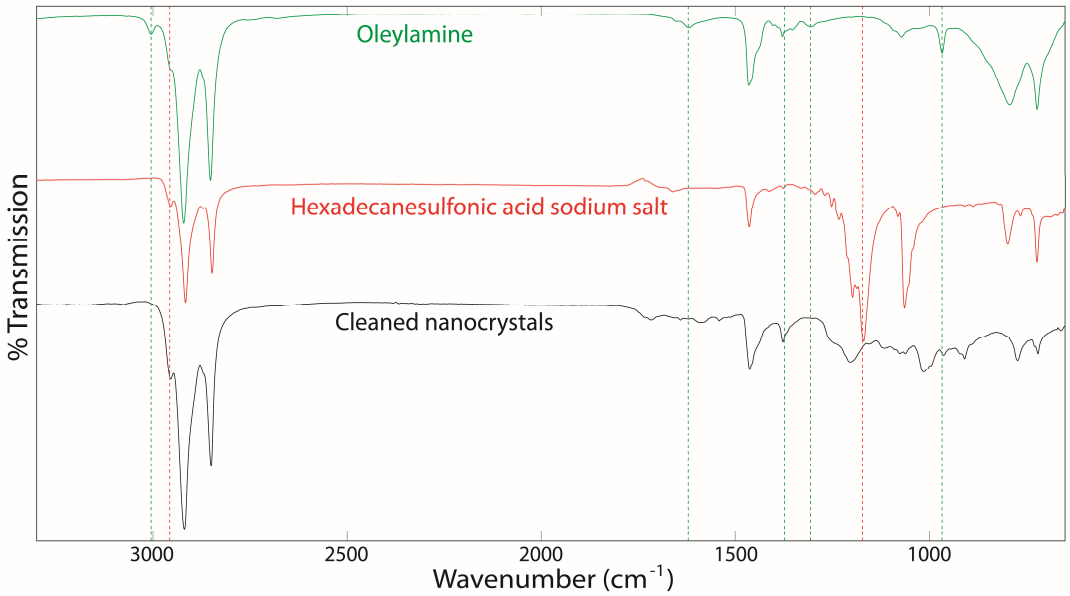

Figure 2.4. IR spectra of oleylamine, hexadecanesulfonic acid sodium salt, and nanocrystals. The color-coded, dashed vertical lines denote unique features of oleylamine or sulfonate, respectively.

Opto-Electronic Structural characterization

The size of the bandgap in iron pyrite nanocrystals has been difficult to measure since many works have significant aggregation and scattering.[13, 15] While aggregates may provide additional opportunities for light trapping, they complicate colloidal measurement of optical properties. Furthermore, bandgaps derived from optical methods can be deceiving, especially for degenerate semiconductors such as iron pyrite. For example, InN was long thought to have a large bandgap of 1.9 eV based on optical measurements, but the fundamental bandgap was later found to be only 0.7 eV.[28, 29] Electronic measurement of the bandgap is not susceptible to the Burstein-Moss effect that skewed the measurement of InN. To our knowledge, this is the first electronic measurement of the bandgap of nanocrystal iron pyrite.

The nature of the pyrite bandgap is also intriguing because of its sharp turn-on and high absorption coefficient appears qualitatively more similar to direct rather than indirect bandgap materials. Computational studies[30, 31] have been used to identify the nature of the transition and effects of impurities, but to our knowledge, the nature of nanoscopic pyrite's bandgap has never been investigated experimentally.

We employed X-ray spectroscopy to measure the bandgap, determine the nature of the transition, and qualitatively evaluate the valence band curvature of the pyrite nanocrystals. The UV-Vis absorption spectrum (Figure 2.6) of the nanoparticles is consistent with the X-ray data, but less informative, as it is rather featureless and convoluted with scattering from aggregation.

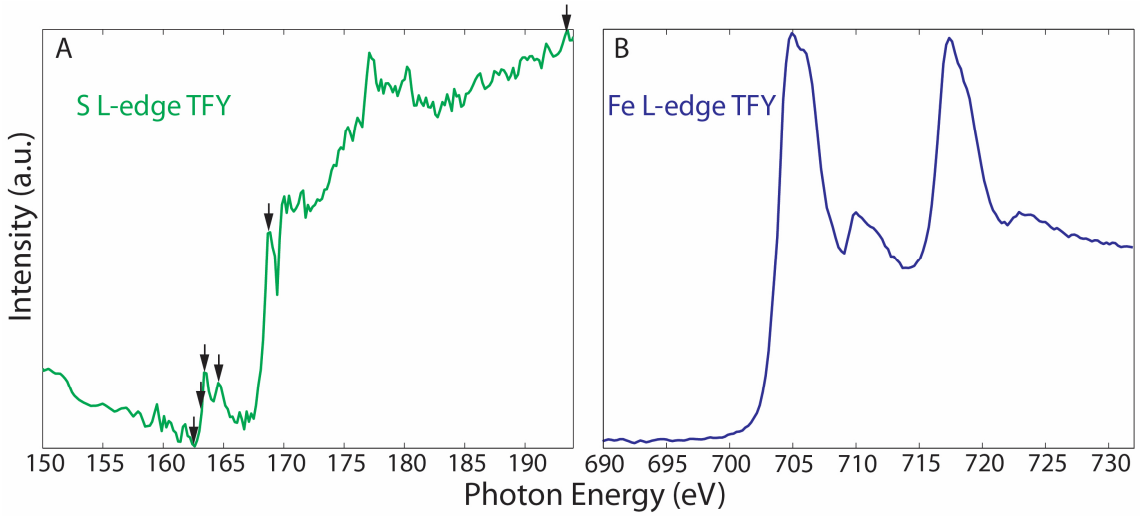

Figure 2.5. Left: X-ray absorption for FeS_2 nanoparticles on the S-L edge measured in total fluorescence yield. Arrows indicate excitation energies used for RIXS measurements shown in Figure 2.7. Right: X-ray absorption on Fe-L edge.

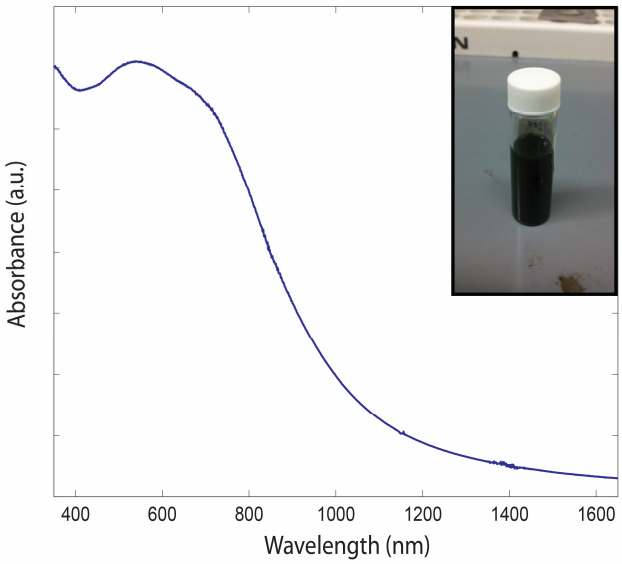

Figure 2.6. UV-Vis absorption in solution shows a strong absorption onset in the near infrared as expected, but scattering background makes interpretation of a bandgap difficult.

X-ray absorption spectroscopy (XAS) on both the sulfur (Figure 2.5a) and iron L-edges (Figure 2.5b) effectively maps the transition-allowed density of unoccupied states by exciting electrons from core levels to the conduction band. Both spectra are consistent with previous measurements in the literature of micro-sized iron pyrite particles.[8] Based on XAS spectra, six energies, denoted by arrows in Figure 2.5a, were chosen for Resonant Inelastic X-ray Scattering (RIXS) analysis. The first three arrows, indicating energies of 162.5 eV, 163 eV and 163.5 eV, are situated along the sulfur-L absorption edge, allowing observation of conduction and valence band near-edge behavior. The following arrows sit on additional peaks, the first arising from

the spin-orbit split L_3 feature at 164.5 eV, and the second a strong peak at 169 eV due to excitation of extended S-3s states. Finally, the normal X-ray emission spectrum (NXES) was measured well above threshold at 194.5 eV to determine the overall density of states. These absorption maxima are chosen to investigate specific features of the electronic structure and to optimize signal strength during the measurement.

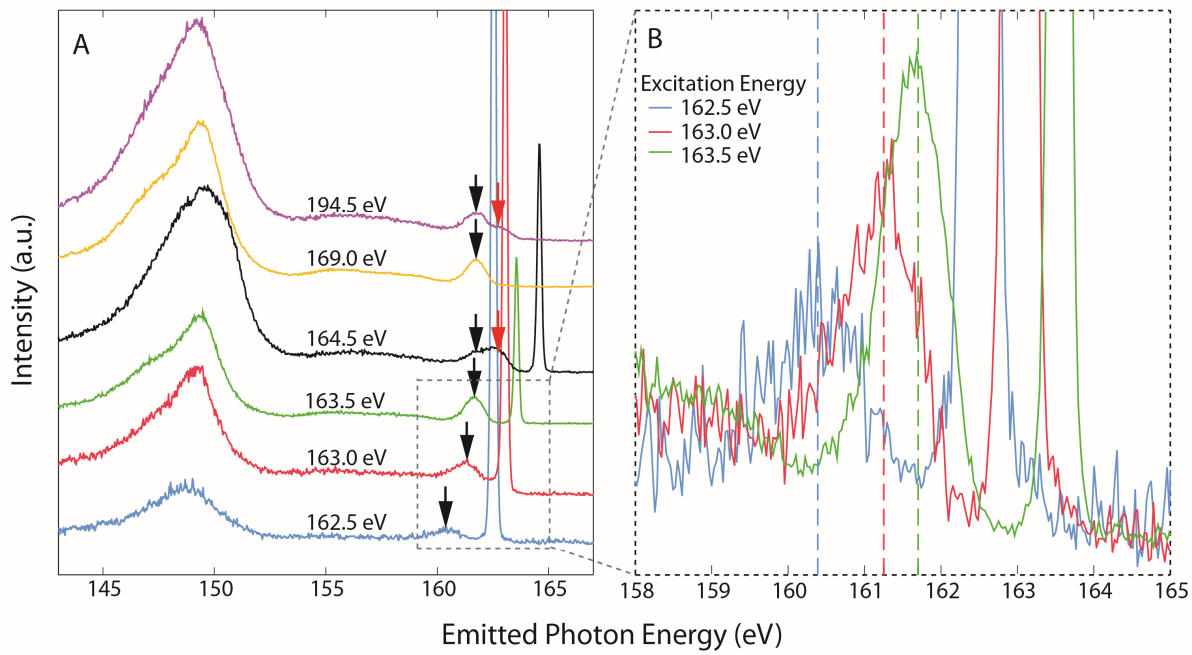

Figure 2.7. (a) RIXS and NXES emission spectra at the excitation energies listed. Black arrows denote the scattering from the valence band. Red arrows denote a second resonance that arises due to spin-orbit splitting. Sharp peaks at higher energies are due to elastic features. (b) Overlaying three RIXS spectra from Figure 2.7a shows an increase in emission energy over excitation photon energies.

RIXS and NXES spectra (Figure 2.7a) of FeS_2 nanoparticles have peak structure and emission energy values that are consistent with previously published work for larger nanoparticles[8] and thin films[32]. Spectra are normalized to the maximum of the resonant feature indicated by the black arrows. The sharp peaks at higher emission energy are due to elastic scattering of the incident photon beam. During a RIXS process, a specific core electron is resonantly excited to a specific unoccupied state. The same core hole is involved in the subsequent decay event and crystal momentum is preserved throughout the RIXS process. This coherence allows the experimenter to use the excitation energy as a k-selective probe of the band structure. A simplified schematic of this technique can be found in the Supporting Information.

The resonant peaks in Figure 2.7a (indicated by black arrows), which correspond to the valence band, shift toward higher energy with increasing excitation energy. Figure 2.7b highlights three RIXS spectra taken at excitation energies between 162.5 eV and 163.5 eV along the sulfur L-edge. The shift of the resonant peak's emission energy to higher values is indicative of an

indirect bandgap. [33, 34] The relatively small shift in the resonant peak's energy with the change in excitation energy can be interpreted as the curvature of the valence band, which here demonstrates a band width of about 1 eV. This relatively flat band is consistent with an effective mass approximation understanding of observations of very low mobility in p-type pyrite films.

Below the high intensity elastic peaks, the next lowest feature on the energy scale, appearing between approximately 160 – 164 eV and marked by black arrows in Figure 2.7a, is due to resonant inelastic scattering from the top of the valence band in FeS_2 and arises from S 3d – Fe 3d orbital hybridization to the S L_3 $2p_{3/2}$ core level.

As can be seen for excitation at 164.5 eV, a corresponding second peak, marked by red arrows in Figure 2.7a, appears in this resonant feature at a blue shift of ~1 eV when resonating on the spin-orbit split S L_2 $2p_{1/2}$ core level and also for normal emission far above threshold. The spin-orbit splitting is also manifested in the shoulder at ~151 eV seen on the large, low energy peak for the same excitation energy

The sharp peaks at higher emission energies are due to elastic scattering of the incoming beam. These peaks are used to calibrate the energy scales used in XAS/XES and RIXS plots and to determine the resolution for each spectrum.

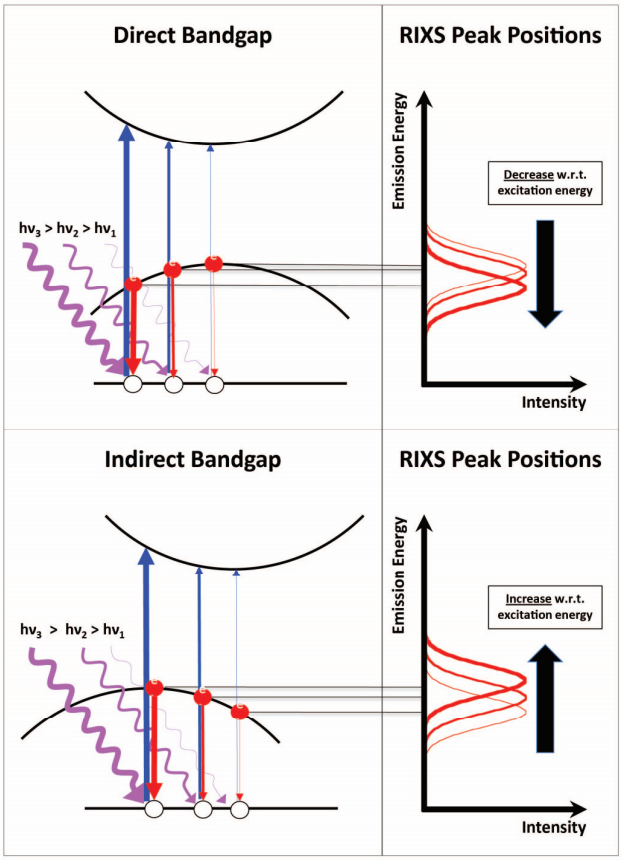

Figure 2.8. Schematic illustration of how RIXS spectra can be used to determine the nature of the bandgap transition.

Figure 2.8 shows a schematic cartoon of the RIXS process as it is used to determine band structure information. In a RIXS measurement (relative to a conventional XES measurement) the inlet slits on the synchrotron beamline are narrowed to confine the energy envelope of the photon beam incident upon the sample within a range allowing excitation of specific transitions in the electronic structure. While this reduces flux, the resonance effect increases signal enough to allow sufficient statistics within a reasonable scan time. (New spectrometers allow much faster measurements, enabling more detailed characterization of band structures[47]). Because a specific core-level to unoccupied state transition is being excited, the same core hole is involved in the subsequent emission event and the crystal momentum is preserved throughout the RIXS process. This coherence allows the experimenter to use the excitation energy as a k-selective probe of the band structure, as depicted in the cartoon. In particular, the expected trend of emission peaks for direct and indirect semiconductors is opposite, giving an unequivocal differentiator for this property within the experimental resolution.[48-50]

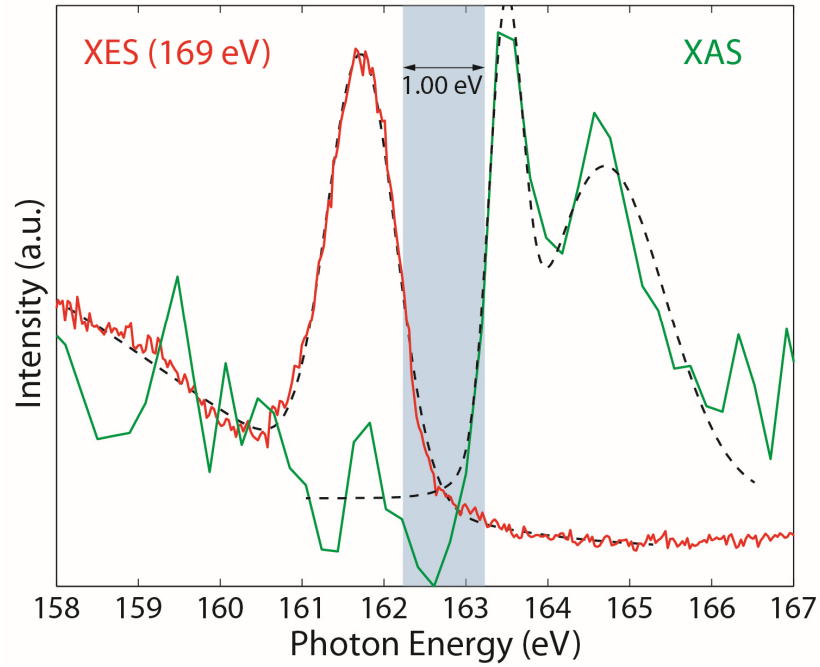

Figure 2.9. X-ray absorption-emission spectroscopy shows the electronic bandgap is 1.00 +/- 0.11 eV. The green XAS spectrum maps the transition-allowed conduction band density of states while the red resonant emission spectrum does the same for the valence band.

Figure 2.9 combines XAS data from Figure 2.5a and RIXS data from Figure 2.7a to approximately quantify the electronic bandgap. The conduction band edge, mapped by XAS on the sulfur L-edge, is overlaid with the emission spectrum from resonant excitation at 169.0 eV, which maps the valence band. Excitation at 169 eV leads to emission very near the valence band maximum, which can be confirmed by comparison to the peak position in the above-threshold NXES spectrum. This particular RIXS spectrum was chosen to determine the band gap, instead of the

NXES spectrum, because of the strong suppression of the spin-orbit peak (red arrows) at this resonance. With excitation from the $2p_{1/2}$ level suppressed, the resonant peak arising from transitions to the $2p_{3/2}$ core level can be compared directly to the absorption threshold of the same core-level to determine the bandgap.

The bandgap is conventionally estimated by taking the difference between the energy values at the half-max of each feature. We found a value of 1.00 +/- 0.11 eV, which is within experimental error of the accepted value of 0.95 eV.[3] The error in this measurement, calculated by fitting the elastic features of the spectra and comparing to the excitation energy, reflects the experiment resolution of 0.1 – 0.2 eV.

Observations on Reaction Mechanism

Formation of the iron pyrite phase requires in-situ reduction of Fe^{3+} to Fe^{2+}, which is the oxidation state of iron in FeS_2. Candidate reducing agents include the double bond in the oleylamine chain, the amine group itself, or the sulfur. Puthessery et al[11] used an aliphatic amine, rather than oleylamine, in their hot injection synthesis of iron pyrite. Their result suggests the unsaturated alkyl chain is not the reducing agent. However, amines have been shown to act as reducing agents in other nanocrystal syntheses.[35] Sulfur cannot be dismissed as the reducing agent, but sulfur-amine interactions are still a matter of investigation[36] and swapping the sulfur reagent would be expected to change the reaction, even if it were not the reducing agent.

This in-situ reduction is likely present in other amine-based iron pyrite syntheses, even though those reaction utilize Fe^{2+} salts. Only Fe^{3+} is soluble in oleylamine. Whereas anhydrous $FeCl_2$ combined with dry and degassed oleylamine failed to dissolve after stirring overnight at 100° C, anhydrous $FeCl_3$ under the same conditions dissolves almost immediately to yield a black solution typical of the iron-oleylamine complex. Both iron chlorides dissolve when the test is repeated in ambient. Given that Fe^{2+} oxidizes to Fe^{3+} instantaneously in aqueous solution, it is assumed that residual water and dissolved oxygen in oleylamine and the atmosphere oxidize Fe^{2+} to Fe^{3+}.

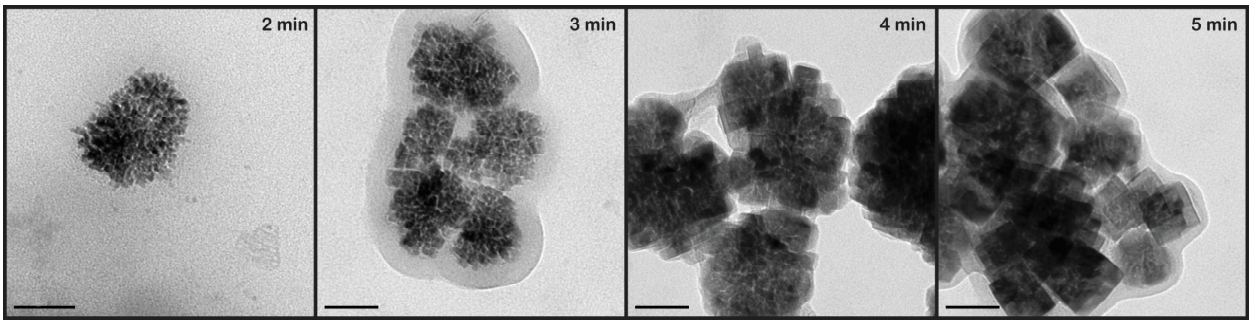

Figure 2.10. TEM micrograph of reaction aliquots. Aggregates of many small crystals gradually fuse to single crystal domains over time. Scale bar is 50 nm.

An unusual growth pattern is observed in a time-series of TEM images (Figure 2.10) taken at the earliest possible time points when crystallites could be observed by TEM. Small nuclei have agglomerated into polycrystalline structures, whose crystalline nature was verified by SAED. PXRD of the reaction product at these time points did not show diffraction peaks, which is consistent with a sample that has a large volume fraction of amorphous material and at most a small fraction of polycrystalline agglomerates. At later time points, however, PXRD shows diffraction peaks, which suggests the amorphous fraction is converted into crystalline particles over time. At those time points, the agglomerates in Figure 2.10 also fuse to form single-domain nanocrystals, like those in Figure 2.1b. Observation of growth from an amorphous matrix was also found in the work of Puthussery et al.[11]

We observe a mechanism in which small nuclei ("primary particles") rapidly clump to form aggregates ("secondary particles"). This mechanism is characteristic of precipitation syntheses, but not of typical hot injection syntheses.[37, 38] In a precipitation synthesis, a lack of repulsion between primary particles, due to an organic species for instance, favors coalescence of the primary particles into secondary particles. In our system, this coalescence is evident because discrete primary nuclei are not observed. Prior modeling from literature assumes that primary particles have much larger diffusion constants than secondary particles, thus attachment and aggregation of primary particles is thought to drive growth, as opposed to diffusional growth from solutes.[39] This coalescence is not typical of hot injection nanocrystal syntheses, but has been reported in the precipitation literature.[40] In contrast to this aggregration mechanism, a typical hot injection synthesis is characterized by diffusion-limited growth, first published by LaMer[41, 42], resulting in a "burst" of nucleation followed by independent, uniform, diffusion-limited growth of these nucleates which is controlled only by the concentration of reactants in solution.[43, 44] In the present reaction, the amorphous phase is fully converted to crystalline particles within a few minutes. The combined effect of primary particle aggregation and nucleation from amorphous phase is that the "burst" in the diffusion-limited mechanism is a gradual process in our synthesis.

The identification of an agglomeration mechanism has consequences for our control of the present reaction. In aqueous precipitation syntheses, the secondary particle formation is controlled by ionic strength, pH, temperature, polymer mediators, and the anion of the metal salt, all of which combine to modulate the attraction between primary particles.[45, 46] Though the use of oleylamine solvent limits our ability to explore this parameter space, we found reaction temperature cannot be reduced more than 30 °C without affecting phase purity and overall reaction concentration cannot be lowered by more than a factor of two before nucleation fails to occur within two hours. We also made an effort to separate the primary nuclei from each other and prevent aggregation by dilution of the reaction mixture at early time points, but this did not prevent secondary particle formation.

We've presented a colloidal synthesis of cubic FeS_2 nanocrystals using the ligand 1-hexadecanesulfonate and characterized the product using X-ray spectroscopies to help resolve disagreement over the size and nature of the electronic bandgap. The growth mechanism for

this reaction is found to be very different from those of other hot-injection syntheses, bearing strong parallels to aqueous colloidal precipitation reactions.

Methods

Iron pyrite nanocrystals were prepared by the following method. All chemicals were used as received. 5mL oleylamine (Acros, 80-90%) was dried under vacuum at 120° C, then transferred using air-free technique to a nitrogen-purged vial containing 96 mg (3 mmol) sulfur (Aldrich, sublimed) and 328 mg (1 mmol) 1-hexadecanesulfonic acid sodium salt (Aldrich, 98%), hereafter referred to as Solution A. Solution A was stirred at 90° C until dissolution of the sulfur and sulfonate, forming a deep red solution. Separately, 10 mL oleylamine and 81 mg (0.5 mmol) anhydrous $FeCl_3$ (Aldrich) were combined in a 3-neck flask and degassed under vacuum at 120° C for 1 hour, hereafter referred to as Solution B. After switching to an argon atmosphere, Solution B was heated to 220° C and Solution A was swiftly injected (< 1 s). We found the smallest size dispersity and sharpest cubes when the reaction temperature dropped the least upon injection (no lower than 195° C). After 10 minutes the heating mantle was removed and the reaction was allowed to cool to less than 100° C, at which point it was diluted with chloroform and methanol (~2:1) and transferred to a centrifuge vial. The particles were precipitated by centrifuging for 4 minutes at 4,000 rpm (2600 g), then resuspended in chloroform for storage. Note that additional methanol or centrifugation steps may cause the particles to lose their solubility.

The nanocrystals were characterized by X-ray diffraction (XRD), selected area electron diffraction (SAED), transmission electron microscopy (TEM), optical absorption, soft X-ray absorption-emission spectroscopy (XAS-XES), resonant inelastic X-ray scattering spectroscopy (RIXS), infrared spectroscopy (IR), and proton nuclear magnetic resonance (NMR).

TEM and SAED images were taken on a Tecnai G2 Super-Twin transmission electron microscope with a LaB_6 thermionic emission filament. Samples were prepared by dipping a TEM grid in a dilute solution of nanocrystals in chloroform. XRD patterns of the precipitated nanocrystals were taken on a Bruker D8 GADDS diffractometer with a cobalt source ($K\alpha_1$ = 1.79 Å). Optical absorption was taken with a Shimadzu UV-3600 spectrophotometer. IR transmission was taken with a Perkin-Elmer FT-IR with HATR assembly from dropcast and dried solutions of nanocrystals in chloroform.

XAS spectra were collected through total fluorescence yield (TFY) and total electron yield (TEY) at beamline 8.0.1 (BL8.0.1) of the Advanced Light Source (ALS) at Lawrence Berkeley National Laboratory. TFY data were used for our analysis because of the enhanced bulk sensitivity relative to TEY. RIXS measurements were collected using a Rowland circle spectrometer.

References

1. Wadia, C., A.P. Alivisatos, and D.M. Kammen, *Materials Availability Expands the Opportunity for Large-Scale Photovoltaics Deployment.* Environmental Science & Technology, 2009. **43**(6): p. 2072-2077.
2. Altermatt, P.P., et al., *Specifying targets of future research in photovoltaic devices containing pyrite (FeS2) by numerical modelling.* Solar Energy Materials and Solar Cells, 2002. **71**(2): p. 181-195.
3. Ennaoui, A., et al., *Iron Disulfide for Solar-Energy Conversion.* Solar Energy Materials and Solar Cells, 1993. **29**(4): p. 289-370.
4. Hopfner, C., et al., *Stoichiometry, Phase and Orientation-Controlled Growth of Polycrystalline Pyrite (Fes2) Thin-Films by Mocvd.* Journal of Crystal Growth, 1995. **151**(3-4): p. 325-334.
5. Soukup, R.J., et al., *Formation of pyrite (FeS(2)) thin films by thermal sulfurization of dc magnetron sputtered iron.* Journal of Vacuum Science & Technology A, 2011. **29**(1).
6. Ennaoui, A. and H. Tributsch, *Iron Sulfide Solar-Cells.* Solar Cells, 1984. **13**(2): p. 197-200.
7. Antonucci, V., et al., *Photoactive Screen-Printed Pyrite Anodes for Electrochemical Photovoltaic Cells.* Solar Cells, 1991. **31**(2): p. 119-141.
8. Wadia, C., et al., *Surfactant-Assisted Hydrothermal Synthesis of Single phase Pyrite FeS(2) Nanocrystals.* Chemistry of Materials, 2009. **21**(13): p. 2568-2570.
9. Wang, D.W., Q.H. Wang, and T.M. Wang, *Controlled growth of pyrite FeS2 crystallites by a facile surfactant-assisted solvothermal method.* Crystengcomm, 2010. **12**(3): p. 755-761.
10. Yuan, B.X., W.L. Luan, and S.T. Tu, *One-step synthesis of cubic FeS2 and flower-like FeSe2 particles by a solvothermal reduction process.* Dalton Transactions, 2012. **41**(3): p. 772-776.
11. Puthussery, J., et al., *Colloidal Iron Pyrite (FeS(2)) Nanocrystal Inks for Thin-Film Photovoltaics.* Journal of the American Chemical Society, 2011. **133**(4): p. 716-719.
12. Bi, Y., et al., *Air Stable, Photosensitive, Phase Pure Iron Pyrite Nanocrystal Thin Films for Photovoltaic Application.* Nano Letters, 2011. **11**(11): p. 4953-4957.
13. Li, W., et al., *Pyrite nanocrystals: shape-controlled synthesis and tunable optical properties via reversible self-assembly.* Journal of Materials Chemistry, 2011. **21**(44): p. 17946-17952.
14. Macpherson, H.A. and C.R. Stoldt, *Iron Pyrite Nanocubes: Size and Shape Considerations for Photovoltaic Application.* Acs Nano, 2012. **6**(10): p. 8940-8949.
15. Kirkeminde, A., et al., *Synthesis and Optoelectronic Properties of Two-Dimensional FeS2 Nanoplates.* ACS Applied Materials & Interfaces, 2012. **4**(3): p. 1174-1177.
16. Lin, Y.Y., et al., *Extended red light harvesting in a poly(3-hexylthiophene)/iron disulfide nanocrystal hybrid solar cell.* Nanotechnology, 2009. **20**(40).
17. Sines, I.T. and R.E. Schaak, *Phase-Selective Chemical Extraction of Selenium and Sulfur from Nanoscale Metal Chalcogenides: A General Strategy for Synthesis, Purification, and Phase Targeting.* Journal of the American Chemical Society, 2011. **133**(5): p. 1294-1297.
18. Caban-Acevedo, M., et al., *Synthesis and Properties of Semiconducting Iron Pyrite (FeS2) Nanowires.* Nano Letters, 2012. **12**(4): p. 1977-1982.

19. Berry, N., et al., *Atmospheric-Pressure Chemical Vapor Deposition of Iron Pyrite Thin Films.* Advanced Energy Materials, 2012. **2**(9): p. 1124-1135.
20. Cullity, B.D., *Elements of x-ray diffraction*. 2d ed. Addison-Wesley series in metallurgy and materials. 1978, Reading, Mass.: Addison-Wesley Pub. Co. xii, 555 p.
21. Carter, D.W.a.B., *Transmission Electron Microscopy: A Textbook for Materials Science*. 2009, New York, New York: Springer.
22. Zuo, J.M. and J.C. Mabon, *Web-Based Electron Microscopy Application Software: Web-EMAPS.* Microscopy and Microanalysis, 2004. **10**(Supplement S02): p. 1000-1001.
23. Shafi, K.V.P.M., et al., *Sonochemical synthesis of functionalized amorphous iron oxide nanoparticles.* Langmuir, 2001. **17**(16): p. 5093-5097.
24. Yee, C., et al., *Self-assembled monolayers of alkanesulfonic and -phosphonic acids on amorphous iron oxide nanoparticles.* Langmuir, 1999. **15**(21): p. 7111-7115.
25. Ethayaraja, M., K. Dutta, and R. Bandyopadhyaya, *Mechanism of nanoparticle formation in self-assembled colloidal templates: Population balance model and Monte Carlo simulation.* Journal of Physical Chemistry B, 2006. **110**(33): p. 16471-16481.
26. Li, X.M., et al., *Sulfonic acid-functionalized gold nanoparticles: A colloid-bound catalyst for soft lithographic application on self-assembled monolayers.* Journal of the American Chemical Society, 2003. **125**(14): p. 4279-4284.
27. Granot, E., F. Patolsky, and I. Willner, *Electrochemical assembly of a CdS semiconductor nanoparticle monolayer on surfaces: Structural properties and photoelectrochemical applications.* Journal of Physical Chemistry B, 2004. **108**(19): p. 5875-5881.
28. Wu, J., et al., *Effects of electron concentration on the optical absorption edge of InN.* Applied Physics Letters, 2004. **84**(15): p. 2805-2807.
29. Wu, J., et al., *Unusual properties of the fundamental band gap of InN.* Applied Physics Letters, 2002. **80**(21): p. 3967-3969.
30. Zhang, Y.N., et al., *Effect of surface stoichiometry on the band gap of the pyrite FeS2(100) surface.* Physical Review B, 2012. **85**(8).
31. Sun, R.S., M.K.Y. Chan, and G. Ceder, *First-principles electronic structure and relative stability of pyrite and marcasite: Implications for photovoltaic performance.* Physical Review B, 2011. **83**(23).
32. Prince, K.C., et al., *Resonant Raman x-ray scattering at the S 2p edge of iron pyrite.* Journal of Physics-Condensed Matter, 2004. **16**(41): p. 7397-7404.
33. Eisebitt, S., et al., *Resonant inelastic soft X-ray scattering as a bandstructure probe: A primer.* Physica Status Solidi B-Basic Solid State Physics, 1999. **215**(1): p. 803-808.
34. Eich, D., et al., *Resonant inelastic soft x-ray scattering of Be chalcogenides.* Physical Review B, 2006. **73**(11).
35. Scheele, M., et al., *Synthesis and Thermoelectric Characterization of Bi(2)Te(3) Nanoparticles.* Advanced Functional Materials, 2009. **19**(21): p. 3476-3483.
36. Thomson, J.W., et al., *From Sulfur-Amine Solutions to Metal Sulfide Nanocrystals: Peering into the Oleylamine-Sulfur Black Box.* Journal of the American Chemical Society, 2011. **133**(13): p. 5036-5041.
37. Orel, Z.C., E. Matijevic, and D.V. Goia, *Precipitation and recrystallization of uniform CuCl particles formed by aggregation of nanosize precursors.* Colloid and Polymer Science, 2003. **281**(8): p. 754-759.

38. Matijevic, E., *Preparation and Properties of Uniform Size Colloids.* Chemistry of Materials, 1993. **5**(4): p. 412-426.
39. Privman, V., et al., *Mechanism of formation of monodispersed colloids by aggregation of nanosize precursors.* Journal of Colloid and Interface Science, 1999. **213**(1): p. 36-45.
40. Matijevic, E., *Monodispersed Colloids - Art and Science.* Langmuir, 1986. **2**(1): p. 12-20.
41. Lamer, V.K., *Nucleation in Phase Transitions.* Industrial and Engineering Chemistry, 1952. **44**(6): p. 1270-1277.
42. Lamer, V.K. and R.H. Dinegar, *Theory, Production and Mechanism of Formation of Monodispersed Hydrosols.* Journal of the American Chemical Society, 1950. **72**(11): p. 4847-4854.
43. Matijevic, E., *Monodispersed Metal (Hydrous) Oxides - a Fascinating Field of Colloid Science.* Accounts of Chemical Research, 1981. **14**(1): p. 22-29.
44. Matijevic, E., *Uniform Inorganic Colloid Dispersions - Achievements and Challenges.* Langmuir, 1994. **10**(1): p. 8-16.
45. Park, J., V. Privman, and E. Matijevic, *Model of formation of monodispersed colloids.* Journal of Physical Chemistry B, 2001. **105**(47): p. 11630-11635.
46. Matijevic, E., *Role of Chemical Complexing in Formation and Stability of Colloidal Dispersions.* Journal of Colloid and Interface Science, 1977. **58**(2): p. 374-389.
47. Weinhardt, L., et al., *Resonant inelastic soft x-ray scattering of CdS: A two-dimensional electronic structure map approach.* Physical Review B, 2009. **79**(16).
48. Eisebitt, S., et al., *Resonant inelastic soft X-ray scattering as a bandstructure probe: A primer.* Physica Status Solidi B-Basic Solid State Physics, 1999. **215**(1): p. 803-808.
49. Kotani, A. and S. Shin, *Resonant inelastic x-ray scattering spectra for electrons in solids.* Reviews of Modern Physics, 2001. **73**(1): p. 203-246.
50. Eich, D., et al., *Resonant inelastic soft x-ray scattering of Be chalcogenides.* Physical Review B, 2006. **73**(11).

Chapter 3:

Ab-Initio Identification of Dopants for Zinc Sulfide Intermediate Band Photovoltaic Absorbers

Based on work submitted to *Energy & Environmental Science*

J. Matthew Lucas, Danylo Zherebetskyy, Shiyou Chen, Lin-Wang Wang, A. Paul Alivisatos

Abstract

A combinatorial computational method is developed and applied to identify the most promising dopant species for formation of mid-bandgap levels in a zinc blende zinc sulfide-based intermediate band solar cell. Several requirements for functional intermediate band solar cells are discussed and evaluated using the computational approach. Group 14 dopants are all found to be the most promising dopant candidates as they all produce a single, mid-bandgap level with strong, sub-bandgap optical absorption. However, these levels are calculated to remain localized as trap states rather than be delocalized as bands. Our new methodology significantly improves upon prior studies that evaluated intermediate band solar cell materials and offers a path toward evaluation of other promising matrix semiconductors.

Background & Motivation

A variety of environmental and economic concerns have driven recent research and deployment of solar photovoltaic systems. With mono- and poly-crystalline silicon, cadmium telluride, and copper indium gallium selenide-based modules now widely deployed and rapidly falling in price, the continued challenge of reducing cost in the module has centered on increasing its efficiency. Higher-efficiency modules can accommodate higher manufacturing costs and margins, on an output-normalized basis, than lower-efficiency devices. Higher-efficiency modules realize further cost savings in land, labor, and some balance of systems components, such as racking, which scale with the number of panels required. For these reasons and observing the recent commercial failures of polymer and amorphous silicon module manufacturers, it seems that devices based on conventional 1-sun, single-junctions will be unlikely to be commercially adopted.

A convenient method for increasing efficiency is to use multi-junction devices to better harness the solar spectrum.[1] However, the epitaxial growth methods used to fabricate these devices are both expensive to manufacture and constrain the materials available due to lattice matching considerations. While approaches to multi-junction devices that do not require lattice matching, such as bonding and spectrum-splitting, are exciting and hold promise, a simpler architecture that has the same potential for efficiencies that far exceed those of conventional single-junction devices is desirable.

Intermediate band (IB) solar cells possess the spectrum-matching qualities of multi-junction architectures in a single-material form factor that should be less complex and lower cost than the multi-junction devices.[1-3] By providing an electronic state in the middle of the bandgap, IB devices permit two (or more) sub-bandgap photons to collectively produce an exciton. Prior detailed balance analysis of these devices shows they have the potential for 1 sun efficiencies over 49% and 100 sun efficiencies over 56%.[5]–[10]

Key Characteristics of an Intermediate Band Absorber

An IB absorber material must possess several qualities to be practical. First, there should be one, and only one, electronic state in the bandgap of the host semiconductor. Ideally this level will divide the bandgap into two parts approximately 1/3 and 2/3 the size of the full bandgap.[6] A full mapping of bandgaps to detailed-balance efficiency is provided in the Supporting Information. Second, the Fermi level of the system should be within this mid-gap electronic state such that it is partially, but not fully, occupied. Third, the wavefunctions of the mid-gap states must overlap to form a band rather than be localized as trap states.[11], [12] Fourth, all three optical transitions in the system–from the valence band (VB) to the mid-gap level (transition A), from the mid-gap level to the conduction band (CB) (transition B), and from the VB to the CB (transition C)—should be quantum mechanically allowed.

The second criterion, that the Fermi level be within the mid-gap state(s), is crucial because it allows Transition B to occur independently of Transition A. While an exciton could be formed by photo-filling from Transition A followed by subsequent absorption across Transition B, this sequential two-photon process is less probable unless either the excited state lifetime of a carrier in the mid-gap states is very long or very high photon fluxes are present, such as in solar devices with high optical concentration factors. The presence of a partially-occupied mid-gap level thus relaxes the required lifetime for an excited mid-gap carrier or the requirement for optical concentration. This need for partial occupation of the IB also dictates that there should only be one mid-gap level since it would be impossible to partially occupy multiple bands. If the Fermi level is positioned such that the mid-gap state is fully occupied or, conversely, completely unoccupied, compensation doping can be used to add either donors or acceptors to achieve the desired partial occupation. This approach has been used in laser recrystallized silicon to adjust the position of the Fermi level. [13]

The third criterion, that the wavefunctions of the mid-gap state must form a delocalized band rather than localized trap states, is important for improving carrier lifetime and the efficient operation of an IB device.[14] Band formation, better known as a Mott transition[15], is the distinction between isolated “trap states” and the continuum “band”. Experimentally, an IB system with a partial occupation should demonstrate metallic temperature-dependent electrical conductivity. Of course the degree of localization of the electrons in the mid-gap level is a sliding scale. Computationally, this delocalization can be estimated by comparing the reorganization energy of the system upon a change in the number of electrons, which favors localization, to the amount of dispersion in energy between two dopants that are electronically coupled, which defines delocalization. This will be addressed in more detail later.

The fourth criterion, that there be three optically-allowed transitions, likely requires hybridization in the three electronic levels to ensure there are sufficient populations of electrons that can make the required transition. One way to consider hybridization is to analyze the element- and orbital- decomposed electronic density of states [16] for the doped system and look for transitions that should be allowed by selection rules. However, since the orbitals are in different atoms this analysis is only an approximation. In zinc sulfide, Transition C, from VB-to-CB, is principally from the S(3p)-orbitals which dominate the VB to the Zn(4s)-orbitals which dominate the CB. Therefore, due to selection rules, the IB must have s- or d-orbital character to allow Transition A but p-orbital character to allow Transition B. Hybridization of the band edges and mid-gap level can permit these optical transitions. An element- and orbital-decomposed density of states for zinc blende zinc sulfide using both PBE and HSE06 functionals, as well as

bandstructure, are included in the Supporting Information. These plots agree with prior literature so we are confident our computational methods are sound.[17], [18]

Two fabrication strategies: Hyperdoping vs. Mini-band

IB solar devices have historically been fabricated by either hyperdoping of a bulk material or mini-band formation within quantum-confined structures.[2] In hyperdoping, high doses of dopants are applied to a bulk semiconductor such that the dopants, which would normally form localized deep trap states, become delocalized to form a band. This delocalization is accompanied by a reduction in electron-phonon coupling which serves to increase the carrier lifetime in that energy level.[19] In quantum well structures, the band edges of the low-bandgap region bleed into the regions with a higher bandgap to form mid-gap states. These electronic states, called mini-bands, typically suffer from weak optical absorption. Sub-bandgap photocurrent has been demonstrated in mini-band devices made of InAs/GaNAs[12] and InAs/GaAs. [13]

There has been significant experimental work in fabricating materials and even full devices using the hyperdoping technique. These include full devices using ZnTe:O [22], [23] and GaAs:N[24], [25] and materials synthesis of ZnO:Se[26], In_2S_3:V[27], TiO_2[28], [29], and Si with various chalcogenides[12], [21-25].

In this work we will focus on hyperdoping because that method has been arguably less explored. Hyperdoping also holds the potential for cost-effective manufacturing via sublimation or sputtering compared to the epitaxial quantum wells that must be fabricated to implement a mini-band device.

Prior efforts at hyperdoping can be distinguished by the dopant type: cation or anion. Cationic hyperdoping typically uses an ion implanter. The implanted material is then rapidly annealed and homogenized using a high-energy pulsed laser. However, the resulting hyperdoped material is confined to a region of at most a few hundred nanometers near the surface. [13], [19], [30]–[34] Anionic hyperdoping has been achieved in some II-VI[23], [35] and III-V[24], [25] systems by modifying the gas environment in the growth chamber during pulsed laser deposition or molecular beam epitaxy. This method has the advantage that the dopants are isovalent and no pulsed laser annealing is required. However, the resulting highly mismatched alloys are poly-crystalline. The desirable optoelectronic properties of many III-V materials are lost once they cease to be monocrystalline.

For these reasons, we have chosen to focus on II-VI materials, specifically zinc sulfide. These materials have direct bandgaps which is favorable for strong optical absorption. They can be fabricated by traditional thin film deposition techniques which is favorable for eventual experimental demonstration. Zinc sulfide has demonstrated strong photoluminescence yield even in polycrystalline form, which suggests it is more tolerant of polycrystalline grain boundaries than some III-Vs. Zinc sulfide is also stable in both n- and p-doping configurations which means it could form a homojunction. Since hyperdoped IB devices have previously been fabricated in p-i-n configurations[24] such versatility is desirable.

Key challenge is immense parameter space

The key challenge is now to identify an appropriate dopant to create the IB given the choice of zinc sulfide as the matrix semiconductor. Dopant energy levels in zinc sulfide have been previously characterized, but in the few cases of hyperdoping the dopant energy level at impurity concentrations ($< 10^{17}$ cm^{-3}) was significantly different from that at hyperdoped concentrations. This suggests some concentration

dependence to dopant energy level. While experimental verification is important, combinatorial experiments are difficult due to the need to acquire appropriately doped source materials for sputtering or sublimation targets and optimize the deposition parameters for each dopant-matrix combination. For these reasons we have chosen a combinatorial computational method using density functional theory.

There have been prior computational studies attempting to identify IB dopants in GaP[26-30], GaAs[39], [41], ZnS[32-34], ZnSe[45], ZnTe[42], [46], Si[47], In_2S_3[48], CdTe[49], TiO_2[28], and $CuGaS_2$[50]. These studies confined themselves to 3d transition metals as dopant species. However, the prior ZnS studies were implemented using local spin-density approximation (LSDA) with atomic basis sets but without ionic relaxation or the Hubbard +U correction. These studies also only applied the dopant in a cation site substitution. As a result, these studies identified chromium as the only IB dopant.[42] Two subsequent studies by the same author applied the +U correction, but only to the Cr-doped case.[43], [44] In contrast, as will be shown later herein, we find that most of the 3d transition metals produce some in-gap state. In our effort to reproduce that prior work, we found that the use of a more complete plane wave basis set (as opposed to the quite limited atomic basis used in the previous work) and, most importantly, a well-converged ionic relaxation to be the differentiating factors.

In this work we use a more thorough and rigorous approach to identifying IB dopants. This approach includes using geometry relaxation, applying the +U correction (when applicable), testing a variety of lattice doping sites and spin configurations, and using a higher level of theory than LSDA. The advantage to using zinc sulfide as the matrix semiconductor for this study is that there are a few experimental literature reports of hyperdoping in zinc sulfide. These existence proofs using Cu[51] and Mn[52] doping will allow validation of the calculations.

METHODS

64 atom supercells with one cation or anion dopant, equivalent to ~2 x 10^{20} cm^{-3}, are generated using a zinc-blende-type zinc sulfide lattice. In the case of tetrahedral or octahedral interstitial dopants, the supercell contains 65 atoms. The supercells were geometrically relaxed using the generalized gradient approximation (GGA) with Perdew–Burke–Ernzerhof (PBE)[53] functional as implemented in VASP [54]–[58] till all forces were less than 0.01 eV/Å. The Monkhorst-Pack mesh[59] of 3 x 3 x 3 k-points was used to sample the Brillouin zone for all calculations regardless of the functional employed. A cutoff energy of 425 eV was used, except in some cases where dopants required a higher potential cutoff energy be used. After repeating the geometry optimization and energy convergence for all four crystallographic sites and various spin configurations, the spin-site combination with the lowest total system energy for a given dopant element was selected for further analysis.

When applying the Hubbard correction, supercells with the dopant site previously found to be optimal were relaxed and electronically converged using PBE without spin-polarization, after which the spin-polarization and +U correction were applied. Since experimental data do not exist except or Cu- and Mn-doped ZnS systems, we performed calculations with two values of Hubbard +U correction of 1 eV and 5 eV to confirm that the preferred spin-site configuration did not change. The Hubbard correction was only applied to the dopant species, not zinc or sulfur. The partial density of states were also calculated for the +U corrected systems (with values of U = 1 eV and 5 eV) to see any effect the Hubbard correction had on energy level position.

PBE potentials are well known to produce values of the bandgap that are below experimental values. For this reason, it is desirable to compare the relative energy position of the mid-gap states in the partial density of states computed with PBE with those computed by using the hybrid Heyd–Scuseria–Ernzerhof (HSE06) functional [55] For dopant elements that showed the most promise (ie. only one mid-gap state not near the band edges), the hybrid HSE06 calculations were also run with the Hubbard correction with U = 1 eV and 5 eV in a similar manner to +U corrected systems using the PBE functional.

The frequency-dependent complex dielectric function was also calculated for the most promising dopant elements using the hybrid HSE06 functional.

RESULTS & DISCUSSION

Figure 3.1 illustrates the preferred crystallographic site (by color) and spin (by number) for various elements in their charge neutral configuration. For a given dopant element and lattice site, the preferred spin configuration is identified by having the lowest system energy. The various dopant lattice sites are compared according to their defect formation energy as described in the Supporting Information

Most elements prefer cation site substitution when doping while some main group elements prefer anion site substitution and octahedral interstitial locations. As expected, elements in the same column generally have similar spin configuration since they share the same valence electron configuration. There are a few exception however, such as molybdenum, which has nearly the same ground state energy in the s=0 and s=2 configurations. It should be noted that the spin configuration is optimized during energy convergence calculations. As a result, calculations that started with different initial values of the spin configuration may be converged to the same value. This provides increased confidence in the final spin configuration value.

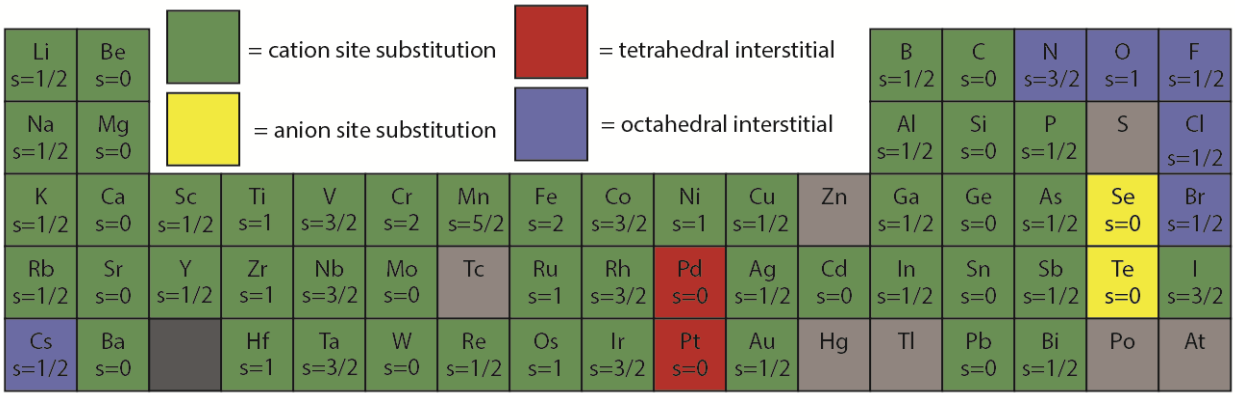

Figure 3.1 caption: Preferred crystallographic dopant site (box color) and spin (number) for various elements in 64 atom supercell of zinc-blende zinc sulfide structure. The spin is determined from HSE06 calculations.

It should be emphasized that just because a particular spin configuration and lattice site are preferred by a particular species of dopant does not mean the doping is a spontaneous process. The defect formation energy for each element in zinc sulfide is given in Supporting Information. These defect formation energies are for the preferred dopant configuration and are thus the lowest values for their respective elements. The formulas used to calculate the defect formation energies are also given in the Supporting Information. All the defect formation energies are positive, which indicates the doping is not spontaneous.

Figure 3.2 identifies changes in the preferred spin configuration after applying the Hubbard +U correction. The +U correction is made to elements with d-orbital character in their pseudopotentials and accounts for core potential that may be incorrectly represented by the pseudopotentials. In most applications the value of U is fit against a known material parameter that can be calculated and the optimized U-value is then used to calculate the unknown property. Since the U-value for most dopant elements in zinc sulfide has not been calibrated, we have chosen two values of U (1 and 5 eV) that are generally within the typical range from 1 to 9 eV.

The preferred spin configuration after Hubbard correction is determined by calculating the system energy for various spin configurations in the preferred dopant site determined in Figure 3.1 and choosing the spin configuration with the lowest system energy. Only a few dopant species (Ta, Mo, Re) show any change in preferred spin configuration and those changes are due to very small differences in total system energy. The Re-doped system only changed from s=1/2 to s=5/2 when U=5 eV. The difference in the Ta-doped system energy between s= ½ and s=3/2 when U=1 eV is only 0.01 eV. The difference in the Mo-doped system's energy between s=0 and s=2 when U=5 eV is also only 0.01 eV. While the Hubbard correction does not change the optimal electron spin configuration for many elements, it will be clear later that the correction can have a significant impact on the mid-gap eigen-energies.

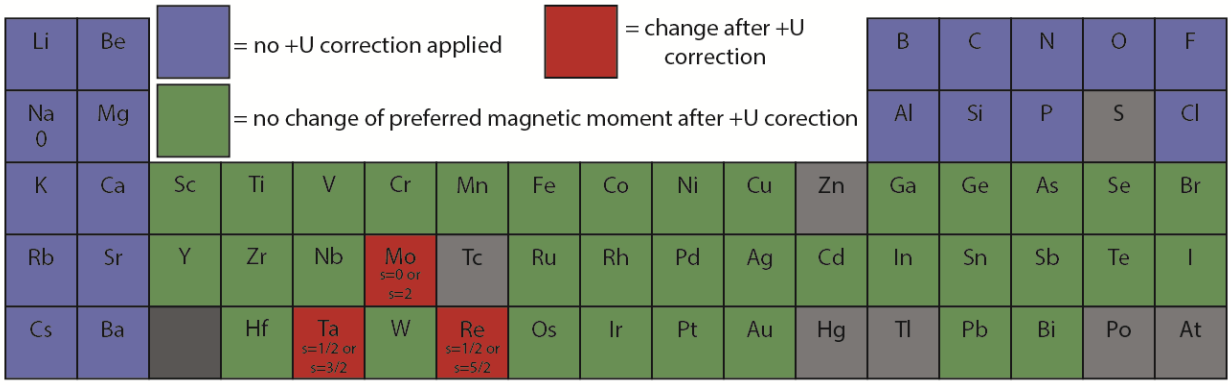

Figure 3.2 caption: Preferred spin (number) and its change after GGA+U correction (box color) with U value of either 1eV or 5eV for various elements in supercells of zinc sulfide. Most elements did not change their preferred spin configuration due to the Hubbard correction.

Figure 3.3 illustrates the polarized electronic density of states for a variety of dopant species that exhibit a range of behaviors. The 'spin down' is plotted to the left and the 'spin up' component is plotted to the right. To guide the eye, the valence band is colored green, the conduction band is colored gray, and in-gap states are colored blue. The total density of states is plotted in dark blue while the contribution from the dopant is plotted in red. The energy axis is normalized to the Fermi energy. Sr-doped zinc sulfide is representative of systems that do not have any in-gap states. These systems are therefore expected to exhibit a single band-edge-to-band-edge transition similar to an undoped semiconductor. The red density shows that strontium contributes some density to the conduction band. F-doped zinc sulfide is representative of systems that have state(s) near one or both of the band edges. In real semiconductors with thermal broadening, these near-edge dopant levels would merge with the nearby band and the system would effectively have smaller bandgaps than their undoped counterparts. The red density from the fluorine is evident in the state near the valence band maximum as well as within the valence band itself. Fe-doped zinc sulfide is representative of systems that have more than one in-gap state where at

least one of the states is not near a band edge. These systems would be expected to have more than one transition, but as explained earlier, having too many in-gap states is not advantageous. In the case of iron doping, the red density is present in both the mid-gap states as well as the conduction band. One of the in-gap states is below the zero energy and is thus fully-occupied while the other in-gap state is at a positive energy and is therefore unoccupied. Collectively, these three systems represent undesirable outcomes for doping if the goal is to generate intermediate band absorbers.

This representation of the density of states allows quick comparison of different dopant species. Since the PBE functional is well known to underestimate the bandgap of semiconductors (2.02 eV for undoped ZnS), we employ the HSE06 functional (3.24 eV for undoped ZnS) to more closely estimate what the actual transition energies would be an experimental system.

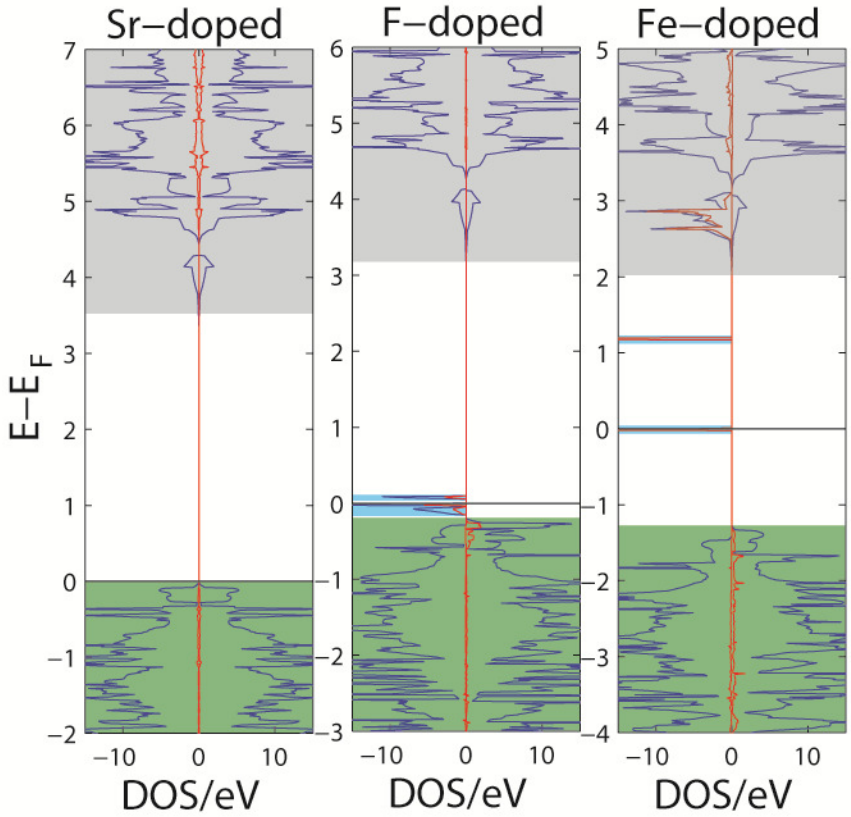

Figure 3.3 caption: Polarized density of states for three different dopants representing a variety of different outcomes. Valence band is colored green, conduction band is colored grey, and in-gap states are colored blue. Total density is plotted in dark blue and the contribution from the dopant is plotted in red.

This group of dopant species is illustrated to show the variety of possible outcomes from doping and how they are categorized based on where the dopant states lie in the bandgap. Fluorine and chlorine produced no in-gap states. Since the goal is to identify IB dopants, these elements are not of interest for the present application. Bromine only produces states close to the band edge. States so close to the band edge are likely to merge with the band edge after thermal broadening and so would not be a discrete level. Instead, the likely result would be a shrinking of the bulk bandgap. Iodine doping generated multiple in-gap states. These three outcomes represent three undesirable outcomes from hyperdoping. The fourth and desired possibility is for a single state to exist near the mid-gap.

1st and 2nd criterion: Only one mid-gap state that contains the Fermi level

Figure 3.4 graphically represents the dopant level position within the bandgap for all elements. Many dopants produce no in-gap states (colored red), multiple in-gap states (colored blue), or states very near to a band edge (color yellow). For the purposes of hyperdoped IB absorbers those dopants that produce only 1 mid-gap state (colored green) are most interesting.

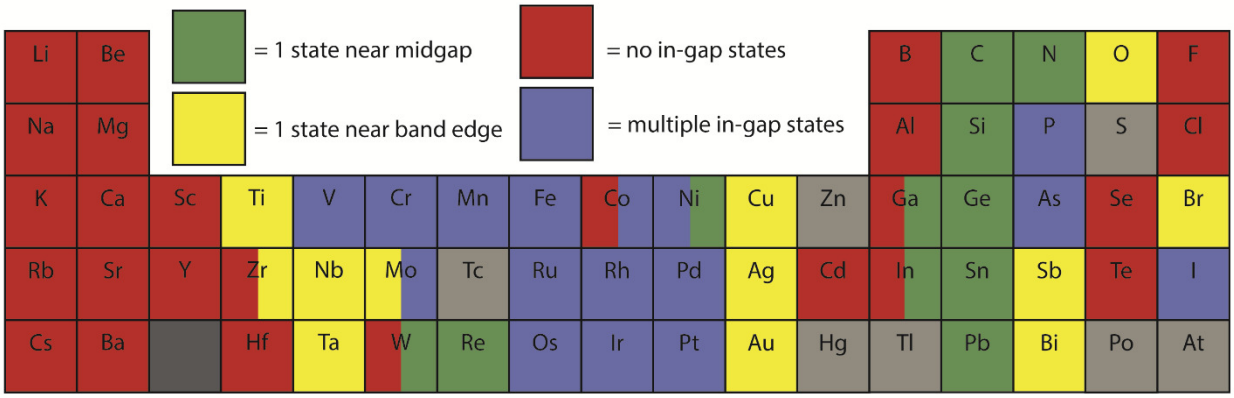

Figure 3.4 caption: Graphical representation of position of mid-bandgap states within bandgap due to hyperdoping of a zinc blende zinc sulfide matrix with various elements in their preferred crystallographic site and spin configuration. The positions of the mid-gap states are derived from PBE, PBE+U (where applicable), HSE06, and HSE06+U (where applicable) calculations. A single mid-bandgap state far from either band edge (colored green) is preferred for a 3-transition solar absorber material. Multiple colors for an element means dopant level positions were influenced by the level of theory used.

The most obvious trend from Figure 3.4 is that all the Group 14 elements produce appropriate doping energy levels within the zinc sulfide bandgap. In Figure 3.5, the DOS are plotted for Group 14-doped ZnS. The Hubbard correction is not applicable for carbon and silicon doping while heavier elements (Ge, Sn, Pb) can use the Hubbard correction. Since the mid-gap level in the +U calculations qualitatively agrees with the level predicted by the PBE or HSE06 calculation without +U, only the corrected densities are included in Figure 3.5.

Some of the dopant elements in Figure 3.4 have two colors which means different levels of theory results in different dopant energy level positions. Since these structures are less certain of producing the desired energy level alignment they are not considered beyond this section. In the case of zirconium, all GGA and GGA+U calculations found no in-gap states, but HSE06 and HSE06+U (where U = 1 eV) found a state near the CB. In the case of molybdenum, there are both s=0 and s=2 configurations. The s=0 configurations in GGA and GGA+U produce one state near the CB, but HSE06 produces a single mid-gap level. The spin 4 configuration produces multiple in-gap states. In the case of tungsten, GGA and GGA+U produce no in-gap states but HSE06 and HSE06+U produce a single mid-gap state. In the case of cobalt, GGA and GGA+U produce multiple in-gap states while HSE06 produces no in-gap states. In the case of nickel, GGA and GGA+U (where U = 5 eV) produce a single mid-gap state, but HSE06 and HSE06+U produce multiple in-gap states. In the cases of both indium and gallium, GGA and GGA+U predict no in-gap states but HSE06 and HSE06+U predict a single mid-gap state. Rhenium is predicted by GGA and GGA+U to have a single mid-gap state, but we were not able to converge the HSE06 calculation and so will disregard this dopant.

One advantage to using zinc sulfide as the matrix semiconductor for this study is that there are a few experimental literature reports of hyperdoping in zinc sulfide. Cu-doped zinc sulfide was found[51] to be a degenerate p-type dopant while Mn-doped zinc sulfide was found [52] to produce a much lower energy luminescence, consistent with a 3- or 4-level system. Both of these experimental observations are consistent with our theoretical results.

Figure 3.5 plots the polarized density of states for Group 14-doped zinc sulfide along with undoped zinc sulfide for comparison. The calculations are all spin polarized, but all the Group 14-doped systems prefer s=0 so the two spin components are identical. If the DFT bandgaps are scaled to the experimental bandgaps, these systems are predicted to have detailed-balance efficiencies of 27% for C-doped, 13% for Si-doped, 33% for Ge-doped, 46% for Sn-doped, and 21% for Pb-doped zinc sulfide under maximum concentration. Since the ZnS matrix has a bandgap that is too wide to be optimal, these theoretical efficiencies are disappointing but not surprising.

The fully-occupied mid-gap states would appear to break the second requirement of IB materials—that the mid-gap states be partially, not fully, occupied. While the rule is broken here, we propose that initial experimental systems could be gated to create a partial occupation of the IB. As discussed previously, full devices would require compensation doping. Recent work by Buonassisi and co-workers[13] using pulsed laser recrystallization of silcon doped with sulfur and compensated with boron suggests such high-concentration compensation doping is feasible.

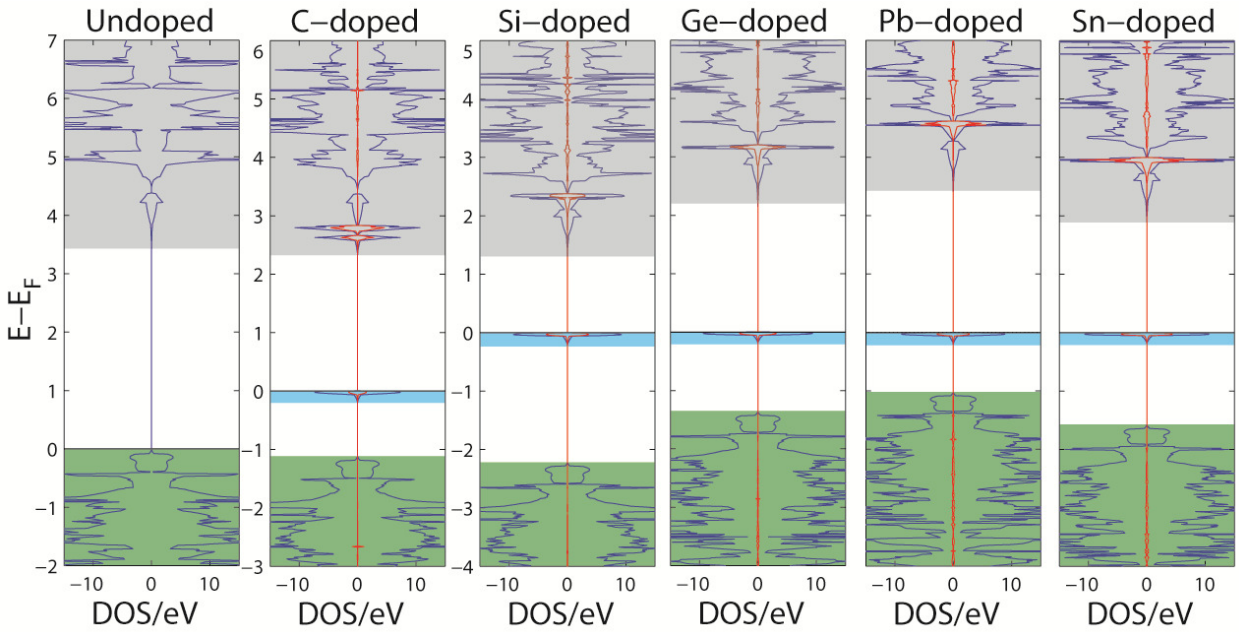

Figure 3.5 caption: Polarized density of states for Group 14-doped zinc blende ZnS. The valence bands are colored green, the conduction bands are colored grey, and the mid-gap levels are colored blue. Total density of states is plotted in blue while the contribution from the dopant is plotted in red. A horizontal, black line at the zero energy denotes the Fermi level.

3rd Criterion: Delocalization of Mid-gap States

The third criterion for an effective mid-gap level is that the states should delocalize from discrete, localized states into a delocalized band. Computationally, delocalization can be qualitatively described by comparing the magnitudes of the reorganization energy to the dopant coupling energy. The reorganization energy represents the decrease in system energy due to relaxation of the ionic positions within the lattice following the loss of an electron from the supercell. Systems that are heavily distorted by passing of charge will have high reorganization energies. The coupling energy represents the degree of overlap of dopant atoms, which are assumed to be homogeneously distributed throughout the material. Whichever energy is higher is thus expected to dominate the process. High doping densities will increase the coupling energy. If reorganization energy is greater than the coupling energy, the electron will prefer to remain on the dopant atom and be localized. If the coupling of the dopants is stronger, then the electrons should prefer to delocalize into a band-like state.

To calculate the reorganization energy we must know the preferred charge state of the silicon dopant in the system. The defect formation energy of various charge states of all Group 14 dopants is examined in the Supporting Information and summarized in Figure 3.6 below.

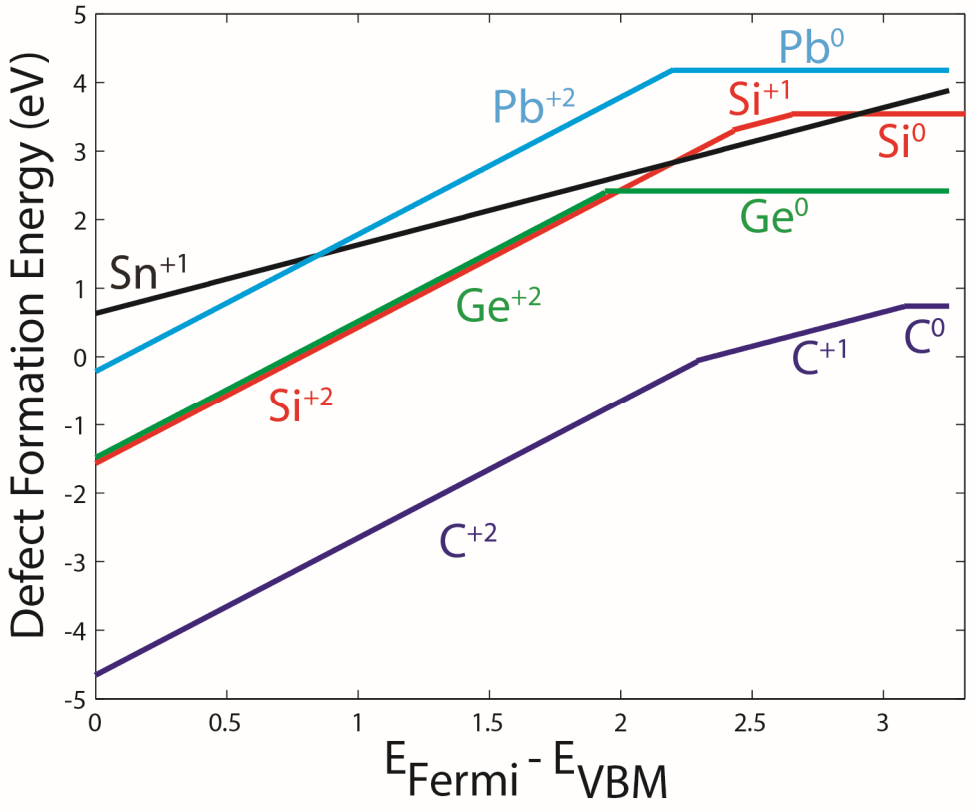

Figure 3.6 caption: Defect formation energy for various charge states of Group 14-doped zinc sulfide calculated using the PBE functional. Different values of the Fermi level within the bandgap yield different preferred charge states. Dopants with more negative defect formation energies are expected to be more preferred in the lattice.

Now that the charge states to be used in the reorganization energy calculation are known, we begin with a 64 atom supercell that has undergone ionic relaxation with the neutral (ie. uncharged) number of electrons. The energy of the relaxed supercell is compared to the energy of the supercell before relaxation. The energy difference is the reorganization energy for the neutral case, Si^0. Next, an electron is removed and the system energy is calculated without ionic relaxation, then the supercell with one missing electron is relaxed and the energy calculated. This energy difference is the reorganization energy for Si^{+1}. This process is repeated for higher-charge systems such that the reorganization energy represents the reorganization for the loss (or gain) of a single electron. The neutral system does not have a reorganization energy since it is the reference for other charged systems.

To calculate the coupling energy between dopants we find the energy of a 64 atom supercell containing a single dopant. The maximum dispersion will be between the k-point at the center of the Brillion zone, gamma (0,0,0), and the (0,0,1/2) point at the edge of the Brillion zone, which is the X point in the zinc blende lattice. Alternatively, the coupling energy can be thought of as the maximum dispersion of the intermediate level. In Si-doped zinc sulfide (see Supporting Information), the intermediate level is nearest to the VBM at the gamma point and nearest to the CBM at the X point. Therefore the maximum dispersion is found by taking the difference in energy between these two k-points. An alternative method would be to form a 128-atom, 2-dopant supercell. In this expanded supercell there are two eigen-energies at the gamma point, which have the same energy difference as between the gamma and X points in the 64 atom supercell. The coupling energy is only one-quarter that of the energy dispersion of the intermediate state. The factor of four comes from the tight binding model where the energy dispersion is proportional to twice the coupling energy multiplied by the sinusoidal plane wave functions, which have a range of values equal to two.

Charge state of dopant	**Reorganization energy (meV)**	**Coupling energy (meV)**
C^0	----	69
C^{+1}	546	76
C^{+2}	332	69
Si^0	----	90
Si^{+1}	432	87
Si^{+2}	453	105
Ge^0	----	64
Ge^{+2}	560	80
Pb^0	----	66
Pb^{+2}	279	62
Sn^{+1}	360	64

Table 1 caption: Reorganization energy and coupling energy for 64 atom supercell of zinc sulfide with one dopant. Calculations used the PBE functional. In all cases, the reorganization energy is greater than the coupling energy, which indicates that the intermediate state will remain localized.

The results of reorganization energy and coupling energy calculations are presented in Table 1. For all charge states of all the dopants, the reorganization energy is greater than the coupling energy. This indicates that the electron is likely to be localized on the silicon at this doping concentration. Practically, this could be overcome by increasing the doping density. This finding also suggests that stiffer, more covalent semiconductors, which would have smaller reorganization energies, would be better matrix materials than comparatively ionic materials like zinc sulfide.

4th Criterion: Optically-Allowed Transitions

The fourth criterion for an IB material requires that there be three-optically allowed transitions. The Si-doped zinc sulfide system studied in Figure 3.7 has a fully occupied IB. As a result there are no VB to IB transitions. However, the other transitions—from IB-to-CB minimum, IB-to-higher states within the CB, and VB maximum-to-CB—can be studied.

To know how strong an optical transition is, the oscillator strength must be calculated. We calculate the complex dielectric function of the doped systems, which is subsequently transformed to the complex refractive index, and then to absorptivity (units of cm^{-1}). The formulas for the transformations are given in Supporting Information and absorptivity is plotted in Figure 3.7.

By minimizing the broadening in the VASP calculations (by setting CSHIFT and SIGMA to very small values) discrete optical transitions can be identified. While Figure 3.7 is not representative of an experimental absorption spectrum, which would include broadening and optical transitions at all points in k-space, this spectrum, with little broadening and a limited number of k-points, allows individual transitions to be analyzed. The inset of Figure 3.7, which includes broadening, is more indicative of what an experimental spectrum would look like. The absorption is peaked rather than monotonically increasing like most experimental spectra because there are a small and finite number of high-energy states in the VASP calculations. Therefore, the transitions from the IB and CBM deep into the conduction band are missing, leading to the peak in the spectrum.

These transitions are lettered in Figure 3.7 and assigned to a particular direct transition at one or more of the six irreducible k-points in the supercell by matching the optical transition energy to the eigen-energies at the various k-points. Indirect transitions were not considered because they are generally much weaker than direct transitions and thus are not expected to dominate the features in Figure 3.7. The VBM-to-CBM optical transitions for undoped zinc sulfide is also plotted for comparison. Since the IB is fully occupied there are no VB-to-IB transitions owing to the lack of empty IB states. Only IB-to-CB transitions are permitted.

Interestingly, the location of the optical transition in k-space changes after Si-doping. In undoped zinc sulfide, the primary optical transition is a direct transition at the gamma point, which is k-point #1 in Figure 3.7. However, after Si-doping the IB-to-CB-minimum transition at the gamma point is not allowed and therefore is not present in Figure 3.7. Nevertheless we find there are many allowed sub-bandgap optical transitions. The VB-to-CB transitions have a strength roughly consistent with experimental data, [17] while there are several sub-bandgap transitions with absorptivity that's only a factor of about 3 less than the band edge. Given the comparatively smaller number of states in the mid-gap level than in the VB or CB, such strong absorption demonstrates that the transitions from the IB are strongly allowed.

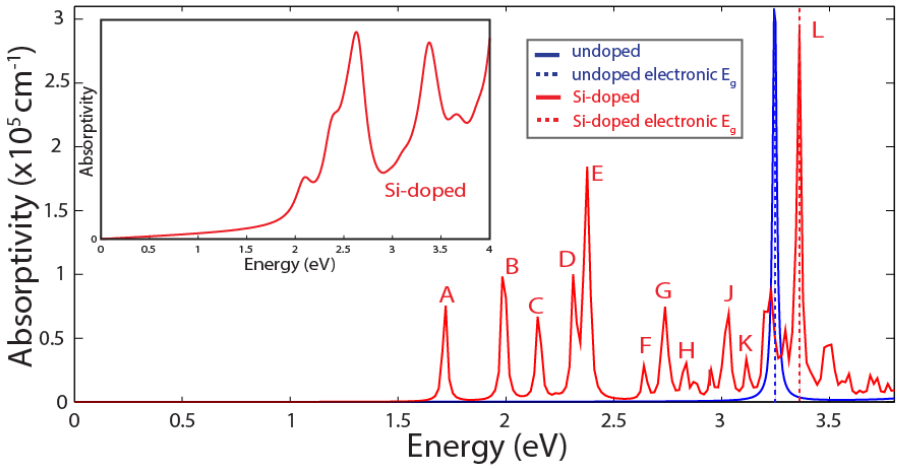

Feature	Energy (eV)	K-point(s)	Transition
A	1.72	2	IB --> CBM
B	1.98	3,4	IB --> CBM
C	2.15	2 5,6	IB --> CBM+1 IB --> CBM
D	2.31	3,4	IB --> CBM+1
E	2.38	3,4,5,6	IB --> CBM+2
F	2.64	2,5,6	IB --> CBM+3
G	2.74	3,4	IB --> CBM+2
H	2.84	1 2 3	IB --> CBM+3 IB --> CBM+5 IB --> CBM+6
I	2.95	2	IB --> CBM+6
J	3.03	3 4 5,6	IB --> CBM+9 IB --> CBM+8 IB --> CBM+7
K	3.12	3 4 5,6	IB --> CBM+10 IB --> CBM+9 IB --> CBM+8
L	3.35	1	VBM --> CBM

Figure 3.7 caption: Optical absorptivity vs. energy for undoped and Si-doped zinc sulfide. Optical features are lettered and assigned to particular transitions by comparing the eigen-energies at the six irreducible k-points in the doped system. The primary transition for the undoped system at the gamma point (k-point #1) is not allowed in the doped system, so the lowest energy transition occurs at k-point #2 at a slightly higher energy. Inset: Optical absorption with smearing that approximates what an experimental spectrum might look like. There is significant sub-bandgap absorptivity. Table: An optical feature may be present at more than one k-point. The six k-points used, in order, are (0,0,0), (1/3,0,0), (1/3,1/3,0), (-1/3,1/3,0), (1/3,1/3,1/3), and (-1/3,1/3,1/3).

Having shown that the optical transitions are indeed allowed, hybridization can roughly explain the calculations. Recall that zinc sulfide's VB is dominated by S(3p)-character and the CB is dominated by Zn(4s)-character (see Supporting Information for element- and orbital-decomposed density of states). Roughly following selection rules, this requires the IB to have s- or d- character to have allowed transitions with the VB and p-character for transitions with the CB. The IB in Si-doped zinc sulfide was found to have a density dominated by sulfur p-orbital (47%) and silicon s-orbital (37%) character, along with sulfur s-orbital (6%) and s-, p-, and d-orbital character from zinc (10% total). This well-hybridized IB is thus expected to have allowed optical transitions with both the VB and CB.

Summary

In summary, a combinatorial computational study has been completed to assess the creation of mid-gap energy levels in a zinc-blende zinc sulfide lattice for the purpose of creating intermediate band solar absorbers. This rigorous study included geometric relaxation, applying the +U correction (when applicable), testing a variety of lattice doping sites and spin configurations, and using several levels of theory (GGA and HSE06). The resulting energy levels are calculated and the group 14 elements (C, Si, Ge, Sn, Pb) are found to have favorable energy level alignment across all levels of theory. Optical properties and dopant coupling calculations on a Si-doped system suggest strong sub-bandgap absorption. Unfortunately the silicon dopants are not sufficiently coupled to form delocalized bands. The intermediate level is also predicted to be fully occupied, so it would have to be de-populated to permit a VB-to-IB transition.

Future work will explore concentration dependence of the dopant species, additional crystallographic defects that might be present in hyperdoped crystals, further explore the optical and electrical properties

of promising dopants, and apply this combinatorial methodology to host semiconductors with bandgaps more appropriately matched to the solar spectrum.

References

[1] A. Polman and H. a Atwater, "Photonic design principles for ultrahigh-efficiency photovoltaics.," *Nat. Mater.*, vol. 11, no. 3, pp. 174–7, Mar. 2012.

[2] A. Luque and A. Marti, "Towards the intermediate band," *Nat. Commun.*, vol. 2, no. March, p. 166, Jan. 2011.

[3] A. Luque and A. Martí, "The intermediate band solar cell: progress toward the realization of an attractive concept.," *Adv. Mater.*, vol. 22, no. 2, pp. 160–74, Jan. 2010.

[4] A. Luque and A. Marti, "A metallic intermediate band high efficiency solar cell," *Prog. Photovoltaics Res. Appl.*, vol. 9, no. 2, pp. 73–86, Mar. 2001.

[5] L. Cuadra, A. Martí, A. Luque, and S. Member, "Influence of the Overlap Between the Absorption Coefficients on the Efficiency of the Intermediate Band Solar Cell," *IEEE Trans. Electron Devices*, vol. 51, no. 6, pp. 1002–1007, 2004.

[6] S. P. Bremner, M. Y. Levy, and C. B. Honsberg, "Limiting efficiency of an intermediate band solar cell under a terrestrial spectrum," *Appl. Phys. Lett.*, vol. 92, no. 17, p. 171110, 2008.

[7] A. Lin and J. Phillips, "Decoupling spectral overlap of intermediate band solar cells using low-high state filling," *Photovolt. Spec. Conf. (PVSC), …*, pp. 13–15, 2012.

[8] A. Luque and A. Martı, "Increasing the Efficiency of Ideal Solar Cells by Photon Induced Transitions at Intermediate Levels," *Phys. Rev. Lett.*, vol. 78, 1997.

[9] M. Y. Levy and C. Honsberg, "Intraband absorption in solar cells with an intermediate band," *J. Appl. Phys.*, vol. 104, no. 11, p. 113103, 2008.

[10] K. Yoshida, Y. Okada, and N. Sano, "Device simulation of intermediate band solar cells: Effects of doping and concentration," *J. Appl. Phys.*, vol. 112, no. 8, p. 084510, 2012.

[11] a. Martí, E. Antolín, P. García-Linares, I. Ramiro, I. Artacho, E. López, E. Hernández, M. J. Mendes, A. Mellor, I. Tobías, D. Fuertes Marrón, C. Tablero, a. B. Cristóbal, C. G. Bailey, M. Gonzalez, M. Yakes, M. P. Lumb, R. Walters, and A. Luque, "Six not so easy pieces in intermediate band solar cell research," *Proc. SPIE*, vol. 8620, no. photon 1, p. 86200J–86200J–11, Mar. 2013.

[12] A. Luque, A. Martí, and C. Stanley, "Understanding intermediate-band solar cells," *Nat. Photonics*, vol. 6, no. 3, pp. 146–152, Feb. 2012.

[13] C. B. Simmons, A. J. Akey, J. P. Mailoa, D. Recht, M. J. Aziz, and T. Buonassisi, "Enhancing the Infrared Photoresponse of Silicon by Controlling the Fermi Level Location within an Impurity Band," *Adv. Funct. Mater.*, p. n/a–n/a, Feb. 2014.

[14] A. Luque, A. Martí, E. Antolín, and C. Tablero, “Intermediate bands versus levels in non-radiative recombination,” *Phys. B Condens. Matter*, vol. 382, no. 1–2, pp. 320–327, Jun. 2006.

[15] N. F. Mott, “Metal-Insultaor Transition,” *Rev. Mod. Phys.*, vol. 40, no. 4, 1968.

[16] D. Zherebetskyy and L.-W. Wang, “In-Gap States in Electronic Structure of Nonpolar Surfaces of Insulating Metal Oxides,” *Adv. Mater. Interfaces*, vol. 1, no. 8, p. n/a–n/a, Nov. 2014.

[17] J. Lucas, C. Tuan, S. Lounis, and D. Britt, “Ligand-Controlled Colloidal Synthesis and Electronic Structure Characterization of Cubic Iron Pyrite (FeS2) Nanocrystals,” *Chem. Mater.*, pp. 2–7, 2013.

[18] S. Z. Karazhanov, P. Ravindran, a. Kjekshus, H. Fjellvåg, and B. G. Svensson, “Electronic structure and optical properties of ZnX (X=O, S, Se, Te): A density functional study,” *Phys. Rev. B*, vol. 75, no. 15, p. 155104, Apr. 2007.

[19] E. Antolín, a. Martí, J. Olea, D. Pastor, G. González-Díaz, I. Mártil, and a. Luque, “Lifetime recovery in ultrahighly titanium-doped silicon for the implementation of an intermediate band material,” *Appl. Phys. Lett.*, vol. 94, no. 4, p. 042115, 2009.

[20] Y. Okada, T. Morioka, K. Yoshida, R. Oshima, Y. Shoji, T. Inoue, and T. Kita, “Increase in photocurrent by optical transitions via intermediate quantum states in direct-doped InAs/GaNAs strain-compensated quantum dot solar cell,” *J. Appl. Phys.*, vol. 109, no. 2, p. 024301, 2011.

[21] A. Martí, E. Antolín, C. Stanley, C. Farmer, N. López, P. Díaz, E. Cánovas, P. Linares, and A. Luque, “Production of Photocurrent due to Intermediate-to-Conduction-Band Transitions: A Demonstration of a Key Operating Principle of the Intermediate-Band Solar Cell,” *Phys. Rev. Lett.*, vol. 97, no. 24, pp. 1–4, Dec. 2006.

[22] W. Wang, A. S. Lin, and J. D. Phillips, “Intermediate-band photovoltaic solar cell based on ZnTe:O,” *Appl. Phys. Lett.*, vol. 95, no. 1, p. 011103, 2009.

[23] T. Tanaka, M. Miyabara, Y. Nagao, K. Saito, Q. Guo, M. Nishio, K. M. Yu, and W. Walukiewicz, “Photocurrent induced by two-photon excitation in ZnTeO intermediate band solar cells,” *Appl. Phys. Lett.*, vol. 102, no. 5, p. 052111, 2013.

[24] N. López, L. Reichertz, K. Yu, K. Campman, and W. Walukiewicz, “Engineering the Electronic Band Structure for Multiband Solar Cells,” *Phys. Rev. Lett.*, vol. 106, no. 2, p. 028701, Jan. 2011.

[25] N. Ahsan, N. Miyashita, M. Monirul Islam, K. Man Yu, W. Walukiewicz, and Y. Okada, “Two-photon excitation in an intermediate band solar cell structure,” *Appl. Phys. Lett.*, vol. 100, no. 17, p. 172111, 2012.

[26] M. a. Mayer, D. T. Speaks, K. M. Yu, S. S. Mao, E. E. Haller, and W. Walukiewicz, “Band structure engineering of ZnO[sub 1−x]Se[sub x] alloys,” *Appl. Phys. Lett.*, vol. 97, no. 2, p. 022104, 2010.

[27] R. Lucena, I. Aguilera, P. Palacios, P. Wahnón, and J. C. Conesa, “Synthesis and Spectral Properties of Nanocrystalline V-Substituted In2S3 , a Novel Material for More Efficient Use of Solar Radiation,” *Chem. Mater.*, vol. 20, no. 16, pp. 5125–5127, Aug. 2008.

[28] J. Wang, H. Sun, J. Huang, Q. Li, and J. Yang, “Band Structure Tuning of TiO2 for Enhanced Photoelectrochemical Water Splitting,” *J. Phys. Chem. C*, 2014.

[29] Z. Tong, T. Peng, W. Sun, W. Liu, S. Guo, and X. Zhao, “Introducing an Intermediate Band into Dye-Sensitized Solar Cells by W 6 + Doping into TiO2 Nanocrystalline Photoanodes,” *J. Phys. Chem. C*, pp. 16892–16895, 2014.

[30] J. Olea, M. Toledano-Luque, D. Pastor, E. San-Andrés, I. Mártil, and G. González-Díaz, “High quality Ti-implanted Si layers above the Mott limit,” *J. Appl. Phys.*, vol. 107, no. 10, p. 103524, 2010.

[31] M. Winkler, D. Recht, M.-J. Sher, A. Said, E. Mazur, and M. Aziz, “Insulator-to-Metal Transition in Sulfur-Doped Silicon,” *Phys. Rev. Lett.*, vol. 106, no. 17, p. 178701, Apr. 2011.

[32] E. Garc, R. Garc, J. Olea, and D. Pastor, “Sub-bandgap spectral photo-response analysis of Ti supersaturated Si,” *Appl. Phys. Lett.*, vol. 192101, pp. 1–5, 2012.

[33] I. Umezu, J. M. Warrender, S. Charnvanichborikarn, A. Kohno, J. S. Williams, M. Tabbal, D. G. Papazoglou, X.-C. Zhang, and M. J. Aziz, “Emergence of very broad infrared absorption band by hyperdoping of silicon with chalcogens,” *J. Appl. Phys.*, vol. 113, no. 21, p. 213501, 2013.

[34] E. Ertekin, M. Winkler, D. Recht, A. Said, M. Aziz, T. Buonassisi, and J. Grossman, “Insulator-to-Metal Transition in Selenium-Hyperdoped Silicon: Observation and Origin,” *Phys. Rev. Lett.*, vol. 108, no. 2, p. 026401, Jan. 2012.

[35] T. Tanaka, S. Kusaba, T. Mochinaga, K. Saito, Q. Guo, M. Nishio, K. M. Yu, and W. Walukiewicz, “Molecular beam epitaxial growth and optical properties of highly mismatched ZnTe1−xOx alloys,” *Appl. Phys. Lett.*, vol. 100, no. 1, p. 011905, 2012.

[36] C. Tablero, “Survey of intermediate band material candidates,” *Solid State Commun.*, vol. 133, no. 2, pp. 97–101, Jan. 2005.

[37] P. Palacios, J. Fernández, K. Sánchez, J. Conesa, and P. Wahnón, “First-principles investigation of isolated band formation in half-metallic TixGa1−xP(x=0.3125–0.25),” *Phys. Rev. B*, vol. 73, no. 8, p. 085206, Feb. 2006.

[38] C. Tablero, “Optoelectronic properties analysis of Ti-substituted GaP.,” *J. Chem. Phys.*, vol. 123, no. 18, p. 184703, Nov. 2005.

[39] P. Wahnón and C. Tablero, “Ab initio electronic structure calculations for metallic intermediate band formation in photovoltaic materials,” *Phys. Rev. B*, vol. 65, no. 16, p. 165115, Apr. 2002.

[40] C. Tablero, “Analysis of the electronic properties of intermediate band materials as a function of impurity concentration,” *Phys. Rev. B*, vol. 72, no. 3, p. 035213, Jul. 2005.

[41] C. Tablero, “Ab-initio spin polarized electronic structure calculations for Ti x Ga n As m photovoltaic materials,” *J. Mater. Sci.*, vol. 0, pp. 1383–1386, 2005.

[42] C. Tablero, “Survey of intermediate band materials based on ZnS and ZnTe semiconductors,” *Sol. Energy Mater. Sol. Cells*, vol. 90, no. 5, pp. 588–596, Mar. 2006.

[43] C. Tablero, “Electronic and magnetic properties of ZnS doped with Cr,” *Phys. Rev. B*, vol. 74, no. 19, p. 195203, Nov. 2006.

[44] C. Tablero, “Correlation effects and electronic properties of Cr-substituted SZn with an intermediate band,” *J. Chem. Phys.*, vol. 123, no. 11, p. 114709, 2005.

[45] C. Tablero, “Correlation effects for highly Cr doped ZnSe,” *J. Phys. Condens. Matter*, vol. 19, no. 46, p. 466209, Nov. 2007.

[46] J. Kim, W. Yin, J. Kang, Y. Yan, S. Wei, and M. M. Al-jassim, “Creating intermediate bands in ZnTe via co-alloying approach,” *Appl. Phys. …*, vol. 7, pp. 121201–121204, 2014.

[47] K. Sánchez, I. Aguilera, P. Palacios, and P. Wahnón, “Assessment through first-principles calculations of an intermediate-band photovoltaic material based on Ti-implanted silicon: Interstitial versus substitutional origin,” *Phys. Rev. B*, vol. 79, no. 16, p. 165203, Apr. 2009.

[48] P. Palacios, I. Aguilera, K. Sánchez, J. Conesa, and P. Wahnón, “Transition-Metal-Substituted Indium Thiospinels as Novel Intermediate-Band Materials: Prediction and Understanding of Their Electronic Properties,” *Phys. Rev. Lett.*, vol. 101, no. 4, p. 046403, Jul. 2008.

[49] Y. Seminovski, P. Palacios, and P. Wahnón, “Obtaining an intermediate band photovoltaic material through the Bi insertion in CdTe,” *Sol. Energy Mater. Sol. Cells*, vol. 114, pp. 99–103, Jul. 2013.

[50] P. Palacios, K. Sánchez, J. C. Conesa, J. J. Fernández, and P. Wahnón, “Theoretical modelling of intermediate band solar cell materials based on metal-doped chalcopyrite compounds,” *Thin Solid Films*, vol. 515, no. 15, pp. 6280–6284, May 2007.

[51] A. M. Diamond, L. Corbellini, K. R. Balasubramaniam, S. Chen, S. Wang, T. S. Matthews, L.-W. Wang, R. Ramesh, and J. W. Ager, “Copper-alloyed ZnS as a p-type transparent conducting material,” *Phys. Status Solidi*, vol. 209, no. 11, pp. 2101–2107, Nov. 2012.

[52] K. I. H. Yoon, J. K. Ahn, and J. Y. Cho, “Optical characteristics of undoped and Mn doped ZnS films,” *J. Mataerials Sci.*, vol. 36, pp. 1373–1376, 2001.

[53] J. Perdew, K. Burke, and M. Ernzerhof, “Generalized Gradient Approximation Made Simple.,” *Phys. Rev. Lett.*, vol. 77, no. 18, pp. 3865–3868, Oct. 1996.

[54] L. Hedin, “New Method for Calculating the One-Particle Green’s Function with Application to the Electron-Gas Problem,” *Phys. Rev.*, vol. 139, pp. A796–A823, 1965.

[55] J. Heyd, G. E. Scuseria, and M. Ernzerhof, “Hybrid functionals based on a screened Coulomb potential,” *J. Chem. Phys.*, vol. 118, no. 18, p. 8207, 2003.

[56] G. Kresse and D. Joubert, “From ultrasoft pseudopotentials to the projector augmented-wave method,” *Phys. Rev. B*, vol. 59, no. 3, pp. 11–19, 1999.

[57] G. Kresse and J. Hafner, “Ab Initio molecular dynamics for liquid metals,” *Phys. Rev. B*, vol. 47, no. 1, pp. 558–561, 1993.

[58] M. Shishkin and G. Kresse, “Implementation and performance of the frequency-dependent GW method within the PAW framework,” *Phys. Rev. B*, vol. 74, no. 3, p. 035101, Jul. 2006.

[59] H. J. Monkhorst and J. D. Pack, “Special points for Brillouin-zone integrations,” *Phys. Rev. B*, vol. 13, no. 12, pp. 5188–5192, 1976.

Chapter 4: Outlook

Future Approaches to Lower Cost and/or Higher Efficiency

Rationale

Not so long ago, the module cost was a dominant component of the total installed cost of a PV system. Therefore attention was correctly placed on reducing module costs. These module price reductions have gotten to such a point that a majority of the system cost is now attributed to other factors. These include "hard" balance of system components like racking, wiring, and inverters, and "soft" balance of systems like installation labor, permitting, and financing.[1]–[3]

With the majority of costs now outside the module, there has been some movement of innovation toward tackling these other non-module costs. Quick-connect mounting systems can save installation time and reduce installation errors. Streamlined permitting by some local jurisdictions can speed installation. Power purchase agreements (aka solar leases) have enabled no-money-down solar systems for homeowners in some states. It would seem that present modules are nearly “good enough” or will be soon as they ride their current cost reduction curves.

Yet modules continue to require innovation. The size of a typical residential roof is not normally a limiting factor when installing a residential solar system, but that doesn't mean higher efficiency modules wouldn't be desirable. Assuming modules are all manufactured for a similar areal cost ($\$/m^2$), a higher efficiency module can sell for more while maintaining the same capital intensity ($/W). This allows the module manufacturer to have a higher margin. In the larger system, installing the same nameplate capacity with fewer modules reduces both labor and roof load. It also reduces aesthetic concerns related to roof-mounted panels. In utility-scale installations where cost of land is a consideration, higher efficiency modules allow equivalent nameplate capacity systems to be installed over fewer acres.

The approaches to improving efficiency are briefly reviewed below. Some approaches attempt to slightly improve the efficiency of today's single-junction devices. Other approaches require new system architectures. Lastly, the most distant approaches utilize both new devices in new architectures.

Optical Approaches Independent of the Cell Itself

- *Optical Upconversion*

Optical upconversion is a non-linear process whereby multiple low energy photons are absorbed and then emitted as a single higher-energy photon. When upconverters are applied to the back of the solar cell they will ideally absorb all the below-bandgap light that was transmitted through the cell and re-emit it back into the solar cell.

The materials most widely utilized today are lanthanide-doped fluoride materials. Lanthanides are used as dopants because they can create long-lifetime intermediate electronic states that photons can be

sequentially absorbed into. The long lifetime is attributable to the f-electron shielding of the lanthanides which limits their interaction with the rest of the lattice. Fluoride matrices are preferable since they are very stable, able to accommodate high dopant loadings, and have a phonon structure that resists thermalizing the lanthanides' intermediate states.

There are several challenges to the successful utilization of upconversion. The fluoride matrix material is a wide bandgap material while the lanthanide dopants have very weak and narrow absorption. The weak absorption is due to their low concentration. Since they are well-shielded within the lattice, their optical spectra are qualitatively similar to atomic spectra as if they were not part of a solid system. One may increase the lanthanide dopant concentration in order to increase the absorbance within the dopant's linewidth, but then the dopants become less isolated in the lattice and upconversion efficiency tends to decrease.

Since upconversion is a nonlinear process, it tends to work more effectively at higher photon flux. This means that upconversion will be more efficient in concentrated systems with a higher flux than a 1-sun system.

Once upconversion has occurred emission is expected to be isotropic. As a result, half the emitted photons would be emitted away from the solar cell. This necessitates that an optical element be used behind the upconverter material to redirect that emitted light back towards the solar cell. This element may be a mirror, but it may be possible that a white, scattering backing material, such as clean Teflon, could be acceptable.

In the context of solar cells, upconversion refers to conversion from near-infrared up to visible. However, for the sake of completeness, it should be noted that there are molecularly system that upconvert within the visible spectrum or from visible to the ultraviolet. These systems may be more useful when dealing with wide-bandgap semiconductors such as those used in water-splitting electrochemical systems.

- *Optical Downconversion*

Optical downconversion is the process of absorbing a high energy photon and then re-emitting it at a lower energy. The difference in energy between the absorbed and emitted photons is lost as heat. Dowconversion is useful when the solar cell has a low quantum efficiency in one part of the solar spectrum. This low efficiency region is typically in the blue since those photons are absorbed very close to the semiconductor surface and are therefore more prone to recombine at the surface than carriers excited deeper within the semiconductor. Improved surface passivation may improve the efficiency of the blue region to the point where the cost and efficiency of downconversion is not sufficient to be justifiable.

Optical downconversion is commonly practiced in displays. In display applications, lumophores are pumped with UV or deep blue light, typically from a gallium nitride LED, and re-emit it at visible frequencies. For this reason, downconversion materials have been very well studied.

Downconversion only improves solar cell efficiency if enough photons are downconverted to and then collected at the lower energy. For example, assume a solar cell with an external quantum efficiency of 50% in the blue and 90% in the green. Also assume that the cell is optically thick at both wavelengths so the external quantum efficiencies are also their internal quantum efficiency. There are at least two possible inefficiencies in this system: the downconversion of blue-to-green photons and the collection of green photons after they've been emitted. The first efficiency is the 'quantum efficiency' or 'quantum yield' of the lumophore. This can be near 100% for some quantum dots but may only be 60-70% for more conventional, cheaper lumophores.

Once the green light has been emitted it must be absorbed by the solar cell to be useful. However, lumophores tend to emit isotropically. That means that, assuming a planar solar cell, half the photons will be emitted away from the device. If half the photons are lost in this way even a 100% quantum efficient lumophore will still cause a decrease in solar cell efficiency due to loss of photons and thus current. In the base case without downconversion, 100 blue photons, collected with 50% efficiency, result in 50 collected carriers. In the downcoversion case, 100 blue photons are converted to 100 green photons, then only 50 green photons are subsequently absorbed at 90% efficiency, resulting in 45 collected carriers. For this reason, unless the blue response of the solar cell is especially poor, the isotropic emission of the downconverter prevents net gain of usable photons.

Isotropic emission may be overcome with a thoughtfully designed optical element. More realistically, a lumophore with directed emission would be beneficial. Anisotropic nanocrystals are known to emit in preferred directions. These particles might provide a basis for photovoltaically-useful downconversion.

- *Quantum cutting*

Quantum cutting refers to optically splitting one high energy photon into several lower energy photons. In contrast to downconversion, which only emits one photon per absorbed photon, quantum cutting can emit multiple photons per absorbed photon.

Quantum cutting is typically observed in lanthanide-doped materials similar to those used for upconversion. Long intermediate state lifetimes are required to allow time for radiative recombination to occur, as opposed to non-radiative relaxation. Typical materials, including quantum dots, which have well separated energy levels, have fast non-radiative relaxation that do not permit the sequential radiative emission to occur. A typical non-radiative lifetime is sub-nanosecond whereas radiative lifetimes are often hundreds of nanoseconds or longer. The result is that excited carriers non-radiatively relax long before they can radiatively emit.

A new organic-inorganic approach to quantum cutting has emerged by coupling semiconducting organic molecules to inorganic quantum dots. In back-to-back papers, tetracene was coupled to PbS nanocrystals and pentacene was coupled to PbSe nanocrystals. In these examples, the long-lived state required for quantum cutting is the triplet state on the organic. That triplet state is converted to emission by interaction with the strong dielectric strength and high radiative efficiency of the quantum dots.

- *Anti-reflection coatings*

A complete discussion of optical approaches to improve cell efficiency must include anti-reflection coatings. Owing to the high refractive index of most PV-relevant semiconductors above their bandgaps, reflection can be 30-40%. By depositing layers of an intermediate index material with specific thickness, the reflection can be minimized. The thickness can be optimized with an understanding of constructive and destructive interference, but the optimization is necessarily angle- and wavelength-dependent. Multiple layers can extend the bandwidth of the anti-reflection properties but also adds cost.

Besides having a wide bandgap and appropriate refractive index, anti-reflection coatings often serve the dual purpose of electronic surface passivation. This further limits the number of available materials.

Semiconductor Material Approaches that Improve Existing Cells

- *Lighting trapping for increased J_{sc}*

Light absorbed by a solar cell has the potential to be converted into useful current. Given a functioning device, it reasons that if the device could be made to absorb more light it would increase its efficiency by increasing the short circuit current, J_{sc}. This is especially relevant for weakly absorbing indirect bandgap materials, such as crystalline silicon.

Much has been written about light trapping of bulk and thin film semiconductors. These approaches typically rely on texturing the semiconductor layer to better couple light into the layer. Plasmonic structures are often used when coupling to thin film materials. The near-field length scale of the enhanced electric field is well-matched to the sub-wavelength thickness of the thin film.

There are potential challenges to implementing engineered textures on semiconductor films. Top side texturing typically requires etching. For an engineered texture, that etch may need to be masked, which adds additional steps (and costs) to production. The increased surface area of the top surface would also be expected to increase surface recombination, which further increases the importance of surface passivation. Backside texturing on a wafer substrate would have similar etch challenges. On a thin film deposited on foil, the foil itself would presumably need to be textured before the thin film is deposited. The process for texturing the metal, like that for etching the semiconductor, adds cost and complexity. Those costs must be weighed against the benefits of light trapping.

A novel approach is to use discrete, rather than continuum, semiconductors, such as sparse, aligned, nanowire arrays. In these arrays the optical cross section of the semiconductor is greater than its physical dimensions. Like other light trapping structures, these sparse nanostructure arrays absorb more light than equal-volume, continuous thin films models would predict. There are undoubtedly issues to efficiently using such sparse arrays, including their high surface area to volume ratios which enhance surface recombination. It remains to be seen if their sparse structure can be utilized efficiently. One possibility is to utilize their high surface area and strong absorption as photoelectrodes in photoelectrochemical systems.

One approach not readily utilized in light trapping is the incorporation of light trapping structures within the absorber layer rather than on either side of it (ie. surface texturing). There are clear reasons that incorporating light trapping into the absorber layer may be difficult. In epitaxial materials the introduction of another material can degrade epitaxy. In any material the foreign structure may serve as a recombination center. In the context of solution-deposited materials it's possible to combine the optical structure, in this case a metal plasmonic nanoparticle coated in an insulating material, with the solution-processed semiconductor and co-deposit the two components together.[4] The insulating coating should reduce the likelihood of recombination at the plasmonic particle. In any case, optical structures will have an intrinsic absorption (ie. be "lossy") so that loss must be balanced against any enhancement they provide the device.

- *Light trapping for increased V_{oc}*

Another benefit of light trapping that arises alongside increased current is increase voltage. When more light is absorbed in a cell, the photo-excited carrier population increases. This leads to the quasi Fermi levels splitting further, which manifests as additional voltage. The key is that absorbed light is a volumetric quantity—if the same amount of light can be absorbed with half the volume of semiconductor that's equivalent to doubling the light flux on the original semiconductor volume. We expect an additional 60 mV of open circuit voltage for every decade increase in light intensity. While it may not be practical to reduce the thickness of a device that is only a few microns thick to begin with by an order of magnitude, any reduction in semiconductor layer volume should have benefits of increased voltage alongside any increase in current.

- *Higher radiative efficiency for increased V_{oc}*

The open circuit voltage of a solar cell is related, in part, to its internal radiative efficiency at open circuit. This can be understood as the cell's ability to maintain a population of photons which contributes to an increase in the splitting of the quasi Fermi levels. Higher radiative efficiency allows the photons to be absorbed and then re-emitted (ie. "recycled) more times, thus maintaining the quasi Fermi level splitting for longer.

It should be noted that internal, not external, radiative efficiency is valued. Since only a small portion of the photons will be able to escape the cell on any given pass, a photon inside the cell does not necessarily translate to a photon outside the cell. Photons cannot always escape due to the restricted angles of the escape cone, defined by Snell's Law, that allow photons to refract out of the cell rather than be totally internally reflected back into the device. For this reason, external efficiency is always lower than internal efficiency except in the limit of 100% efficiency. The difference between the internal and external efficiency grows greater as the refractive index of the semiconductor increases. This is because the escape cone of a higher index material is smaller than the escape cone of a lower index material.

The origin of imperfect radiative efficiency depends on the semiconductor. A few generalizations can be made though. We expect direct bandgap semiconductors to perform better than indirect bandgaps since materials that absorb strongly also tend to radiate quickly. We also expect mono-crystalline

materials to outperform poly-crystalline analogs. Low surface recombination and bulk defects, whether they are dislocations or stoichiometry imperfections, are desirable.

Concentrating System Architectures

Concentration is desirable because it increases the V_{oc}, and sometimes the fill factor, of devices. The increase in V_{oc} is due to the higher concentration of excited carriers in the device which leads to an increased splitting in the quasi Fermi levels. Ideally, we expect 60 mV additional V_{oc} per decade of concentration.

One challenge of concentrating systems is that the cells must have particular characteristics. They must be able to handle the increased light flux associated with concentration. In poor devices, parasitic processes like Auger recombination that are more prevalent at high excited carrier populations can undermine gains from concentration. The cells will also likely increase in temperature, even with robust heat sinks. This is one of the reasons that III-V cells, which degrade less per unit increase in temperature than silicon or thin film cells, are often used in concentrating systems. The commercialization of new cells suitable for use with concentration could aid these systems, though system costs are not dominated by cell costs so this may not be the key cost reduction moving forward.

It should be mentioned that concentration is a sliding scale. Most cell technologies can tolerate a few suns of light without significantly heating or otherwise decreasing in efficiency. However, concentration is more conventionally used to refer to system with hundreds of suns of illumination where only certain devices can take advantage of such a high flux.

- *Geometric concentration*

Geometric concentration, colloquially represented by a telescope focusing light from a big area to a small area, is the most common form of concentration. These concentrator require (1) that they have tracking hardware that follows the sun and (2) the sunlight incident on them is direct, rather than diffuse. This is due to geometric concentrators being governed by ray optics. Only rays of light that are direct and normally incident upon the concentrator will be concentrated.

The requirement for direct light is also the reason that tracking is required. For the concentrator to be facing the sun at all times in order to satisfy the ray optics requirements requires tracking hardware that moves the orientation of the concentrator. Such trackers can be either one-axis (following the sun on a daily cycle) or two-axis (following the sun on both daily and seasonal cycles).

A key challenge for geometric concentrators is finding appropriate locations for them. Until just recently, a major of solar PV installations as measured by installed capacity were on rooftops. Tracking hardware is generally considered incompatible with rooftop installation. Aside from the question of rooftop compatibility, a geometric concentrator should be in an area with as little diffuse light as possible. This can be challenging since even deserts like the Mojave still have 20% diffuse light. This diffuse light will not be concentrated and is therefore not utilized. If too much light is unutilized the energy output of the system is reduced.

- *Luminescent concentration*

Luminescent concentration is the use of a lumophore to absorb light at high energies and re-emit it at lower energy. This shift in the frequency of light is the means of generating concentration. For instance, a lumophore could absorb blue light and emit it as green light. The difference in energy between absorption and emission, known as the Stoke's shift, governs the maximum allowable concentration. A bigger Stoke's shift permits a higher level of concentration.

A high-performance luminescent concentrator must have a few key characteristics. First, it must have high luminescence efficiency—the efficiency with which absorbed light is re-emitted at a lower energy. Second, the absorption at the lower energy should be minimized compared to the absorption at the higher energy to reduce re-absorption of light that has already been Stoke's shifted. Of course, if the lumophore is perfect (ie. 100% luminescence efficiency) then re-absorption would not matter because re-absorption would never parasitically consume photons. In real devices that achieve high concentration factors, photons will have to propagate inside the waveguide for a long distance. Therefore, as the concentration factor increases so does the photon's path length and therefore its chance of intersecting another lumophore and being parasitically reabsorbed. Lastly, the waveguide structure that traps the shifted photons needs to be nearly lossless, meaning that photons cannot escape. At present, lumophores based on quantum dots have achieved or can be reasonably expected to achieve the first two objectives, but developing waveguides with very high photon collection efficiency is presently limiting.[5]–[7]

Nanocrystals may have a role to play in forming the high-quality waveguides. There’s an open debate as to how the refractive index of materials change as they are quantum confined. Due to the high index of many II-VI materials, especially lead sulfide, below their bulk bandgaps it may be possible to make high-index films at relevant red or near-infrared wavelengths that are optically transparent. This may be achieved by quantum confining the II-VI materials to a point where their bandgap is above the wavelength of interest.

A key advantage of luminescent concentration compared to geometric concentration is that the incident light does not have to be direct. Instead, it can also be diffuse. Since the incoming light doesn't have to be direct, there's the potential for luminescent concentrators to work without tracking. Eliminating tracking hardware could be the key to achieving cost reductions and improving reliability enough to make the technology practically viable. For this reason, luminescent concentrators could be compatible with the flat-panel form factor of modules today.

In a solar cell, there's a tradeoff between the additional V_{oc} gained from the luminescent concentration and the current lost due to the lack of absorption of light in the region of the Stoke's shift, assuming perfect photon delivery efficiency of the luminescent concentrator for those photons it does absorb. In the limit of a perfect solar cell and a luminescent concentrator that does not lose any absorbed photons, these losses will perfectly cancel each other. This is important to note because, unlike geometric concentration, luminescent concentration cannot break the so-called Shockly-Quessier limit that

governs single-junction solar cells under 1-sun illumination. This unfortunate conclusion means these systems cannot have superior efficiency to their flat-plate analogs.

Due to its inability to improve efficiency, luminescent concentration is only likely to be practically useful in systems where the area of cell must be minimized for cost reasons. It's imaginable that a module could be designed that uses small areas of high-cost, high-performance solar cells coupled to a large area of comparatively cheap luminescent concentrator. It's not clear at present what type of solar cell would need this treatment. The most costly solar cells today are multi-junction III-V devices, but since a luminescent concentration converting much of the solar spectrum to one energy the spectrum-matching properties of multi-junction cells are unlikely to be realized with a luminescent concentrator. It should be mentioned that there have been multi-colored, layered luminescent concentrators based on dyes with discrete absorption. However, these dyes are generally inferior lumophores to inorganic materials due to their smaller Stoke's shifts.

New Cell Technologies

- *Multi-junction cells on lattice-matched substrate*

The devices have traditionally been based on III-V materials. Their high performance is not disputed, rather it's their cost that has been identified as limiting their adoption. For instance, these devices are often used with geometric concentrators. The concentrators both decrease the area of expensive cell required and increase the performance of the device because of the increase light flux. In turn, the high efficiency of the cell helps justify the cost of the concentrator and tracking hardware. However, given the challenges with tracking identified previously it appears the market potential for these cells coupled to concentrators is limited. If these cells were to be used without concentrator, presumably in flat-panel, 1-sun form factors, then their areal cost would have to be reduced significantly.

- *Multi-junction on traditional single-junction bottom cell*

A newer approach to achieving the efficiency benefits of multi-junction cells without the manufacturing cost of epitaxial III-V devices is to add another junction on top of an existing and well-developed cell that is currently deployed as a stand-alone single junction device. For instance, various materials have been proposed to be the top cell with a silicon bottom cell, including CdSe, GaInN, GaAs, organics, and perovskites.

Determining the requirements under which a top cell will boost the overall performance of the device can be tricky. Ideally the top cell would have a comparable or greater EQE at a given wavelength than the bottom cell. This is a challenging standard to meet since most well-developed silicon and CIGS devices which would likely be the bottom cell have EQEs around 90% in the visible spectrum which leaves very little room for further EQE improvement in the top cell compared to the bottom cell. Unfortunately, candidate top cells tend not to be as well-developed and are therefore less efficient than the bottom cells they are proposed to sit over.

Alternatively, one can argue that since the high-energy photon will be extracted at a higher voltage from the top cell than they would be in the bottom cell a lower EQE may be acceptable in the top cell. However, given the additional cost and complexity in adding the top cell it seems unlikely that such a compromise on performance would be acceptable.

- Metal-insulator-semiconductor cells

Metal-insulator-semiconductor (MIS) cells are an alternative to p-n or p-i-n cell architectures. In such a device, a metal gate is biased to form an inversion layer in the semiconductor across an insulator layer. There is a second metal electrode on the far side of the semiconductor to complete the circuit.

MIS cells have several advantages. They are processed at low temperatures, so they should have a lower production cost and level of thermal defects. There is no performance loss due to diffused dopants either. If light is incident from the insulator side, the collecting junction is near the surface of the cell, which should enhance blue response.

MIS cells were challenging to fabricate in practice because the insulator layer needs to be robust and stable, but also thin enough to allow charges to tunnel through to be collected by the gate electrode. Recently, Silevo has commercialized a silicon-based MIS device.

The MIS architecture can theoretically be used with any lightly doped semiconductor that is unable to be doped both n- and p-type, which makes it a potential architecture for many thin film materials. However, the insulator must meet two conditions. First, it must be stable at an appropriate thickness. Second, it must passivate the semiconductor surface. Those are difficult to achieve simultaneously.

The other challenge is applying a finger grid for use as the gate electrode cost-effectively, which today requires lithography. Unlike frontside current-collecting bus bars, a gate electrode needs to be very fine to deliver a uniform electric field through the dielectric and into the semiconductor. A realistic finger grid is likely not optimal since the lines would be too far apart and thus the induced field in the semiconductor would not be uniform. A transparent conductor that is sufficiently transparent and conductive would solve that challenge.

- *Multi-junction cells with more than two terminals*

Traditional multi-junction cells, regardless of their fabrication method and number of junctions, are wired in series through connection by tunnel junctions. These devices therefore only have two terminals—one at each side of the device. Series connections means that the cells must be current matched. Current matching means the current of the entire device is limited by the junction that produces the smallest amount of current. In theory the bandgaps of the various junctions can be tuned to equally divide the solar spectrum, but practical considerations make this difficult. For instance, precisely tuning the bandgap of the junction can be difficult. The solar spectrum is also somewhat depends on location, time of day, and time of year.

For these reasons there is a small efficiency advantage gained by wiring the cells electrically in parallel rather than series. Such an arrangement removes the requirement of current matching. However,

making two terminal connections to each junction adds complexity. Therefore, it appears that parallel electrical wiring may be accompanied by module architectures that place the cells optically in parallel (set next to each other) rather than optically in series (stacked on top of each other). The benefit versus added cost and complexity of more than two terminals needs to be evaluated. It may be that a mix of parallel and series electrical connection, possibly coupled to both parallel and series optical arrangements may be optimal.

- *Intermediate band cells*

Intermediate band (IB) devices have the spectrum-matching potential of multi-junction cells without the complication of having two different materials to form the separate junctions. In an IB cell, there is a third level positioned in the bandgap. This additional level allows sequential two photon absorption (from the valence band to the intermediate band and then from the intermediate band to the conduction band) to generate useful work. In this way, an IB cell has the potential to utilize lower energy photons that would otherwise transmit through the absorber layer.

IB cells have two dominant architectures. In the first, a semiconductor is heavily doped in such a way that the dopant atoms form the intermediate band. Since the concentration of dopants often exceeds the dopant's solubility in the matrix semiconductor these layers must be formed by molecular beam epitaxy, ion implantation followed by pulsed laser recrystallization, or some other technique that can produce metastable material. Due to the large lattice distortions caused by the heavy doping, these films are often poly-crystalline. This approach offers a vast parameter space of dopants, matrix semiconductors, and deposition techniques which makes it appealing for ongoing investigations. The dopant used can be isovalent or heterovalent. Isovalent dopants have the advantage that they should not perturb the Fermi level within the material, which should allow independent control of the intermediate band and position of the Fermi level to be within that band. Heterovalent dopants are appealing because there are many more of them and thus open a larger parameter space.

The second technique uses superlattices to form the intermediate band. While superlattice quantum wells are idealized as perfect barriers, the wavefunction of the smaller bandgap region inevitably bleeds into the larger bandgap region. If the smaller bandgap lies at least partially within the larger bandgap then the electron density from the levels of the smaller bandgap region will bleed into the larger bandgap region and create mid-bandgap state(s). These devices can be difficult to fabricate and the optical transitions involving the midgap states are often very weak.

IB cells have traditionally had poor performance due to either poor absorption through the intermediate band and/or because the material quality of the resulting film is degraded by processing, such as heavy doping. One approach is to use the high miscibility and alloying ability of the III-V materials to form appropriate energy levels. By using all III-V materials the doping is also isovalent. However, some III-V materials are intolerant of grain boundaries and other defects, so growing high quality material will likely be a challenge. A second approach is to pursue materials, such as II-VI materials, that are known to perform well in the poly-crystalline form often resulting from deposition and have been doped widely in the past. These materials offer a vast parameter space to explore different material compositions.

- *Nanowire or microwire arrays*

Arrays of semiconductor wires, whether with diameters on the nanometer or micrometer length scale, have gained attention for their exceptional ability to absorb significantly more light per unit volume than their thin film counterparts.[8] When arrays are fabricated by vapor-liquid-solid (VLS) growth or some other direct-from-gas method they are kerfless, which gives them the potential to have very high material precursor utilization efficiency. Indeed, these arrays are still appealing for use with expensive semiconductor materials.

Due to their form factors, arrays have other advantages. When heterojunctions are formed, the radial structure allows strain to be relaxed out. Radial junctions can also be formed, which have been shown to help charge separation in materials with short diffusion lengths.

Despite their advantages, array-based cells do not perform comparably to their thin film analogs. This performance difference is attributed to the increased surface area of the arrays compared to thin films. For instance, it is known that photons absorbed near the surface of thin film or wafer cells have a greater chance of parasitically recombining at the semiconductor surface. This is the origin of poor EQE in the blue portion of the spectrum compared to the rest of the visible spectrum. In a wire absorber much more of the volume of the absorber is now close to a surface. Effective passivation is therefore critical for array devices to achieve their full efficiency.

- *Quantum dots*

Quantum dots hold the promise for bandgap-tunable absorber layers that can be solution-processed at room temperature. In the face of increasingly efficient competition, including organic and perovskite cells, both of which are also solution-processed, the question is whether quantum dot-based devices can be efficient enough to compete.

Solution processing is industrially known to be vastly cheaper than vacuum deposition. A bladecoater is 2000 times cheaper than an equivalent sputtering system. If ovens and dryers must be added, the capital cost advantage is still a significant 10 times less.

Quantum dots offer a couple of other opportunities for device engineering. Their bandgaps have long been known to be tunable based on the dot's diameter. More recently, it has been shown that different surface ligands can change the energy positions of the HOMO and LUMO relative to vacuum.[9], [10] Doping levels have also been adjusted in both the n- and p-type directions.[11], [12] These degrees of freedom in setting energy and Fermi levels allows quantum dots to serve as selective contacts, aka blocking layers, or for quantum dot absorber layers to have a graded energy landscape to assist in charge collection. Like other solution-processed material, they have a greater ability to incorporate other structures, such as light trapping particles, within their absorber layers or conform over engineered substrates compared to epitaxial films.

It has recently been proven that quantum dot solids are limited by trap states rather than by their albeit-rather-low mobility. As a result, free charges will tend to be trapped in these states rather than diffuse

as would be expected based on mobility and lifetime values. Synthesis and surface passivation techniques will undoubtedly be developed to reduce the trap state density in the future.

Quantum dots should not be viewed as merely a possible absorber layer material though. As high-quality lumophores, quantum dots have potential in optical downconversion and luminescent concentration. Their large ability to incorporate dopants has already made them useful as selective contacts, such as those made by Innovalight.

- *Multiple exciton generation & impact ionization*

Multiple exciton generation and impact ionization are related processes where one high-energy photon produces more than one electron-hole pair. This process is exceedingly rare in bulk materials but its probability is enhanced in quantum-confined structures like quantum dots and quantum rods. Recently, devices have been built based on quantum dots that achieve over 100% EQE at UV photon energies. Since a photon needs to be several multiples of the bandgap energy in order to induce MEG, absorber layers in these devices tend to have smaller-than-typical bandgaps. Due to the bandgap and the thinner-than-normal absorber layer that was not optically thick, these devices do not currently produce high efficiencies.

It should be noted that all-optical processes, like quantum-cutting, can be equivalent to opto-electronic processes like MEG in the regard that they both solve the problem of 'blue loss'. 'Blue loss' is the loss of free energy of a high energy photon absorbed across a traditional junction. By segmenting the high-energy photon, either optically into multiple photons or electrically into multiple excited carriers, more of the free energy can be captured. For this reason, optical processes should be compared to their opto-electronic counterparts when evaluating the optimal solution for mitigating solar cell losses. A similar analogy can be made when evaluating solutions to 'red loss' where an optical method, upconversion, is equivalent to an opto-electronic method, intermediate band cells.

Concluding Thoughts

The potential for future innovation in the area of cells and modules in the photovoltaic industry appears robust. There appear to be technical approaches to achieve different goals: incremental improvement of existing technology, "add-on" technologies for improving efficiency but without interfering with the cell, and entirely new device architectures.

The optical approaches that are independent of the cell are particularly appealing because they do not require any modification to the cell manufacturing process. That may be appealing to manufacturers who are hesitant to modify their device fabrication. The question is not whether these processes will increase efficiency since they certainly will. Instead, the real question is whether they can be implemented with the required durability and at the right cost to increase the value of existing modules. These are questions that the academic community is traditionally uninterested and ill-equipped to answer. However, this presents an excellent entrepreneurial opportunity because it sits beyond the scope of the academic lab but isn't something traditional manufacturers are equipped to pursue themselves.

In the future, it seems there's an arc of progress towards higher efficiency cells. What's unclear is how high is 'high efficiency'. It may be that with continuing incremental efficiency improvements, cost reductions, and scaled manufacturing that wafer silicon may not be the most efficient options, but will be sufficiently cheap that a slightly lower efficiency won't matter. Therefore, it would appear that any new entrants would have to have radically lower capital intensity (ie. $/watt). Such an improvement might come from higher efficiency devices using today's manufacturing processes. In this way, there's more of an emphasis on the denominator of capital intensity. Alternatively, one could implement today's devices with new, cheaper manufacturing processes. That places the emphasis on the numerator of the capital intensity. An ideal innovation would achieve both.

On the manufacturing side, it seems that the elimination of vacuum processes will be essential. Inks, electrodeposition, and chemical bath deposition are all appealing in this regard. Inks, which would presumably be sintered later, have been tried at Solexant, a printed CdTe manufacturer, but the cost of producing the ink was prohibitive. There might also be room for vapor-based solutions, but any reacting gas process would likely soon resemble a chemical vapor deposition process with a high capital intensity to match.

Higher device efficiency and concentration will likely be complementary technologies. Higher efficiency devices have typically been able to benefit from concentration while concentrators can leverage higher efficiency devices to justify their hardware costs. Since implementing tracking concentration on rooftops has been difficult, it is likely these technologies will see use in flat-land utility scale installations first.

What the actual device will be is unknown. However, if a new junction is going to be paired with an existing, well-performing device, such as a silicon wafer-based cell, then the new junction would likely have to be as good as the silicon-based device since the new junction will be using photons that the silicon cell would otherwise be utilizing. This is a tough standard given the extensive work on silicon. For this reason, new combinations of junctions might make sense. Intermediate band devices are particularly compelling since they may bypass some of the challenges of current epitaxial multi-junction cells.

References

[1] P. Denholm, R. M. Margolis, S. Ong, and B. Roberts, “Break-Even Cost for Residential Photovoltaics in the United States : Key Drivers and Sensitivities Break-Even Cost for Residential Photovoltaics in the United States: Key Drivers and Sensitivities,” *NREL Tech. Rep.*, no. December, 2009.

[2] A. Goodrich, T. James, and M. Woodhouse, “Utility-Scale Photovoltaic (PV) System Prices in the United States: Current Drivers and Cost-Reduction Opportunities Residential , Commercial , and Utility-Scale Photovoltaic (PV) System Prices in the United States : Current Drivers and Cost-Reductio,” *NREL Tech. Rep.*, no. February, 2012.

[3] K. Ardani, D. Seif, R. Margolis, J. Morris, C. Davidson, S. Truitt, and R. Torbert, “Non-Hardware (‘Soft’) Cost- Reduction Roadmap for Residential and Small Commercial Solar Photovoltaics, 2013-2020,” *NREL Tech. Rep.*, no. August, pp. 2013–2020, 2013.

[4] D. Paz-soldan, A. Lee, S. M. Thon, M. M. Adachi, H. Dong, P. Maraghechi, M. Yuan, A. J. Labelle, S. Hoogland, K. Liu, E. Kumacheva, and E. H. Sargent, “Jointly Tuned Plasmonic − Excitonic Photovoltaics Using Nanoshells,” *Nano Lett.*, vol. 13, pp. 1502–1508, 2013.

[5] N. D. Bronstein, L. Li, L. Xu, Y. Yao, V. E. Ferry, a P. Alivisatos, and R. G. Nuzzo, “Luminescent solar concentration with semiconductor nanorods and transfer-printed micro-silicon solar cells.,” *ACS Nano*, vol. 8, no. 1, pp. 44–53, Jan. 2014.

[6] I. Coropceanu and M. G. Bawendi, “Core/shell quantum dot based luminescent solar concentrators with reduced reabsorption and enhanced efficiency.,” *Nano Lett.*, vol. 14, no. 7, pp. 4097–101, Jul. 2014.

[7] C. S. Erickson, L. R. Bradshaw, S. Mcdowall, J. D. Gilbertson, D. R. Gamelin, D. L. Patrick, U. States, and H. Street, “Zero-Reabsroption Doped-Nanocrystal Luminescent Solar Concentrators,” *ACS Nano*, vol. 8, no. 4, pp. 3461–3467, 2014.

[8] P. Krogstrup, H. I. Jørgensen, M. Heiss, O. Demichel, J. V Holm, M. Aagesen, J. Nygard, and A. Fontcuberta, “Single-nanowire solar cells beyond the Shockley-Queisser limit,” *Nat. Photonics*, vol. 7, no. April, 2013.

[9] P. R. Brown, D. Kim, R. R. Lunt, N. Zhao, M. G. Bawendi, J. C. Grossman, and V. Bulovi, “Energy Level Modification in Lead Sulfide Quantum Dot Thin Films through Ligand Exchange,” *ACS Nano*, vol. 8, no. 6, pp. 5863–5872, 2014.

[10] C.-H. M. Chuang, P. R. Brown, V. Bulović, and M. G. Bawendi, “Improved performance and stability in quantum dot solar cells through band alignment engineering.,” *Nat. Mater.*, vol. 13, no. May, May 2014.

[11] J. H. Engel and A. P. Alivisatos, “Postsynthetic Doping Control of Nanocrystal Thin Films: Balancing Space Charge to Improve Photovoltaic Efficiency,” *Chem. Mater.*, vol. 26, pp. 153–162, 2014.

[12] J. H. Engel, Y. Surendranath, and a P. Alivisatos, “Controlled chemical doping of semiconductor nanocrystals using redox buffers.,” *J. Am. Chem. Soc.*, vol. 134, no. 32, pp. 13200–3, Aug. 2012.

Appendix A

Formulas for calculation of defect formation energy

Cation substitution:

(Energy of cation-substituted system $[D_1Zn_{31}S_{32}]$ + energy of Zn_1) –

(energy of undoped $Zn_{32}S_{32}$ + energy of $dopant_1$)

Anion substitution:

(Energy of anion-substituted system $[D_1Zn_{32}S_{31}]$ + energy of S_1) –

(energy of undoped $Zn_{32}S_{32}$ + energy of $dopant_1$)

Tetrahedral interstitial:

(Energy of tetrahedral system $[D_1Zn_{32}S_{32}]$) –

(energy of undoped $Zn_{32}S_{32}$ + energy of $dopant_1$)

Octahedral interstitial:

(Energy octahedral system $[D_1Zn_{32}S_{32}]$) –

(energy of undoped $Zn_{32}S_{32}$ + energy of $dopant_1$)

Formula for conversion of complex dielectric function to complex refractive index

$$n = \sqrt{\frac{\sqrt{\epsilon_1^2 + \epsilon_2^2} + \epsilon_1}{2}}$$

$$\kappa = \sqrt{\frac{\sqrt{\epsilon_1^2 + \epsilon_2^2} - \epsilon_1}{2}}.$$

Where ε_1 is the real part of the dielectric function and ε_2 is the complex part of the dielectric function.

Formula for conversion of Complex refractive index to absorptivity

$\alpha = (4\pi k) / \lambda$

Our data is plotted with regard to energy, not wavelength, so the modified equation is:

$\alpha = (4\pi k)/(1240/\text{energy in units of eV}) \times 10^7$ to obtain the units of cm^{-1}

Figure 5.1

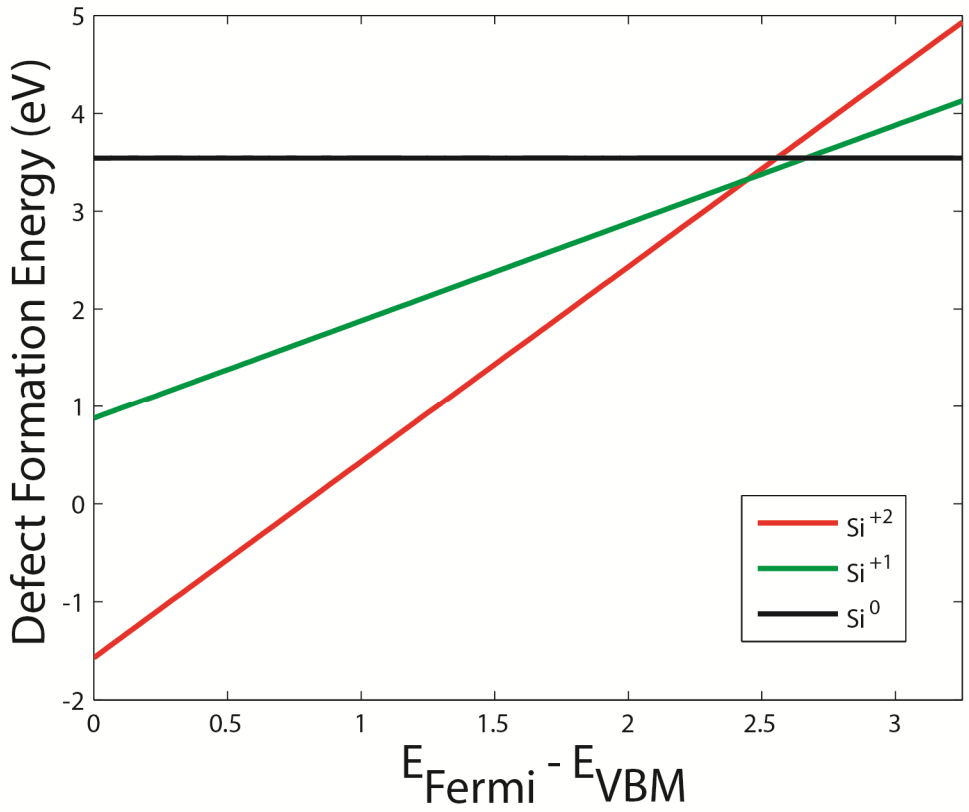

Defect formation energy for silicon in zinc sulfide for various oxidation states as a function of Fermi level calculated using HSE06. The most negative energy represents the preferred charge state of the dopant. Charge states that are preferred (Si^0, Si^{+1}, Si^{+2}) somewhere in the bandgap are solid lines. Si^{+2} is preferred over most of the bandgap.

Figure 5.1 represents the thermodynamic defect formation energy for Si-doped zinc blende zinc sulfide with one silicon dopant in a 64 atom supercell of zinc sulfide. The silicon is cation-substituted for zinc because that was found to be the thermodynamically preferred doping site.

The defect formation energy is calculated using the same formula, in this case the one for a cation substitutional defect, given in this Supporting Information but modified for the charged state of the doped system.[1] The charged system is ionically relaxed and then a self-consistent energy calculation is performed. Since there are only two electrons in the intermediate state, the highest positive charge the dopant can have is +2. Any additional electrons added to the neutral system would presumably populate the conduction band, so negative system charges are not calculated here since they do not involve the intermediate state.

Charged system defect formation energy = (Energy of $Si_1Zn_{31}S_{32}$ in charged state + Energy of Zn_1 in neutral state) – (Energy of $Zn_{32}S_{32}$ in neutral state + Energy of Si_1 in neutral state)

The charged system defect formation energy + (charge of system * eigen energy of VBM) is the y-intercept for Figure 5.1. The slope of the line is the integer charge of the system. The preferred charge state at a given energy is the one with the lowest defect formation energy.

Figure 5.2

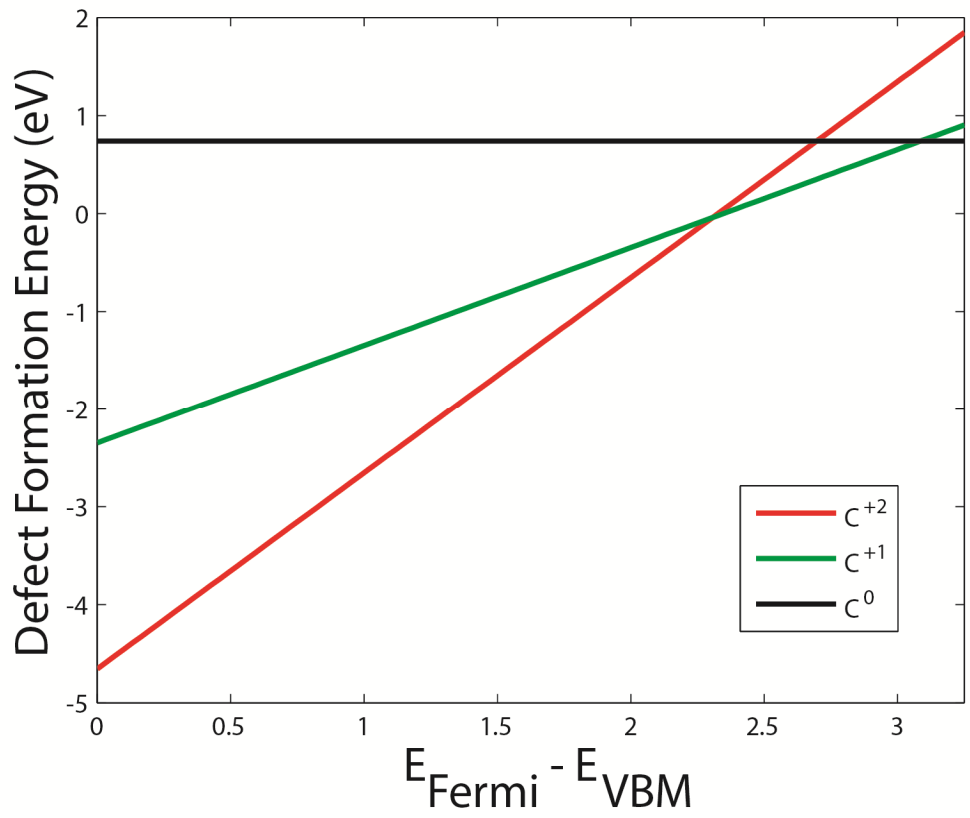

Defect formation energy for C-doped zinc sulfide for various oxidation states as a function of Fermi level calculated using HSE06. The most negative energy represents the preferred charge state of the dopant. Charge states of germanium that are preferred (C^{+2},C^{+1},C^{0}) somewhere in the bandgap are solid. This figure was calculated in the same manner as Figure 5.1.

Figure 5.3

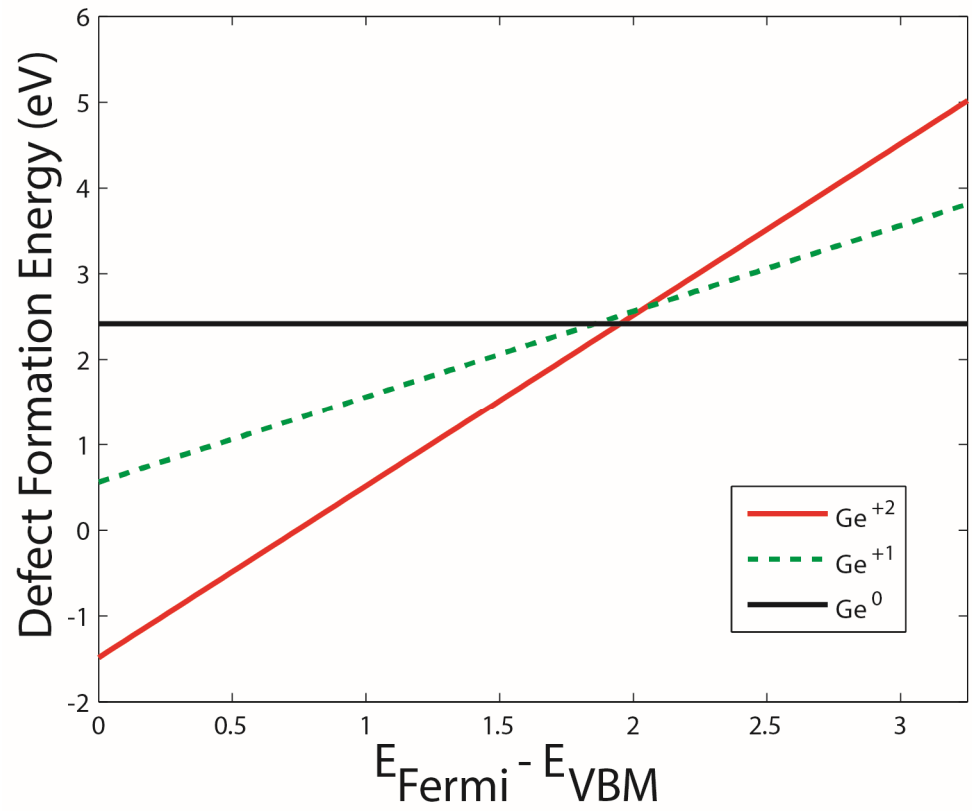

Defect formation energy for Ge-doped zinc sulfide for various oxidation states as a function of Fermi level calculated using HSE06. The most negative energy represents the preferred charge state of the dopant. Charge states of germanium that are not preferred at any Fermi level within the bandgap are dashed while charge states that are preferred (Ge^{+2}, Ge^{0}) somewhere in the bandgap are solid. This figure was calculated in the same manner as Figure 5.1.

Figure 5.4

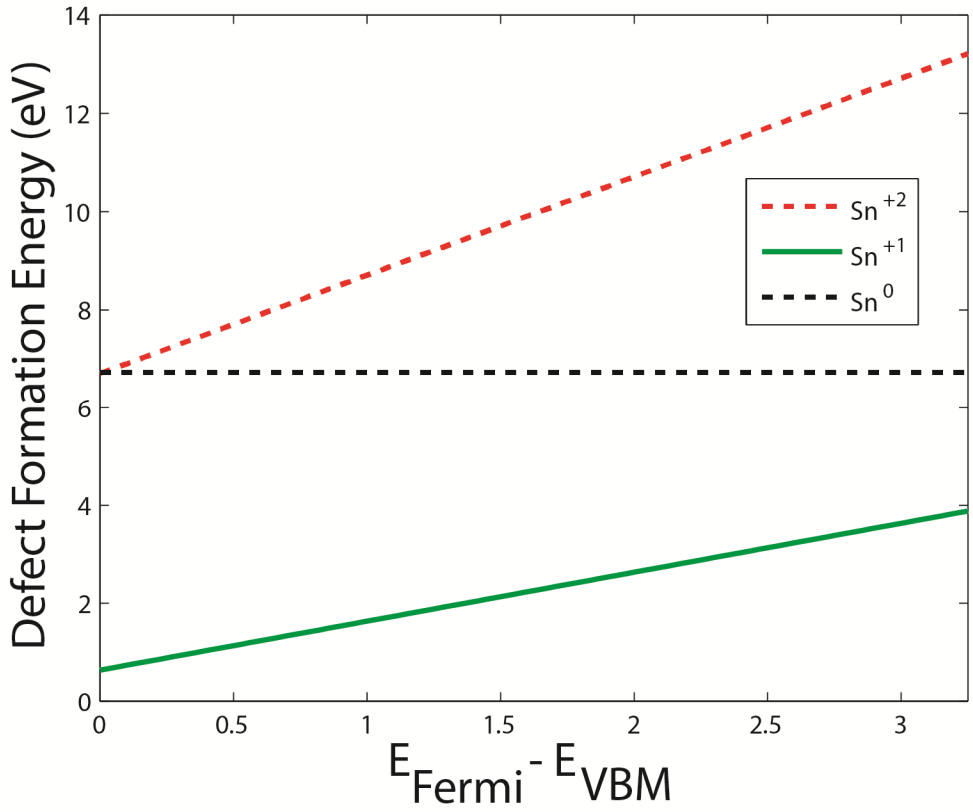

Defect formation energy for Sn-doped zinc sulfide for various oxidation states as a function of Fermi level calculated using HSE06. The most negative energy represents the preferred charge state of the dopant. Charge states of tin that are not preferred at any Fermi level within the bandgap are dashed while charge states that is preferred (Sn^{+1}) somewhere in the bandgap are solid. This figure was calculated in the same manner as Figure 5.1.

Figure 5.5

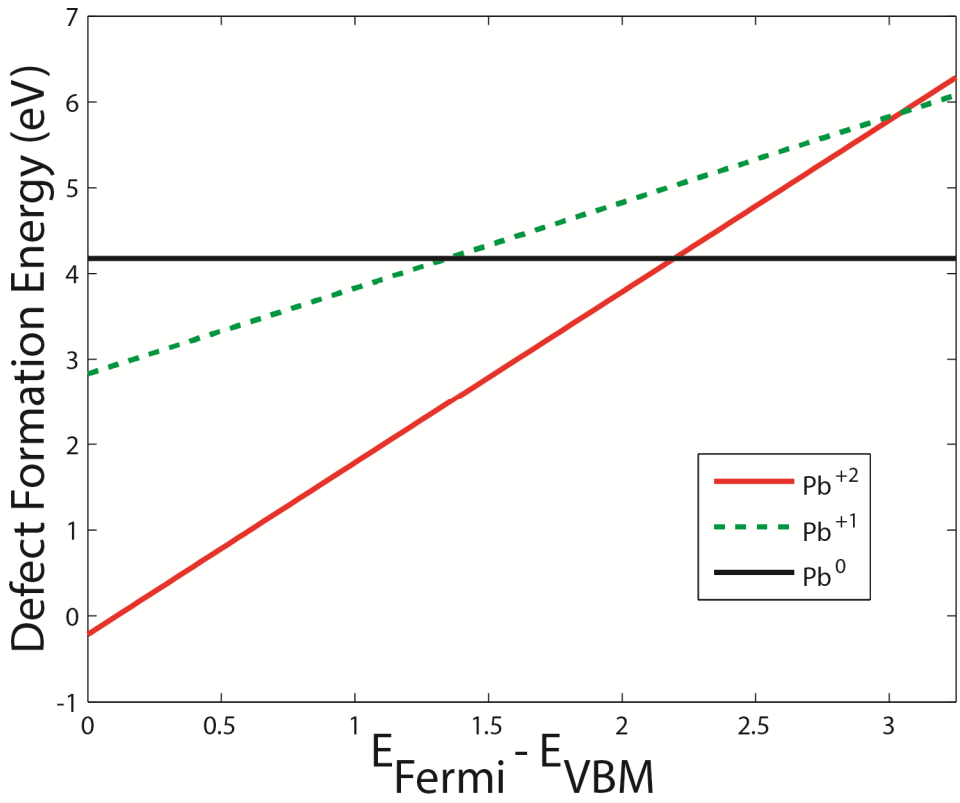

Defect formation energy for Pb-doped zinc sulfide for various oxidation states as a function of Fermi level calculated using HSE06. The most negative energy represents the preferred charge state of the dopant. Charge states of lead that are not preferred at any Fermi level within the bandgap are dashed while charge states that are preferred (Pb^{0}, Pb^{+2}) somewhere in the bandgap are solid. Pb^{+2} is preferred over most of the bandgap. This figure is calculated in the same manner as Figure 5.1.

Figure 5.6

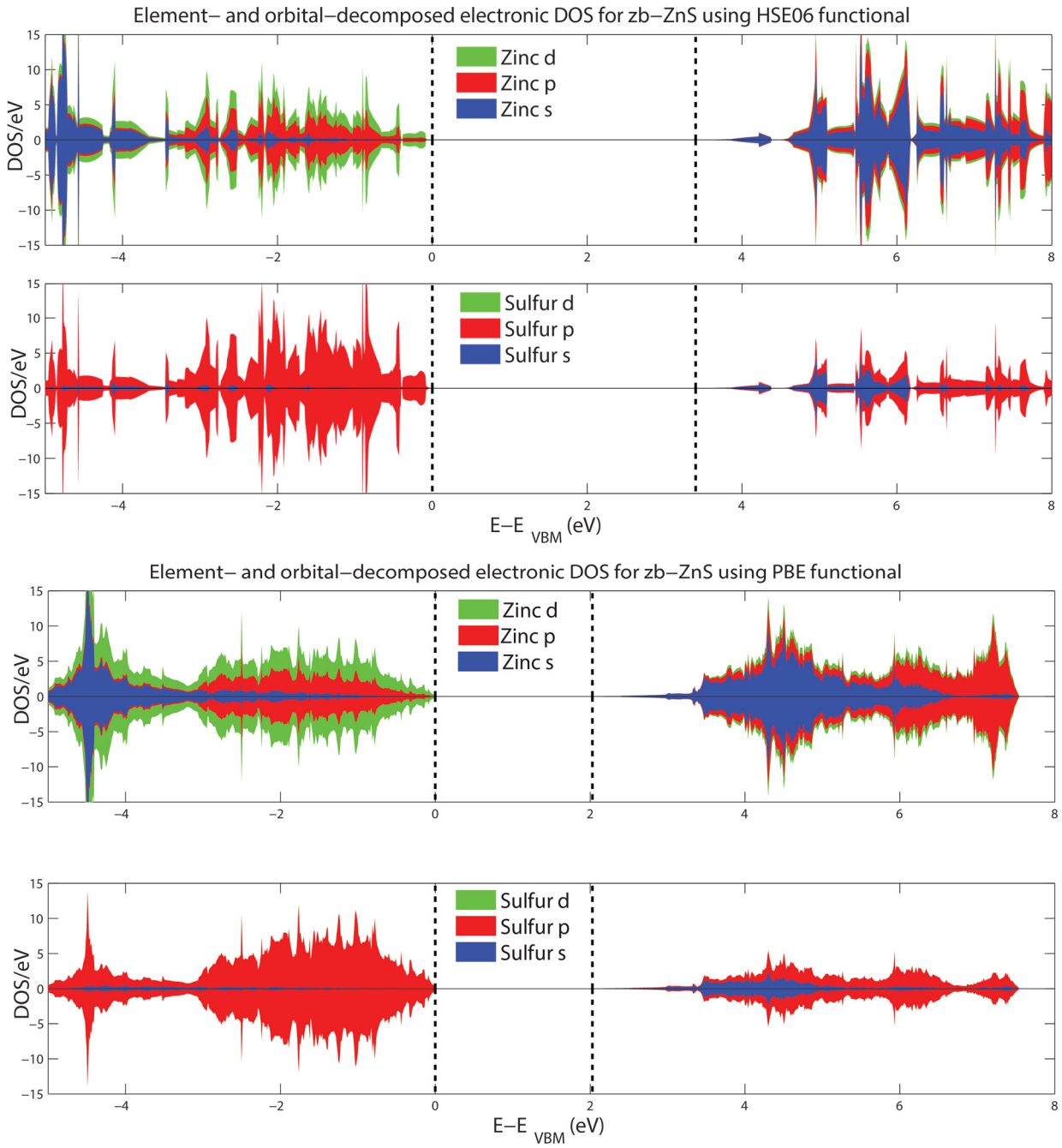

Element- and orbital-decomposed polarized electronic density of states for zinc blende zinc sulfide using both the HSE06 and PBE functionals. The coarseness of the plots is related to their k-point meshes. The HSE plot was made using a k-point mesh of 3x3x3 while the PBE plot used a finer mesh of 7x7x7. The valence band is principally sulfur p-orbital density while the conduction band is predominately zinc s-orbital density.

Figure 5.7

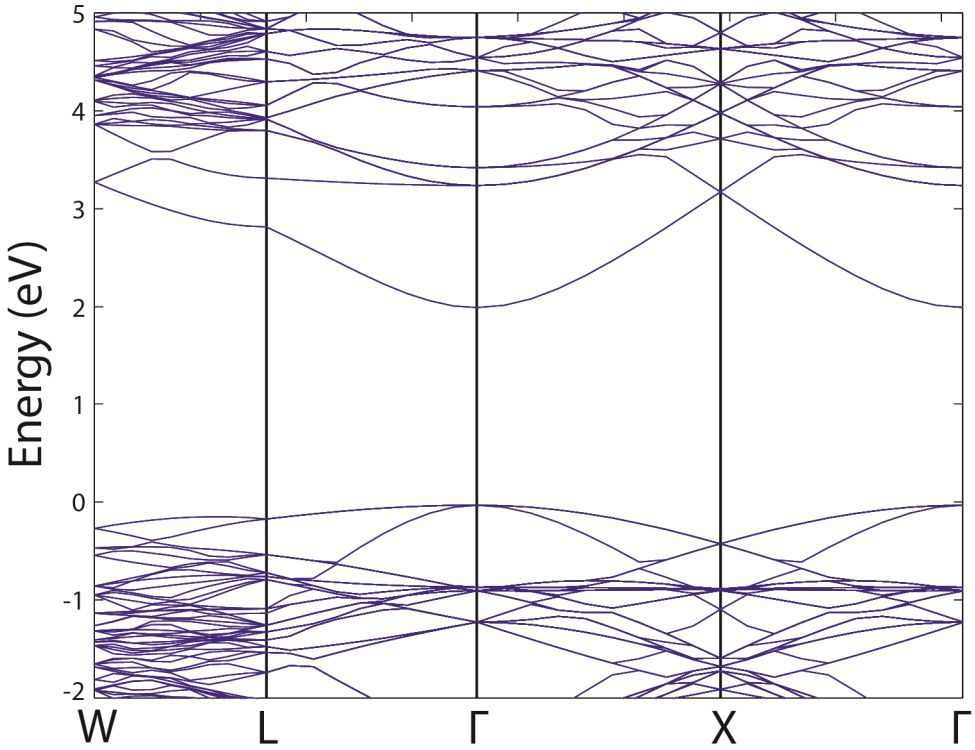

Calculated bandstructure of undoped zinc blende zinc sulfide using PBE functional. The W point is (¼, ½, 0), L point is (¼, ¼, ¼), the gamma (Γ) point is (0,0,0), and the X point is (0, ½, 0). As expected, there is a direct transition at the gamma point.

Figure 5.8

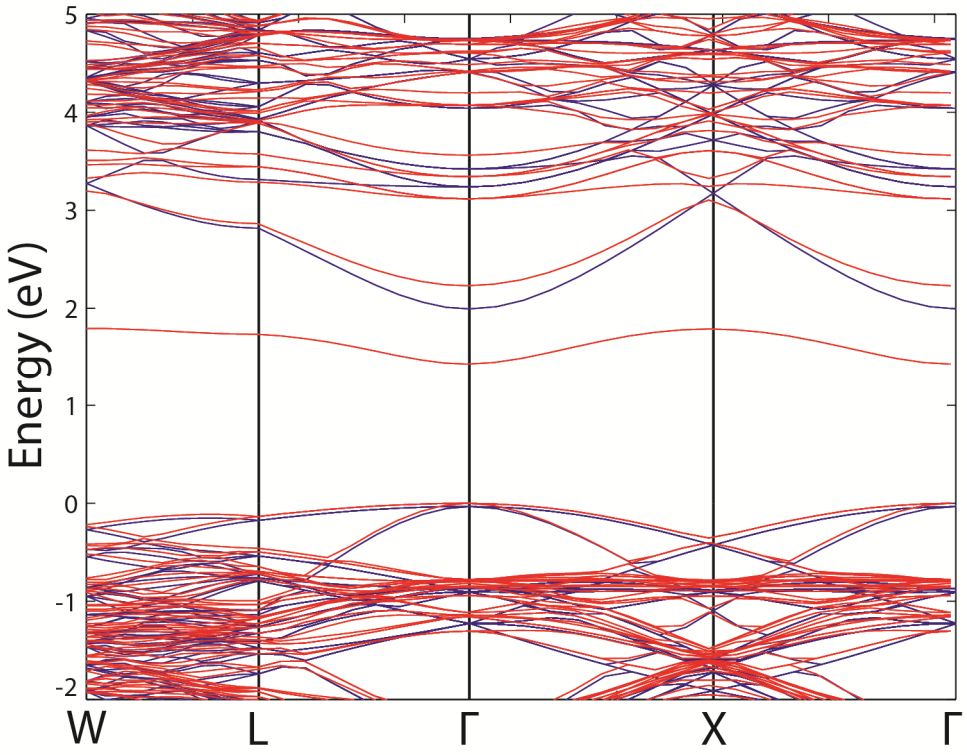

Calculated bandstructure of undoped zinc blende zinc sulfide (blue, same as Figure 5.7) overlayed with Si-doped zinc sulfide (red). Bandstructures are calculated using the PBE functional. The bandstructures were overlayed such that their VBMs would coincide. In fact, the Fermi level (ie. the zero energy level in the DFT calculation) is in the mid-gap state for the Si-doped system. Along the x-axis, the W point is (¼, ½, 0), L point is (¼, ¼, ¼), the gamma (Γ) point is (0,0,0), and the X point is (0, ½, 0). The intermediate state is evident in the doped bandstructure.

Figure 5.9

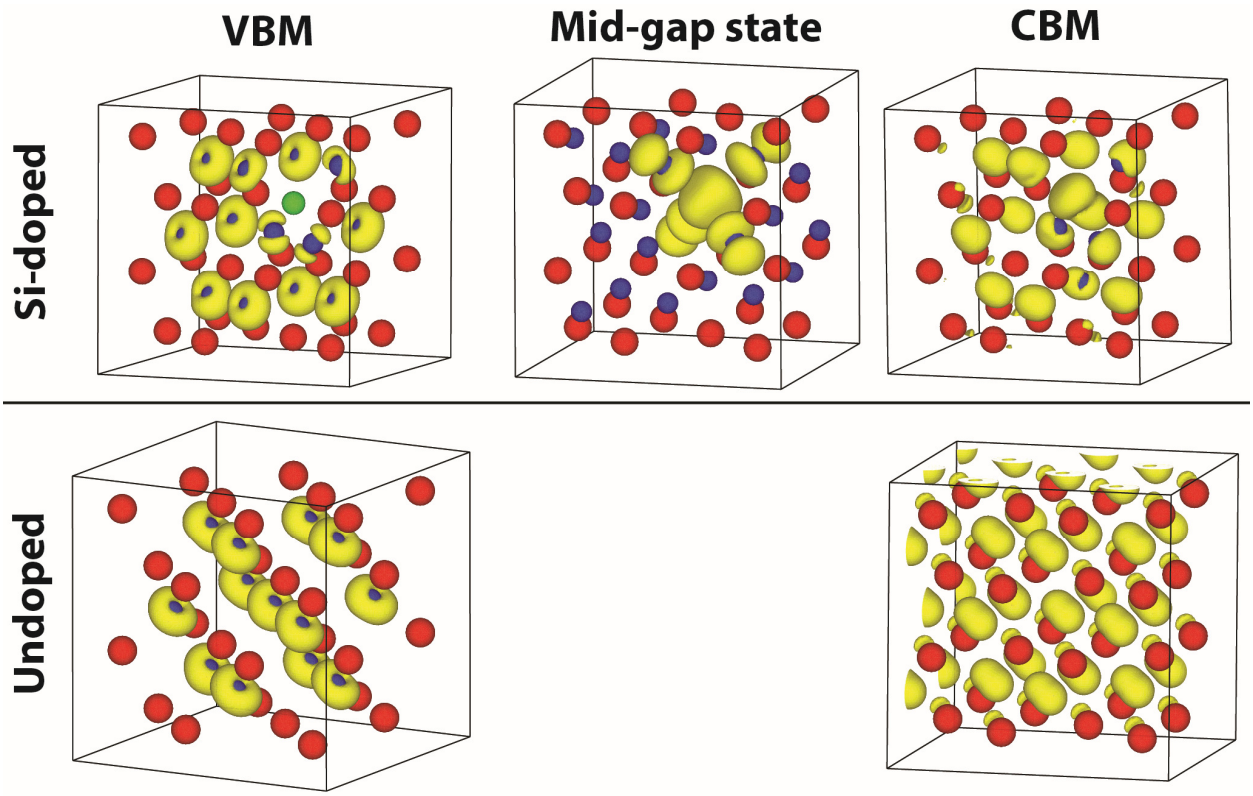

Visualization of electron density for undoped and Si-doped zinc sulfide for three energy levels: the valence band maximum, mid-gap state (Si-doped only), and conduction band minimum. Zinc atoms are red, sulfur atoms are blue, silicon is green, and density is yellow. The VBM has mostly donut-shaped density centered on sulfur, consistent with the density of states that shows the VBM is dominated by sulfur p-orbital character. The Si-doped mid-gap state is centered on the silicon dopant with a roughly spherical density, along with dumbbell-shaped density centered on the adjacent sulfurs. This is consistent with the density of states that shows the mid-gap state is a combination of silicon s-orbital and sulfur p-orbital character. The CBM for the undoped system is spherical around the zinc atoms, consistent with the density of states showing zinc s-orbital character. The CBM for the Si-doped system also has a strong zinc s-orbital character along with silicon s-orbital character.

Figure 5.10

Li +2.0	Be +1.1											B +5.0	C +1.2	N +7.0	O +3.9	F +0.8
Na +3.0	Mg +0.3											Al +1.9	Si +4.3	P +2.6	S	Cl +4.8
K +3.8	Ca -0.0	Sc +1.1	Ti +2.1	V +3.2	Cr +2.9	Mn +1.7	Fe +3.2	Co +3.2	Ni +3.6	Cu +3.4	Zn	Ga +3.2	Ge +3.4	As +5.7	Se +4.3	Br +6.0
Rb +4.3	Sr +0.4	Y +1.2	Zr +2.8	Nb +4.5	Mo +4.6	Tc	Ru +5.0	Rh +4.3	Pd +3.4	Ag +4.1	Cd +2.0	In +3.0	Sn +7.1	Sb +5.1	Te +5.8	I +6.9
Cs +7.8	Ba +1.0		Hf +3.3	Ta +5.2	W +5.8	Re +6.2	Os +6.2	Ir +4.2	Pt +4.5	Au +4.4	Hg	Tl	Pb +3.2	Bi +5.3	Po	At

Defect formation energy for each element in its preferred crystallographic site in the zinc blende zinc sulfide lattice. Positive defect formation energies indicate that the doping is not spontaneous.

Figure 5.11

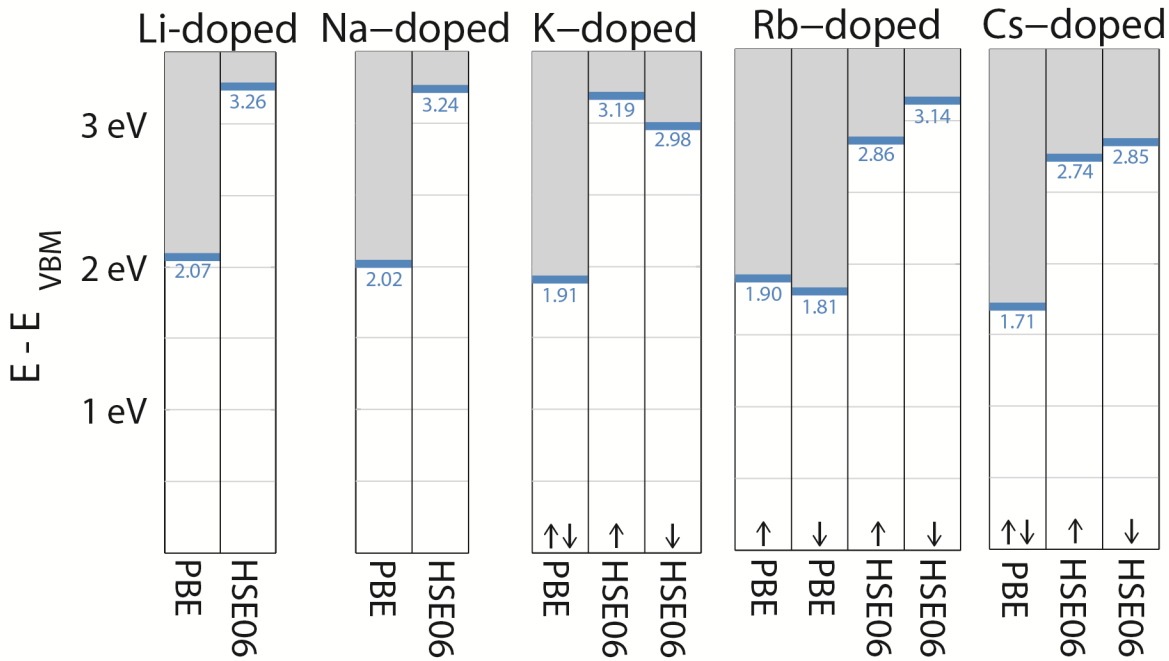

Eigen-energies for Group 1-doped zinc blende zinc sulfide at the gamma point. Each column represents a single calculation with the functional used listed at the bottom. The valence band maximums are normalized to zero. There are no mid-bandgap states in these systems. Blue lines represent the conduction band minimum. The grey box represents the continuum of states in the conduction band. Polarized calculations, required for the K-doped, Rb-doped, and Cs-doped systems, have spin up and spin down components denoted by upward and downward pointing arrows. Numbers below bands are the eigen-energy, relative to the VBM, in units of eV.

Figure 5.12

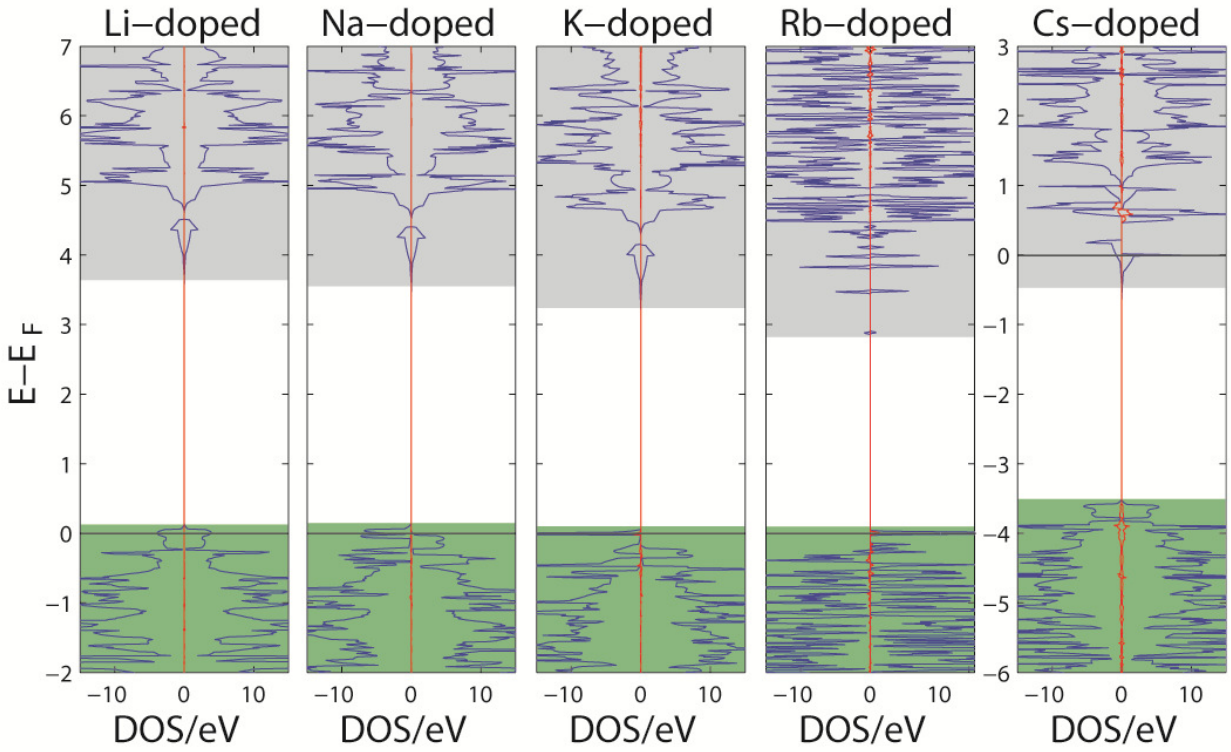

Polarized electronic density of states for Group 1-doped zinc sulfide using HSE06 functional. For clarity, the valence band is colored green and the conduction band is colored gray. The total density is plotted in blue while the total contribution from the dopant is red. There are no mid-gap states in these systems.

Figure 5.13

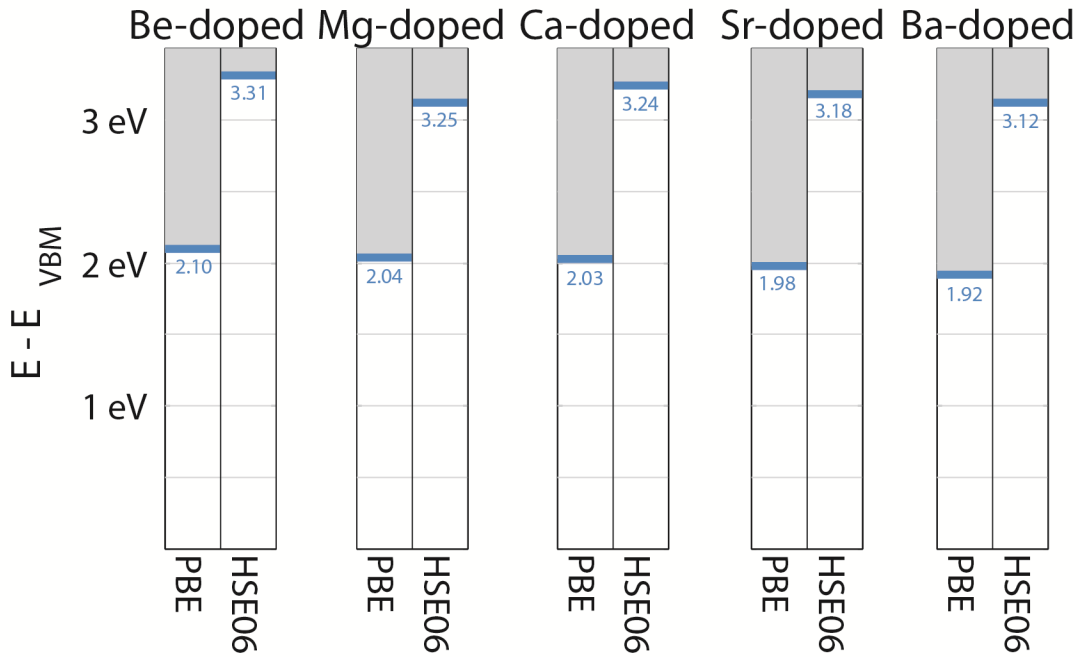

Eigen-energies for Group 2-doped zinc blende zinc sulfide at the gamma point. Each column represents a single calculation with the functional used listed at the bottom. The valence band maximums are normalized to zero. There are no mid-bandgap states in these systems. Blue lines represent the conduction band minimum. The grey box represents the continuum of states in the conduction band. None of these systems required polarized calculations. Numbers below bands are the eigen-energy, relative to the VBM, in units of eV.

Figure 5.14

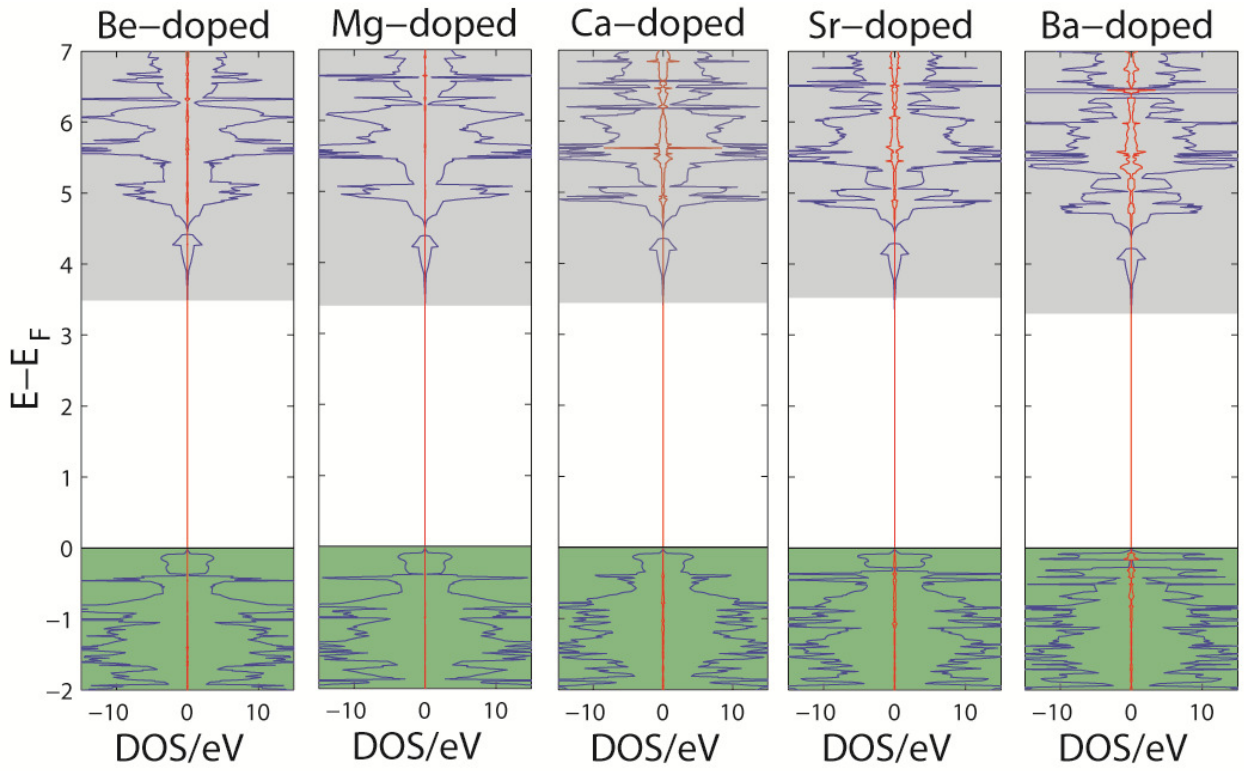

Polarized electronic density of states for Group 2-doped zinc sulfide using HSE06 functional. For clarity, the valence band is colored green and the conduction band is colored gray. The total density is plotted in blue while the total contribution from the dopant is red. There are no mid-gap states in these systems, but some dopant density is evident in the conduction band.

Figure 5.15

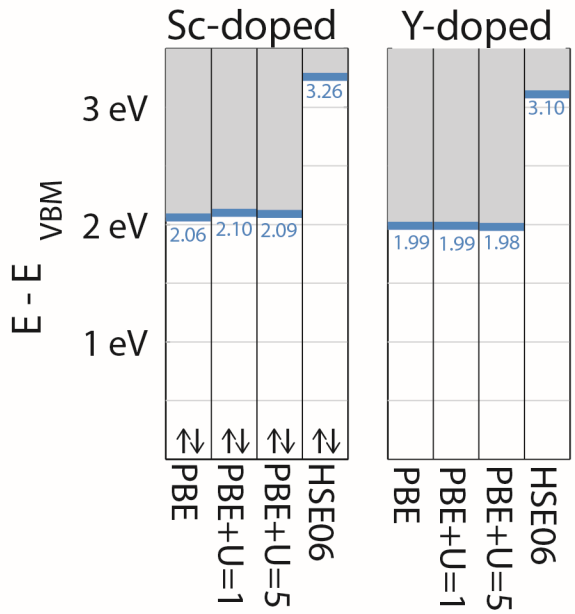

Eigen-energies for Group 3-doped zinc blende zinc sulfide at the gamma point. Each column represents a single calculation with the functional used listed at the bottom. The valence band maximums are normalized to zero. Neither Sc- or Y-doped systems have in-gap states. Blue lines represent the conduction band minimum. The grey box represents the continuum of states in the conduction band. Only Sc-doped ZnS required polarized calculations, but the two spin components were similar so they are overlaid in the figure. Numbers below bands are the eigen-energy, relative to the VBM, in units of eV.

Figure 5.16

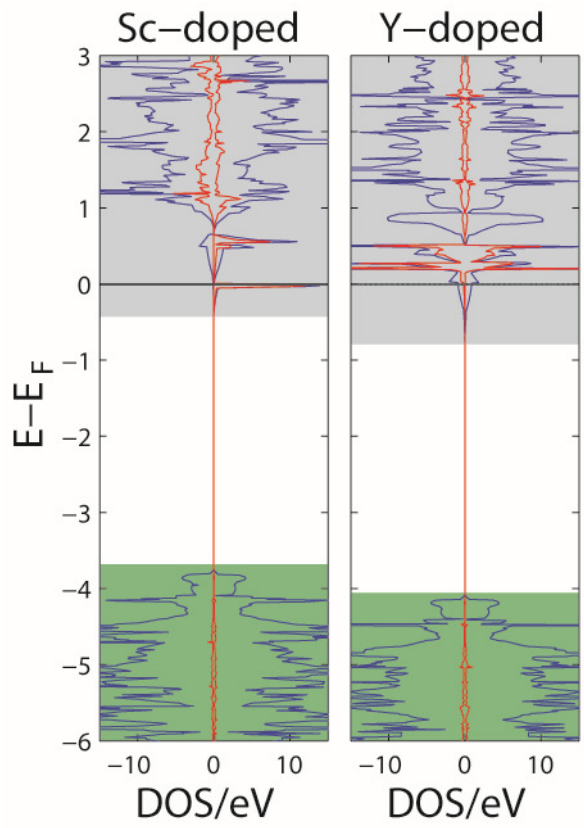

Polarized electronic density of states for Group 3-doped zinc sulfide using HSE06 functional. For clarity, the valence band is colored green and the conduction band is colored gray. The total density is plotted in blue while the total contribution from the dopant is red. There are no in-gap states in these samples, but the dopant density and Fermi level are in the conduction band.

Figure 5.17

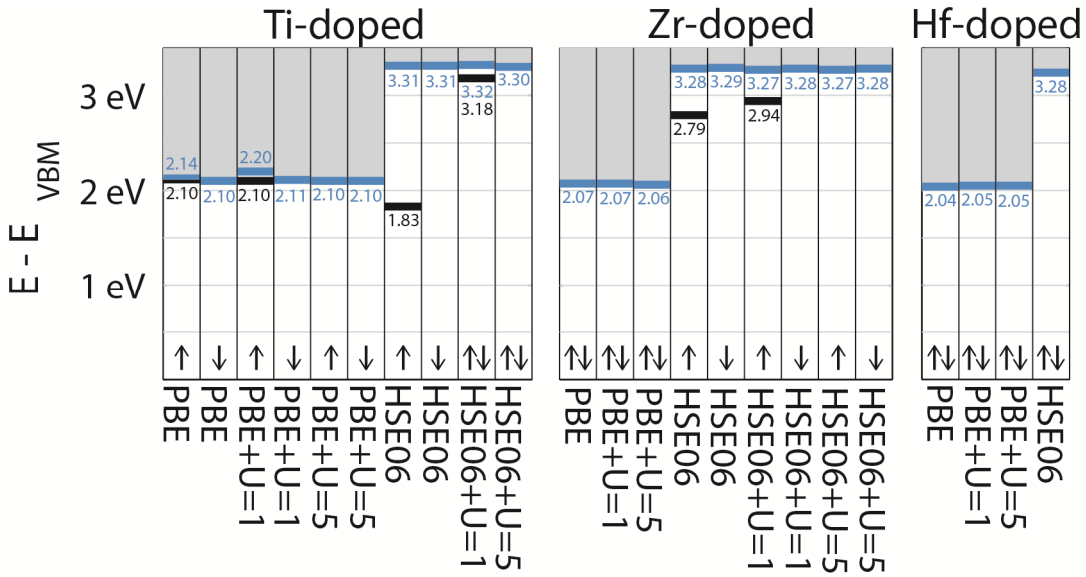

Eigen-energies for Group 4-doped zinc blende zinc sulfide at the gamma point. Each column represents a single calculation with the functional used listed at the bottom. The valence band maximums are normalized to zero. Blue lines represent the conduction band minimum. Solid black lines represent fully-occupied in-gap states. The grey box represents the continuum of states in the conduction band. All calculations are polarized calculations with both spin up and spin down components and denoted by upward and downward pointing arrows. Numbers below bands are the eigen-energy, relative to the VBM, in units of eV.

Figure 5.18

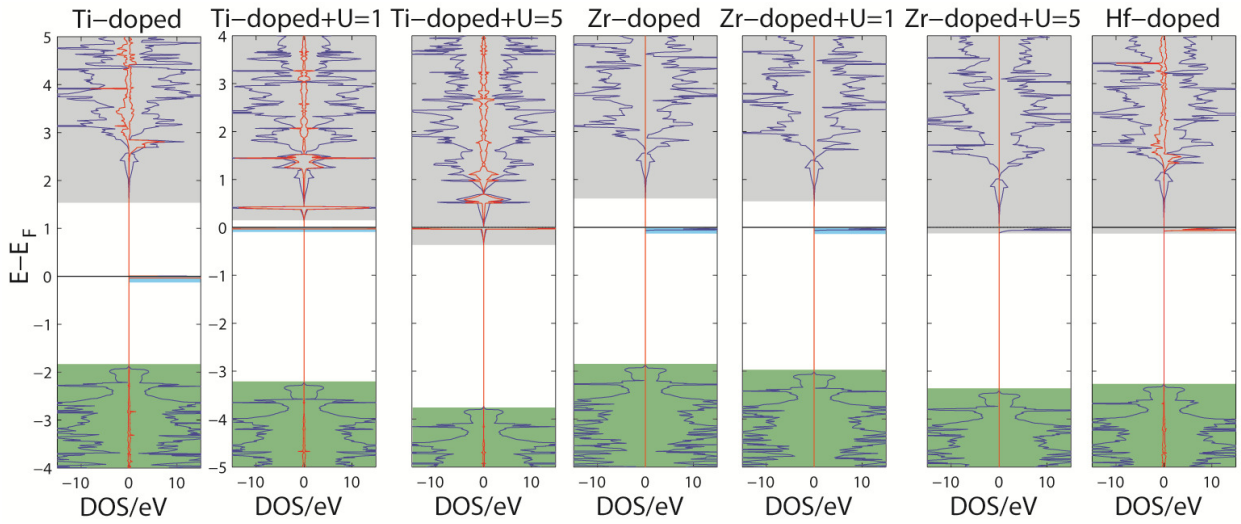

Polarized electronic density of states for Group 4-doped zinc sulfide using HSE06 and HSE06+U functionals. For clarity, the valence band is colored green, the conduction band is colored gray, and in-gap states are colored blue. The total density is plotted in blue while the total contribution from the dopant is red. There is a mid-gap state in the Ti- and Zr-doped systems, but those states move toward and then into the conduction band when the Hubbard correction is applied.

Figure 5.19

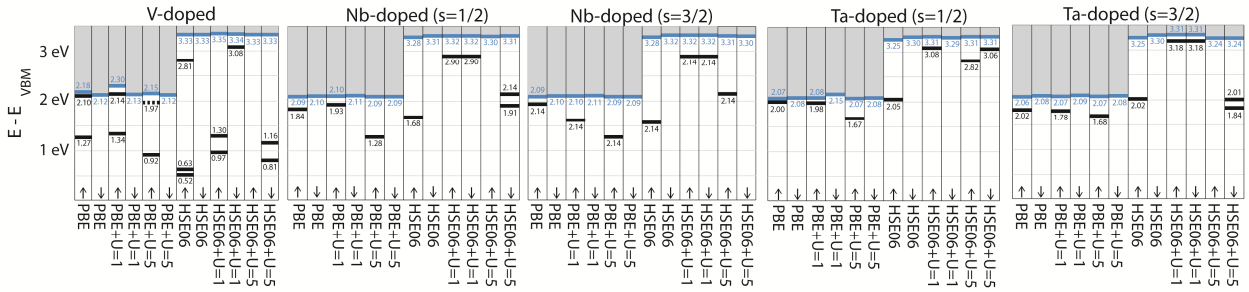

Eigen-energies for Group 5-doped zinc blende zinc sulfide at the gamma point. Each column represents a single calculation with the functional used listed at the bottom. The valence band maximums are normalized to zero. Blue lines represent the conduction band minimum. Solid black lines represent fully-occupied in-gap states, while dashed black lines represent empty or partially-occupied states. The grey box represents the continuum of states in the conduction band. All calculations are polarized calculations with both spin up and spin down components and denoted by upward and downward pointing arrows. Numbers below bands are the eigen-energy, relative to the VBM, in units of eV.

Figure 5.20

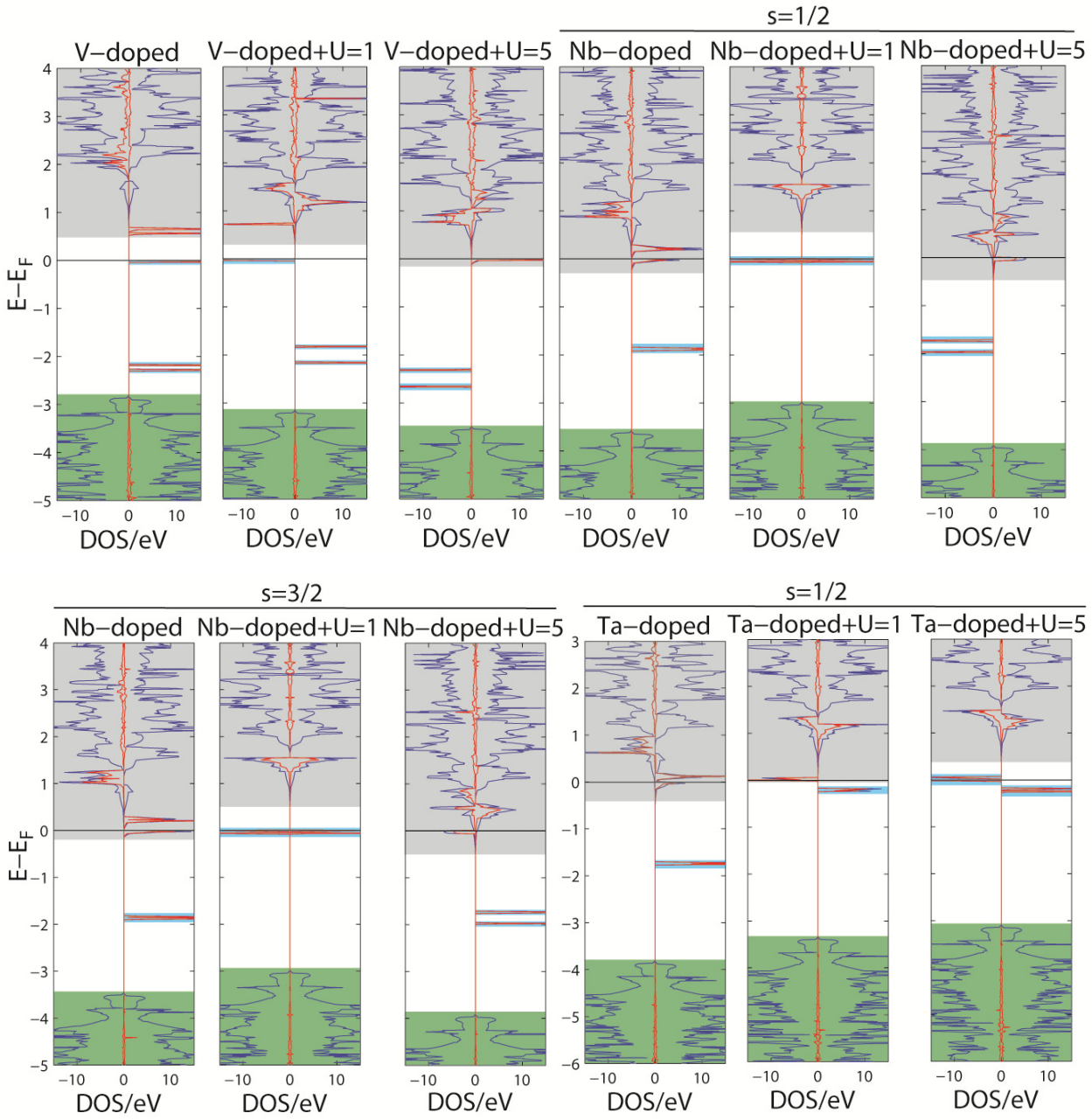
s=1/2
V–doped
V–doped+U=1
V–doped+U=5
Nb–doped
Nb–doped+U=1
Nb–doped+U=5
s=3/2
Nb–doped
Nb–doped+U=1
Nb–doped+U=5
s=1/2
Ta–doped
Ta–doped+U=1
Ta–doped+U=5
E–E_F
DOS/eV

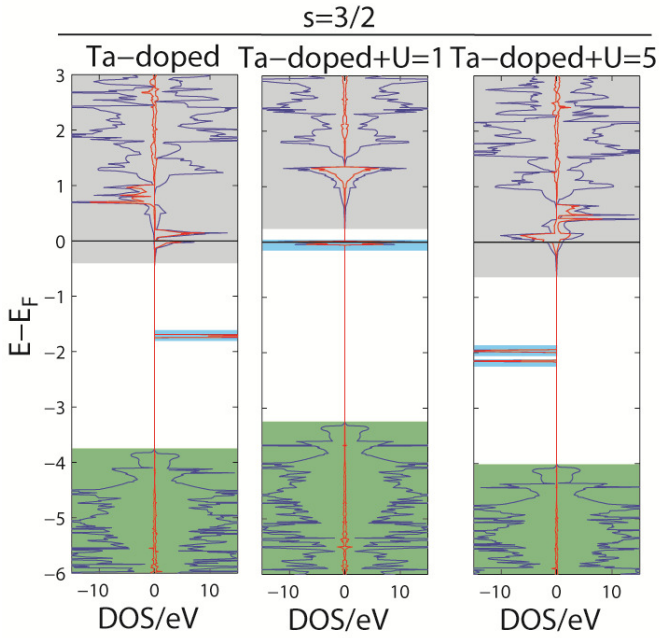

Polarized electronic density of states for Group 5-doped zinc sulfide using HSE06 and HSE06+U functionals. For clarity, the valence band is colored green, the conduction band is colored gray, and in-gap states are colored blue. The total density is plotted in blue while the total contribution from the dopant is red. Multiple spin states are provided for Ta- and Nb-doped systems because the two spin states have very similar energies.

Figure 5.21

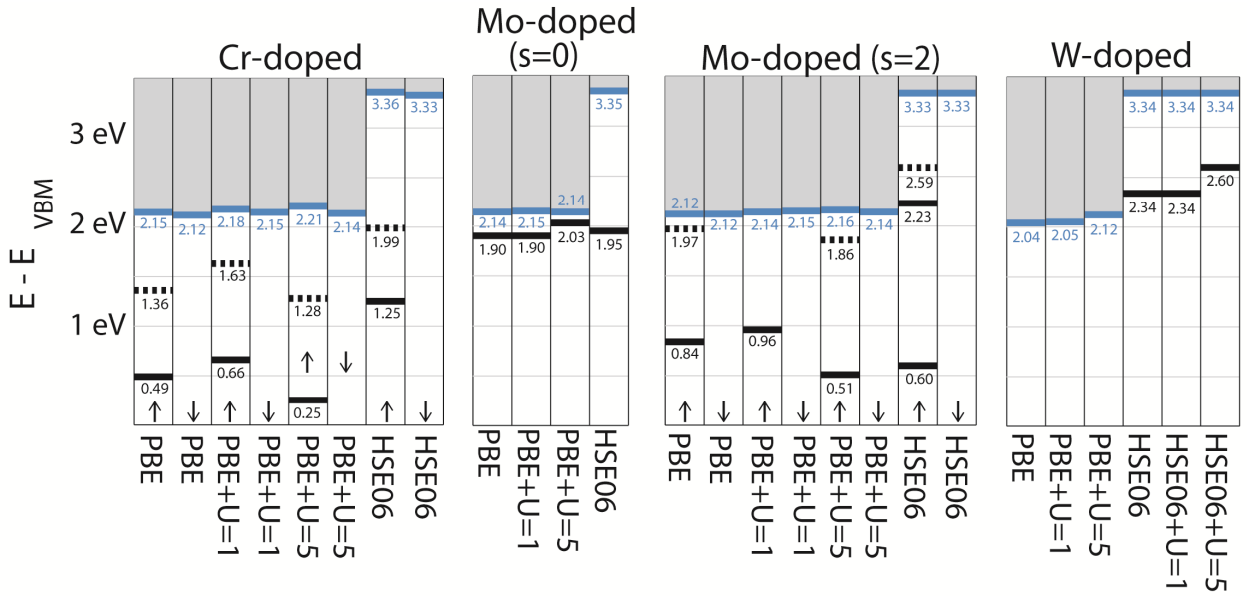

Eigen-energies for Group 6-doped zinc blende zinc sulfide at the gamma point. Each column represents a single calculation with the functional used listed at the bottom. The valence band maximums are normalized to zero. Blue lines represent the conduction band minimum. Solid black lines represent fully-occupied in-gap states, while dashed black lines represent empty or partially-occupied states. The grey box represents the continuum of states in the conduction band. Polarized calculations with both spin up and spin down components are denoted by upward and downward pointing arrows. Unpolarized calculations do not have arrows. Numbers below bands are the eigen-energy, relative to the VBM, in units of eV.

Figure 5.22

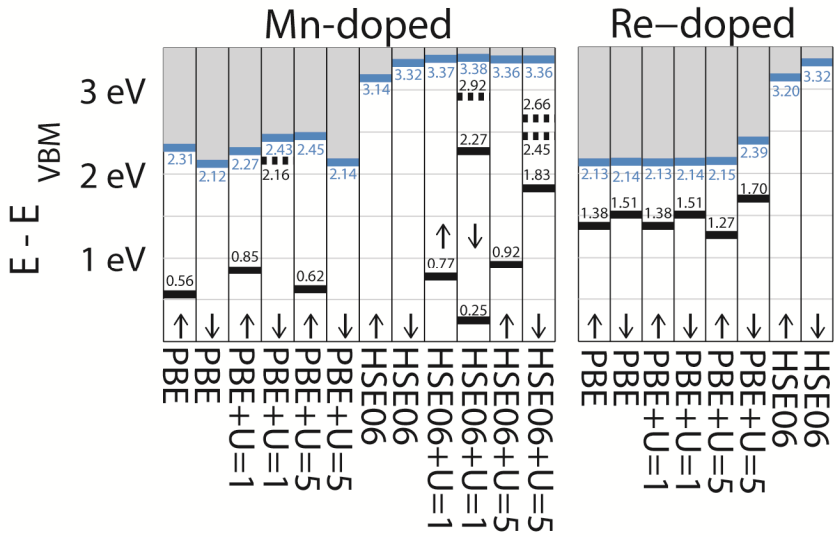

Eigen-energies for Group 7-doped zinc blende zinc sulfide. Each column represents a single calculation with the functional used listed at the bottom. The valence band maximums are normalized to zero. Blue

lines represent the conduction band minimum. Solid black lines represent fully-occupied in-gap states, while dashed black lines represent empty or partially-occupied states. The grey box represents the continuum of states in the conduction band. Polarized calculations with both spin up and spin down components are denoted by upward and downward pointing arrows. Numbers below bands are the eigen-energy, relative to the VBM, in units of eV.

Figure 5.23

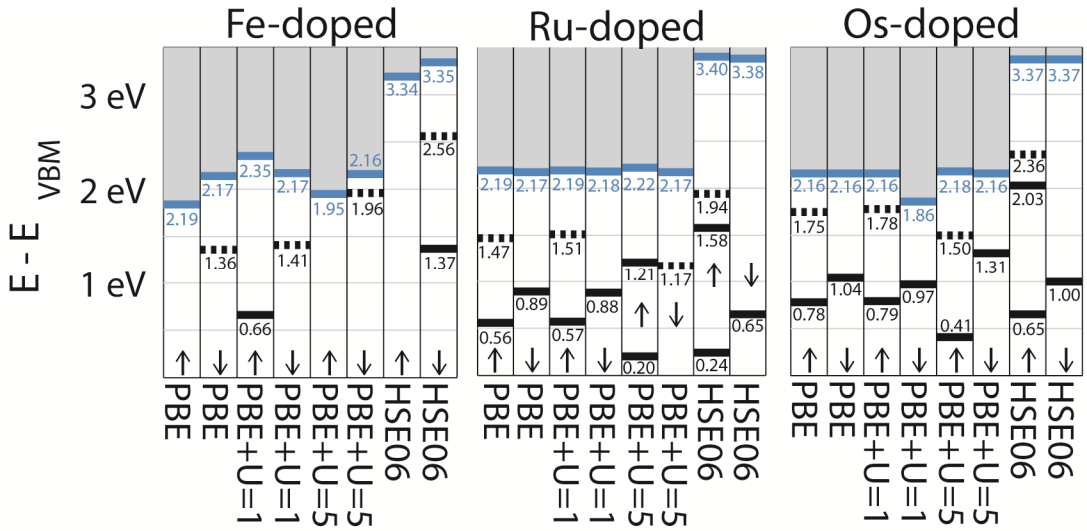

Eigen-energies for Group 8-doped zinc blende zinc sulfide. Each column represents a single calculation with the functional used listed at the bottom. The valence band maximums are normalized to zero. Blue lines represent the conduction band minimum. Solid black lines represent fully-occupied in-gap states, while dashed black lines represent empty or partially-occupied states. The grey box represents the continuum of states in the conduction band. Polarized calculations with both spin up and spin down components are denoted by upward and downward pointing arrows. Numbers below bands are the eigen-energy, relative to the VBM, in units of eV.

Figure 5.24

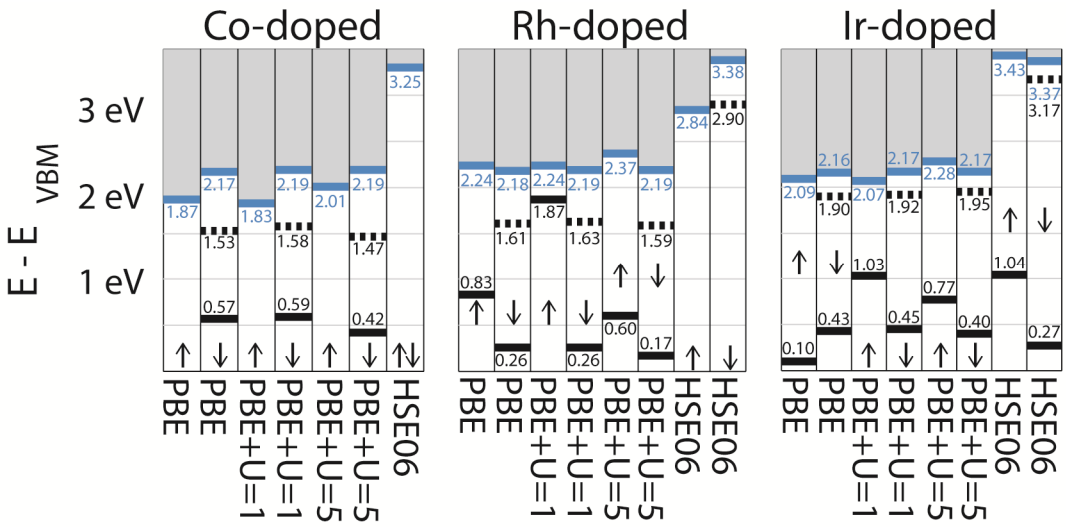

Eigen-energies for Group 9-doped zinc blende zinc sulfide. Each column represents a single calculation with the functional used listed at the bottom. The valence band maximums are normalized to zero. Blue lines represent the conduction band minimum. Solid black lines represent fully-occupied in-gap states, while dashed black lines represent empty or partially-occupied states. The grey box represents the continuum of states in the conduction band. Polarized calculations with both spin up and spin down components are denoted by upward and downward pointing arrows. Numbers below bands are the eigen-energy, relative to the VBM, in units of eV.

Figure 5.25

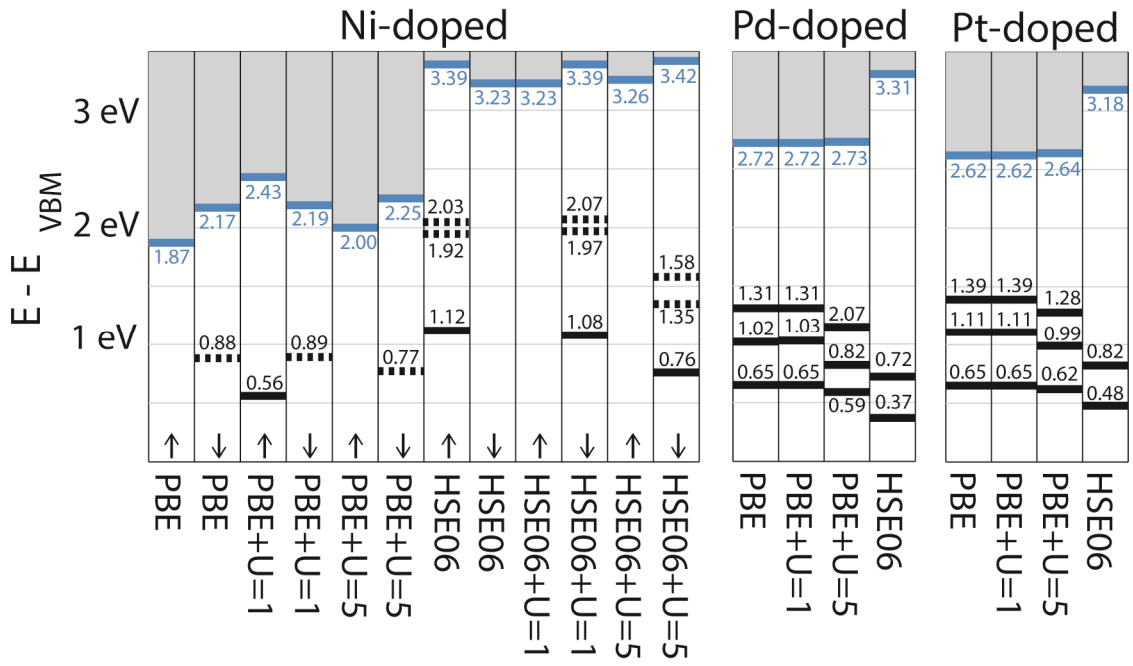

Eigen-energies for Group 10-doped zinc blende zinc sulfide. Each column represents a single calculation with the functional used listed at the bottom. The valence band maximums are normalized to zero. Blue lines represent the conduction band minimum. Solid black lines represent fully-occupied in-gap states, while dashed black lines represent empty or partially-occupied states. The grey box represents the continuum of states in the conduction band. The Ni-doped system used polarized calculations with both spin up and spin down components are denoted by upward and downward pointing arrows. The Pd- and Pt-doped systems did not require spin-polarized calculations. Numbers below bands are the eigen-energy, relative to the VBM, in units of eV.

Figure 5.26

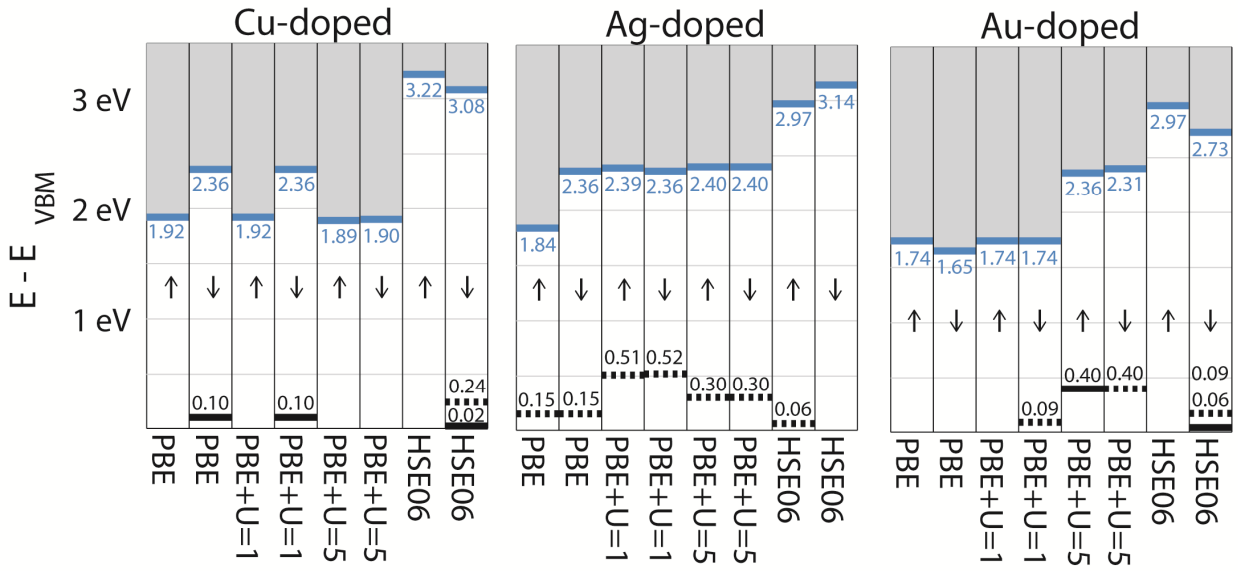

Eigen-energies for Group 11-doped zinc blende zinc sulfide. Each column represents a single calculation with the functional used listed at the bottom. The valence band maximums are normalized to zero. Blue lines represent the conduction band minimum. Solid black lines represent fully-occupied in-gap states, while dashed black lines represent empty or partially-occupied states. The grey box represents the continuum of states in the conduction band. Spin polarized calculations with both spin up and spin down components are denoted by upward and downward pointing arrows. Numbers below bands are the eigen-energy, relative to the VBM, in units of eV.

Figure 5.27

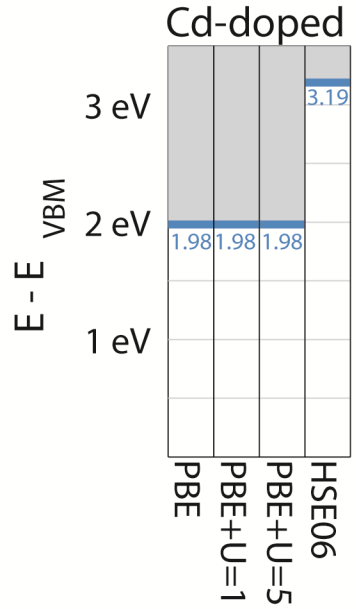

Eigen-energies for Group 12-doped zinc blende zinc sulfide. Zinc was omitted because that doping would be identical to the matrix and mercury was not calculated due to presumed toxicity and general incompatibility with vacuum-based materials processing. Each column represents a single calculation with the functional used listed at the bottom. The valence band maximums are normalized to zero. Blue lines represent the conduction band minimum. The grey box represents the continuum of states in the conduction band. The Cd-doped system does not require spin polarized calculations and has no in-gap states. Numbers below bands are the eigen-energy, relative to the VBM, in units of eV.

Figure 5.28

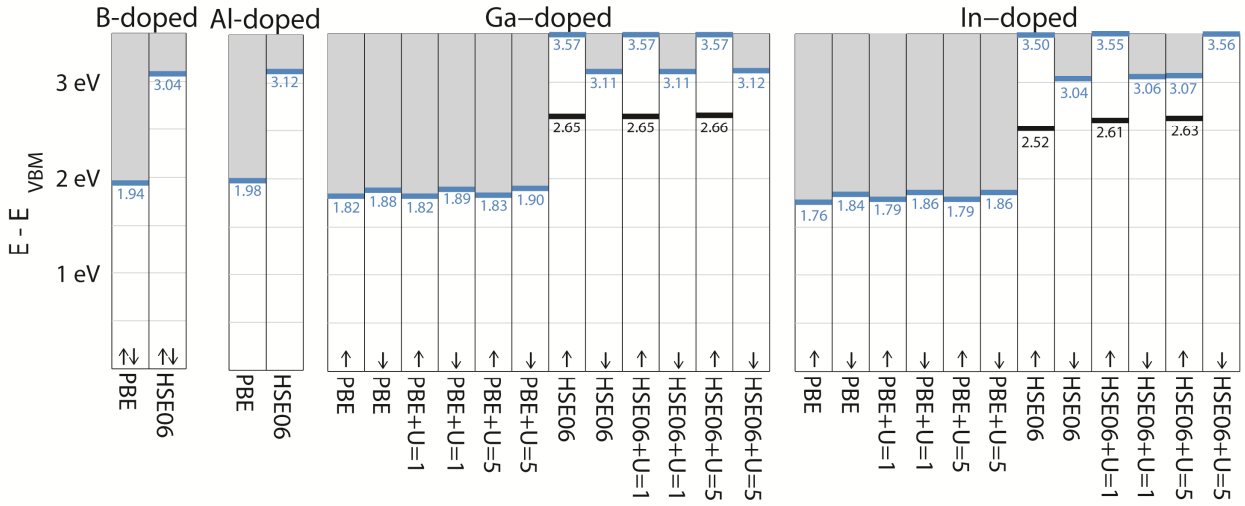

Eigen-energies for Group 13-doped zinc blende zinc sulfide. Each column represents a single calculation with the functional used listed at the bottom. The valence band maximums are normalized to zero. Blue lines represent the conduction band minimum. Solid black lines represent fully-occupied in-gap states. The grey box represents the continuum of states in the conduction band. The Al-doped system did not require spin polarized calculations, but other dopants that required polarized calculations have their spin up and spin down components denoted by upward and downward pointing arrows. Numbers below bands are the eigen-energy, relative to the VBM, in units of eV.

Figure 5.29

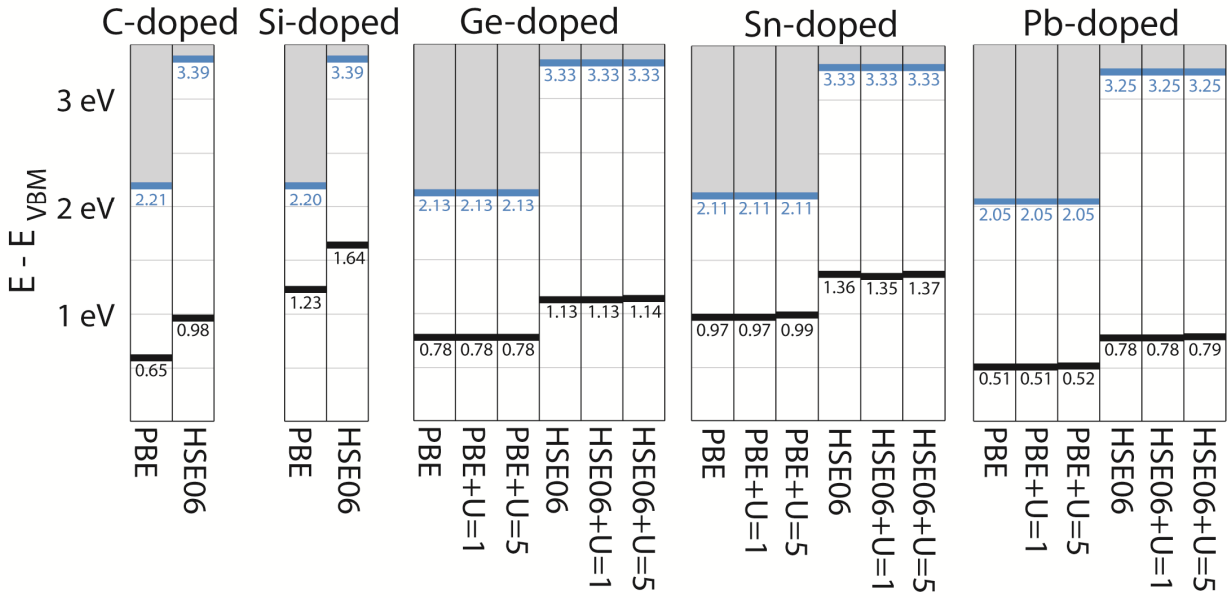

Eigen-energies for Group 14-doped zinc blende zinc sulfide. Each column represents a single calculation with the functional used listed at the bottom. The valence band maximums are normalized to zero. Solid black lines represent fully-occupied states. Blue lines represent the conduction band minimum. The grey box represents the continuum of states in the conduction band. All Group 14-doped systems preferred a non-magnetic configuration, thus these calculations are non-polarized and do not have spin up and spin down components. Numbers below bands are the eigen-energy, relative to the VBM, in units of eV.

Figure 5.30

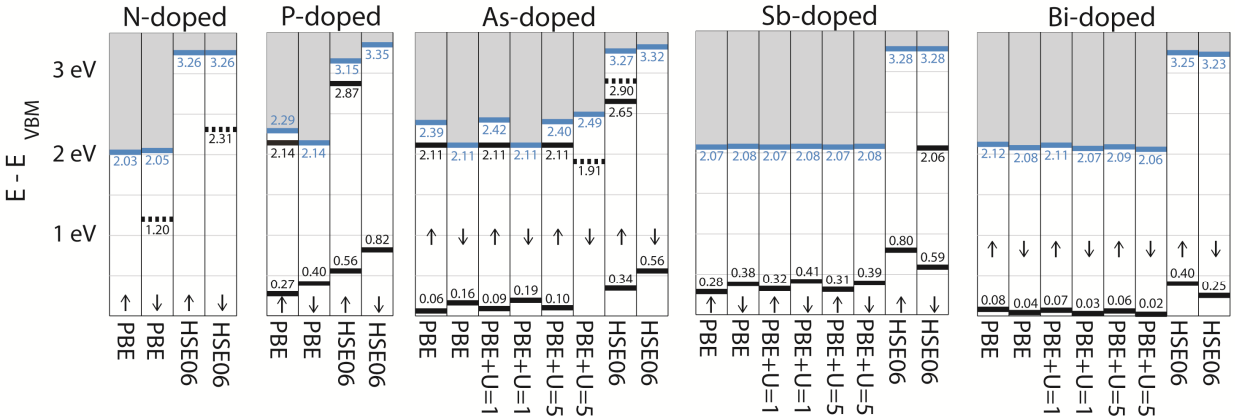

Eigen-energies for Group 15-doped zinc blende zinc sulfide. Each column represents a single calculation with the functional used listed at the bottom. The valence band maximums are normalized to zero. Solid black lines represent fully-occupied states while dashed black lines represent empty or partially-occupied states. Blue lines represent the conduction band minimum. The grey box represents the continuum of states in the conduction band. Polarized calculations with spin up and spin down components are denoted

by upward and downward pointing arrows. Numbers below bands are the eigen-energy, relative to the VBM, in units of eV.

Figure 5.31

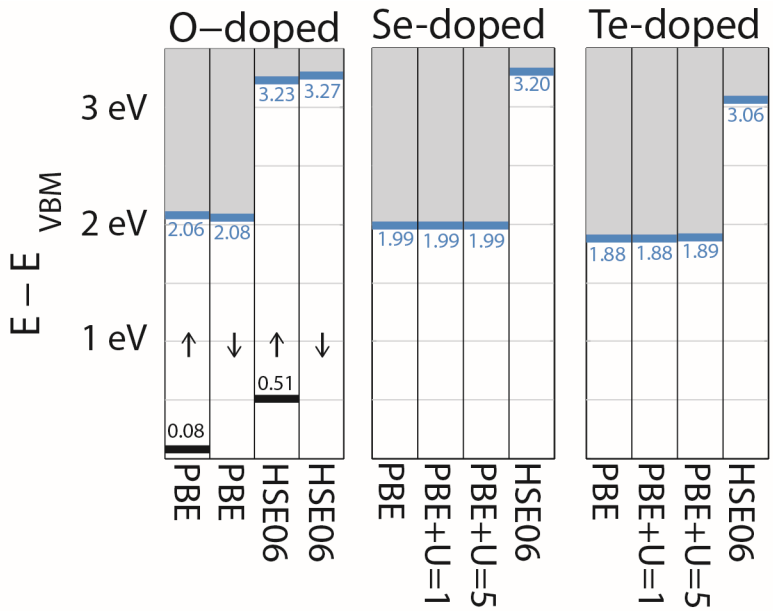

Eigen-energies for Group 16-doped zinc blende zinc sulfide. Each column represents a single calculation with the functional used listed at the bottom. The valence band maximums are normalized to zero. Solid black lines represent fully-occupied states. Se- and Te-doped systems have no in-gap states. Blue lines represent the conduction band minimum. The grey box represents the continuum of states in the conduction band. Only oxygen-doped ZnS required polarized calculations whose spin up and spin down components are denoted by upward and downward pointing arrows. Numbers below bands are the eigen-energy, relative to the VBM, in units of eV.

Figure 5.32

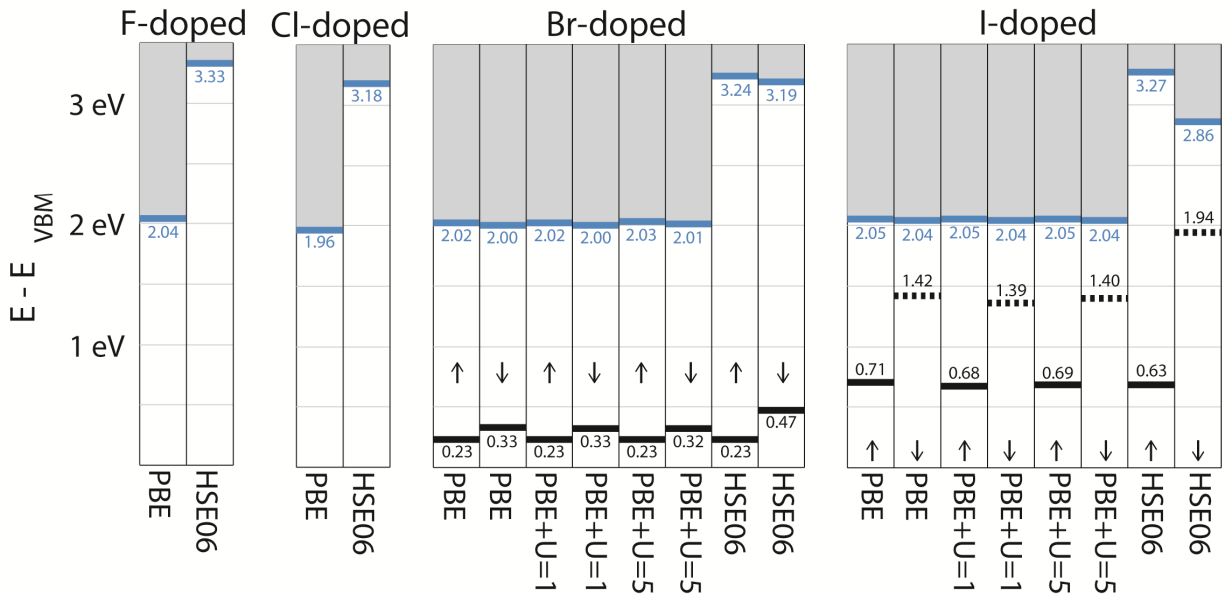

Eigen-energies for Group 17-doped zinc blende zinc sulfide. Each column represents a single calculation with the functional used listed at the bottom. The valence band maximums are normalized to zero. Solid black lines represent fully-occupied states while dashed black lines represent empty or partially-occupied states. Blue lines represent the conduction band minimum. The grey box represents the continuum of states in the conduction band. Polarized calculations with spin up and spin down components are denoted by upward and downward pointing arrows. Numbers below bands are the eigen-energy, relative to the VBM, in units of eV.

Figure 5.33

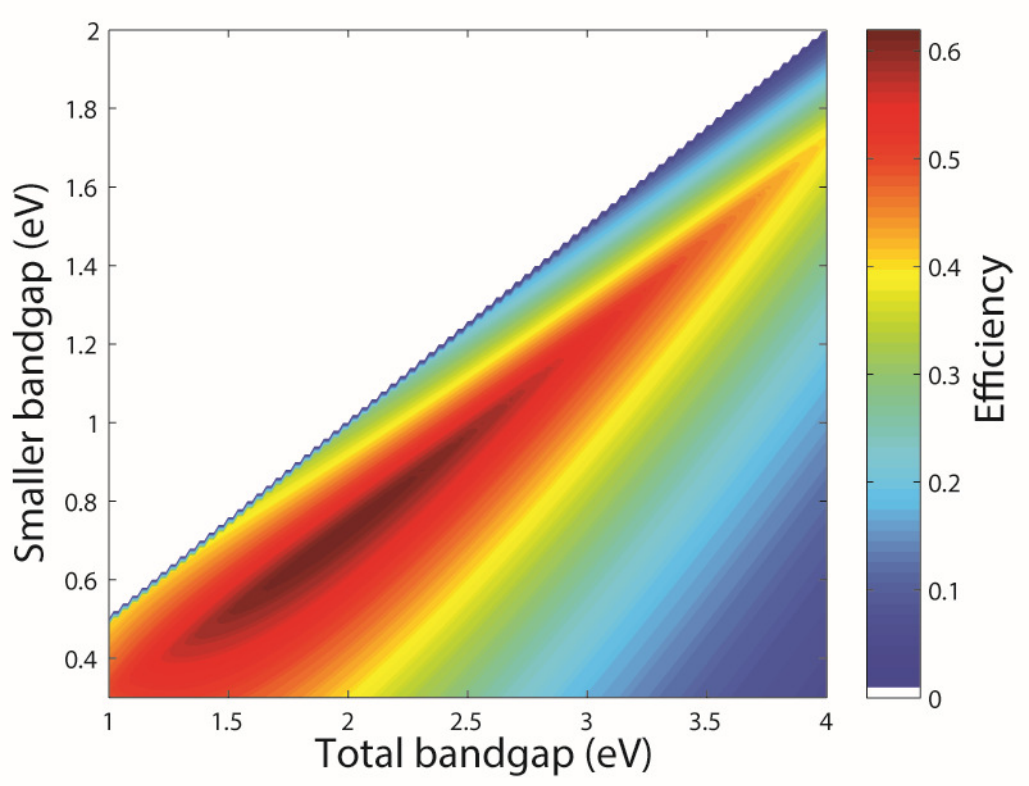

Detailed balance efficiency calculated for a variety of bandgaps at maximum concentration. This calculation is only a function of bandgap and is therefore agnostic to matrix and dopant materials.

References

[1] S. Chen and L.-W. Wang, "Intrinsic defects and electronic conductivity of TaON: First-principles insights," *Appl. Phys. Lett.*, vol. 99, no. 22, p. 222103, 2011.